Nanomaterials and High-Contrast Metastructures for Integrated Optoelectronics

Kun Li

Electrical Engineering and Computer Sciences
University of California at Berkeley

December 1, 2017

Nanomaterials and High-Contrast Metastructures for Integrated Optoelectronics

by

Kun Li

A dissertation submitted in partial satisfaction of the

requirements for the degree of

Doctor of Philosophy

in

Engineering-Electrical Engineering and Computer Sciences

and the Designated Emphasis

in

Nanoscale Science and Engineering

in the

Graduate Division

of the

University of California, Berkeley

Committee in charge:

Professor Constance J. Chang-Hasnain, Chair
Professor Ming C. Wu
Professor Feng Wang
Professor Eli Yablonovitch

Fall 2016

Nanomaterials and High-Contrast Metastructures for Integrated Optoelectronics

Copyright © 2016

by Kun Li

Abstract

Nanomaterials and High-Contrast Metastructures for Integrated Optoelectronics

by

Kun Li

Doctor of Philosophy in Engineering-Electrical Engineering and Computer Sciences

and the Designated Emphasis in Nanoscale Science and Engineering

University of California, Berkeley

Professor Constance J. Chang-Hasnain, Chair

Integrated optoelectronics has demonstrated its great potential in numerous fields. In the past decade, its applications have rapidly expanded from the conventional long-haul optical communication to emerging areas such as data center, consumer electronics, energy harnessing, environmental sensing, and biological imaging. This revolutionary progress benefits from the advancement in light generation, manipulation, detection and its interaction with other systems. Device innovation is the key in this advancement. My dissertation discusses this innovation from two aspects: the integration of nanomaterials and the incorporation of metastructures in optoelectronic devices.

The first topic focuses on material integration to facilitate on-chip optoelectronic devices. As microprocessors become progressively faster, chip-scale data transport has turned progressively more challenging. Optical interconnects for inter- and intra-chip communications are required to reduce power consumption and increase bandwidth. Integrating III-V compound semiconductors with superior optical proficiencies onto the silicon-based microelectronic backbone can pave the way towards a highly compact optoelectronic platform, combing the strengths of both materials. The direct growth of III-V micropillars on silicon substrate in the unique growth mode and under CMOS-compatible condition can yield single-crystal structures in sizes exceeding lattice-mismatched critical dimensions. These micropillars overcome the drawbacks of conventional nanowires, thus are endued with superior optical characteristics for on-chip lasers, photodetectors, and cost-effective solar cells. I will discuss the optical characterization of InP micropillars directly grown on silicon, and the optimization of their optical properties. The excellent material quality and device performance of these InP micropillars show promise for a variety of integrated optoelectronic devices.

The second topic centers at the function integration enabled by high-contrast subwavelength grating (HCG), on the platform of vertical-cavity surface-emitting lasers (VCSELs). VCSELs are key light sources in integrated optoelectronics, with the advantages of low power consumption, low packaging cost, and ease of fabrication into arrays for wafer-scale testing. Mode-hop-free, fast and widely tunable VCSELs are also

an ideal candidate for the emerging swept-source optical coherence tomography (SS-OCT) as well as light detection and ranging (LiDAR) applications. I will investigate how HCG, an ultrathin monolithic layer of sub-wavelength metastructure, can function as a highly reflective broadband mirror to facilitate lasing of VCSEL. Widely tunable HCG-VCSELs emitting at 1060-nm are demonstrated, a prevalent light source in SS-OCT for 3D eye imaging. Besides functioning as a tunable mirror, the HCG can also be designed as an integrated beam-shaping element at the same time. The rich properties and the large design space of HCG enable direct tailoring of the output beam features of VCSELs, such as transverse-mode control and far-field emission patterning with angular and spatial modulations by HCG. This opens new avenues for direct laser beam shaping with a monolithic optical element for integrated optoelectronics.

To my parents and my husband

TABLE OF CONTENTS

ACKNOWLEDGEMENTS

First of all, I would like to give the most sincere thanks to my advisor Prof. Connie Chang-Hasnain. She has not only guided me in the aspects of academics and research, but also has been a great mentor to help build my character for life. With the support and opportunities she provides, I have gained tremendous growth during graduate school. I am very grateful for her untiring effort and warm care as an advisor and lifetime mentor, especially for being such a wonderful role model for my future career.

I want to thank Prof. Eli Yablonovitch, Prof. Ming Wu, and Prof. Feng Wang for serving on my qualifying exam and dissertation committee, with their great guidance and advice.

Looking back to these six years of ups and downs, laughter or tears, I would not have made it this far without the help and company of the CCHG big family. This dissertation is not possible without the great teamwork and close collaboration with Kar Wei Ng, Hao Sun, Thai Tran, Fan Ren, Roger Chen, Fanglu Lu, Chris Chase, Yi Rao, Pengfei Qiao, and Weijian Yang. I would like to thank my graduate student mentors for both projects – Roger Chen, Thai Tran, Weijian Yang, Yi Rao, and Chris Chase. I did not realize how much I should appreciate their patience and effort until I have started mentoring new students myself. I also want to thank the co-workers at Bandwidth 10 Inc. for their help during my internship. The peers who were in the group around the same time, Wilson Ko, James Ferrara, Fanglu Lu, Li Zhu, Tianbo Sun, Adair Gerke, and Indrasen Bhattacharya, have shared lots of great memories and learning experience together with me. I also thank Ms. Therese George for always taking care of us as an administrative assistant. I am grateful to all the CCHG research group members, the past members for setting excellent standards, the current members for showing outstanding teamwork, and the future ones for carrying on the awesome traditions.

Life at graduate school is more fun with the numerous ideas and supports from the faculty and staff at EECS department; the inspiring student groups such as WICSE, Photobears, and EEGSA; as well as the diverse and open-minded environment that UC Berkeley has offered us. I thank the EECS peers, my housemates, and other friends who I met here and have gone on this journey together. I have learnt a lot and will continue to learn from these awesome people. Go bears!

Last but certainly not least, I want to give the special thanks to my dear parents and husband for their endless support and love.

LIST OF FIGURES

LIST OF TABLES

Chapter 1
Dissertation Overview

Integrated optoelectronics has seen its rapid development in the past decade. From its original primary application in long-haul communications and access network, integrated optoelectronics has expanded itself to data center, consumer electronics, energy harnessing, environmental sensing, biological and medical imaging, etc. This revolutionary progress benefits from the advancement in light generation, manipulation, detection and its interaction with other systems. Device innovation is the key in this advancement. During my doctoral study, I was lucky enough to have worked on two research directions related to integrated optoelectronics on the device level.

For the first half of my PhD, I have primarily worked on optoelectronic devices based on III-V nano/miropillars directly grown on silicon – the material integration for optoelectronics. Owing to both physics and the tremendous effort that has gone into their development, silicon and group-III-V compound semiconductor have become the principal materials for electronics and photonics, respectively. Naturally then, the integration of these two materials appears to be a pathway towards optoelectronic functionality. Silicon has been the prevalent backbone for the existing microelectronic infrastructures and the foundation of complementary metal-oxide-semiconductor (CMOS) transistor devices. It is difficult, however, to utilize silicon for optoelectronic devices, since it is an indirect bandgap material. Direct bandgap materials that exhibit superior proficiencies in optical processes are traditionally group III-V compound semiconductors, which on the other hand, are not as cost effective as silicon. Integrating III-V semiconductors onto silicon can therefore pave the way towards a highly compact optoelectronic platform combining the strengths of both materials. As microprocessors become progressively faster, chip-scale data transport has turned progressively more challenging. Optical interconnects for inter- and intra-chip communications are required to reduce power consumption and increase bandwidth. Growing III-V material directly on silicon opens a pathway to integrate superior optoelectronic properties with massive existing silicon-based infrastructure. However, the efforts have been mainly blocked by the lattice mismatch between III-V and silicon.

Our group has developed a unique growth mechanism to grow GaAs-based and InP-based nanoneedle/nanopillar/micropillar structures on a variety of lattice-mismatched substrates [1]-[4]. Our method is superior to traditional nanowire growth benefiting from its unique core-shell mode growth mechanism by low-temperature MOCVD without any external catalyst. The growth conditions have been verified to be CMOS post-process compatible [5].The diameter of the pillars can then go far beyond the lattice-mismatch critical dimension and offer outstanding optical gain and other optoelectronic characteristics [6]. Furthermore, the growth condition can be adjusted to achieve single crystalline pure wurtzite phase, which is ideal for achieving optimal optical efficiency. Among the III-V materials, InP stands out as a promising material platform for laser sources, solar cells, photodetectors, as well as other integrated optoelectronic devices. The first half of this dissertation will focus on the InP-based nanoneedles/nanopillars/micropillars and their optoelectronic characteristics. **Chapter 2** introduces the background for optoelectronic material integration, as well as the growth and material characterization methods used here for the nano/miropillars grown on silicon. **Chapter**

1

3 discusses the tailoring and optimization of optical characteristics of micro-sized InP nanoneedles grown on silicon by tuning the growth conditions, facilitated by a variety of optical characterization methods [7]. **Chapter 4** focuses on the optimized wurtzite-phased InP miropillars grown on silicon, and further characterizes the pillar's surface quality by proposing an innovative metrology method [8]. As a conclusion, single-crystal wurtzite-phased InP miropillars directly grown on silicon are endued with excellent optical characteristics and thus can be a promising material platform for integrated optoelectronics.

For the second half of my PhD, I have focused on the function integration for optoelectronics, based on a novel integrated optical element - high-contrast subwavelength grating (HCG). Compared to other optical elements, HCG has very rich properties and design flexibility. Some of them are fascinating and extraordinary, such as broadband high reflectivity, and high quality factor resonance - all it needs is a single thin-layer of HCG. Furthermore, it can be a microelectromechanical (MEMS) structure. These rich properties are readily to be harnessed and turned into novel devices. Numerous devices have been reported using HCG, including a tunable-frequency VCSEL [9], [10], a high-Q optical resonator [11], a planar lens [12] and a hollow-core waveguide that uses an HCG to redirect light [13].

Vertical-cavity surface-emitting lasers (VCSELs) are key light sources in integrated optoelectronics, with the advantages of low power consumption, low packaging cost, and ease of fabrication into arrays for wafer-scale testing. Mode-hope-free, fast and widely tunable VCSELs are also an ideal candidate for the emerging swept-source optical coherence tomography (SS-OCT) as well as light detection and ranging (LiDAR) applications [14]. Our group has developed a revolutionary single-layer, high-index contrast sub-wavelength grating (HCG), and implemented it as a reflection mirror in VCSEL. Compared with conventional reflective Bragg reflector mirrors (DBR), the seemingly simple-structured HCG provides ultra-broadband high reflectivity (R>0.99, $\Delta\lambda/\lambda$>35%) and high quality-factor resonance (Q>107) [15]. In the second half of this dissertation, I will investigate how high-contrast grating (HCG) could function as a highly reflective broadband mirror to facilitate lasing of VCSEL. Widely tunable HCG-VCSEL emitting at 1060-nm are demonstrated, a prevalent light source in SS-OCT for 3D eye imaging. Beyond wavelength tuning, the rich properties and the large design space of HCG enable direct tailoring of the output beam features, such as transverse-mode control and far-field emission patterning. This opens up new avenues for direct laser beam shaping with a monolithic optical element for integrated optoelectronics. **Chapter 5** introduces the background knowledge of VCSEL, its challenges, and how it can be improved with HCG mirror. **Chapter 6** demonstrates HCG as an integrated tuning mirror for 1060-nm GaAs-based VCSEL, with excellent laser performance reported [16]. **Chapter 7** shows another unique property of HCG – as an integrated beam-shaping element for VCSEL [17]. As a conclusion, the ultrathin monolithic HCG element with versatile characteristics has huge potential for function integration of optoelectronics.

Chapter 8 will summarize the dissertation with proposal of future work and outlook.

Chapter 2
Nanomaterials for Integrated Optoelectronics

Owing to both physics and the tremendous effort that has gone into their development, silicon and group-III-V compound semiconductor have become the principal materials for electronics and photonics, respectively. Naturally then, the integration of these two materials appears to be a pathway towards optoelectronic functionality. The first half of my dissertation will focus on optoelectronic integration by growing III-V nanomaterials on silicon. Before going into the details of my research project, it is dutiful to first summarize the major efforts that have been devoted to silicon-based optoelectronic integration.

2.1 Approaches to Optoelectronic Integration

2.1.1 III-V on silicon

Silicon has been the prevalent backbone for the existing microelectronic infrastructures and the foundation of complementary metal-oxide-semiconductor (CMOS) transistor devices. It is difficult, however, to utilize silicon for optoelectronic devices, since it is an indirect bandgap material. Direct bandgap materials that exhibit superior proficiencies in optical processes are traditionally group III-V compound semiconductors, which on the other hand, are not as cost effective as silicon. Integrating III-V semiconductors onto silicon can therefore pave the way towards a highly compact optoelectronic platform combining the strengths of both materials.

In order to be integrated onto silicon platform, it is required that the foreign materials are fully compatible with silicon processes, especially with modern CMOS technology. Existing technologies to integrate III-V on silicon include: (a) monolithic growth, (b) direct wafer bonding, and (c) indirect wafer bonding, as summarized in Figure 2.1 [18].
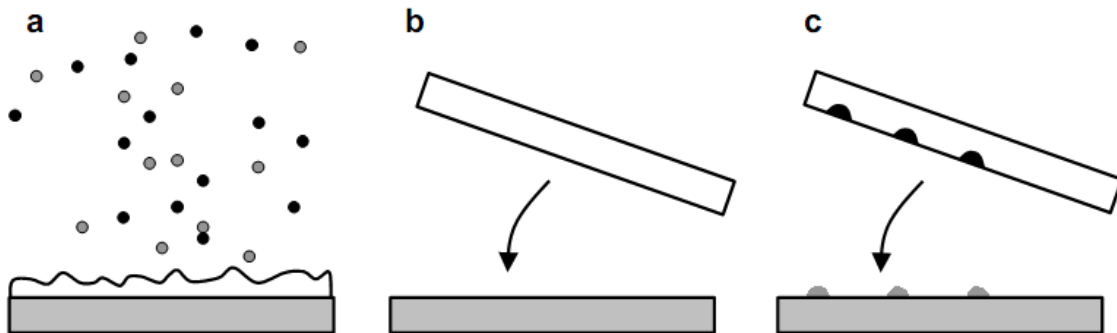
Figure 2.1 Main existing technologies to integrate III-V on silicon substrate. (a) Monolithic growth; **(b)** Direct wafer bonding; **(c)** Indirect wafer bonding. Figure is adapted from [18].

Bottom-up growth of III-V materials on silicon substrate provides a possible pathway towards this goal. But it remains highly challenging due to the fundamental incompatibilities mainly in lattice mismatch and synthesis temperatures between these two materials. Although lasers have been demonstrated with this approach [19], the large lattice mismatch results in poor III-V thin film quality and device performance [20]. As semiconductor nanostructures have been the key enablers in several diverse application areas, their unique properties help bypass these roadblocks and open up a new landscape in optoelectronics. In Fig. 2.2, epitaxy on lattice-mismatched substrates often results in severe dislocations, while the smaller footprints of nanowires can somewhat accommodate strain and allow dislocation-free heterogeneous material integration [18]. Tomioka and Fukui et al. have provided comprehensive reviews of III-V nanowires on silicon substrate [21], [22], including pioneer work on metal-catalyzed vapor-liquid-solid growth [23]- [26], catalyst-free growth [27]- [30], as well as selective-area growth [31]- [33]. However, these methods of growing nanowires require either the use of gold catalyst [23]- [26], or relatively high growth temperature (usually >550 ºC) [28]- [36], which are both CMOS post-process incompatible [29], [32], [37]. To explain further, Takeuchi et al investigated the thermal budget limits for 250-nm foundry CMOS for post-processing MEMS devices, which should be applicable to all CMOS post-processing devices [37]. According to their study for 250-nm foundry, resistance increases for vias (metal-to-metal contacts) rather than transistor-performance shifts limits the post-processing thermal budget. With a criterion of 10% increase, 6 hr at $425\,°C$, 1 hr at $450\,°C$, and 0.5 hr at $475\,°C$ are the maximum allowable thermal budgets, respectively. Most of the catalyst-free growths, as far as we know, took place above $550\,°C$ actually. This tight thermal budget puts a limit to growth time and is not applicable in most cases, especially as most foundries enter sub-100-nm era. In addition, the existence of critical dimensions [38], leading the diameters of these nanowires to be well below 200 nm in general, results in poor optical confinement and large surface to volume ratio, thus hampering their optoelectronic performance. Thereby, a complete photonic integrated circuit (PIC) has been an unfulfilled feat with traditional nanowires grown on silicon.
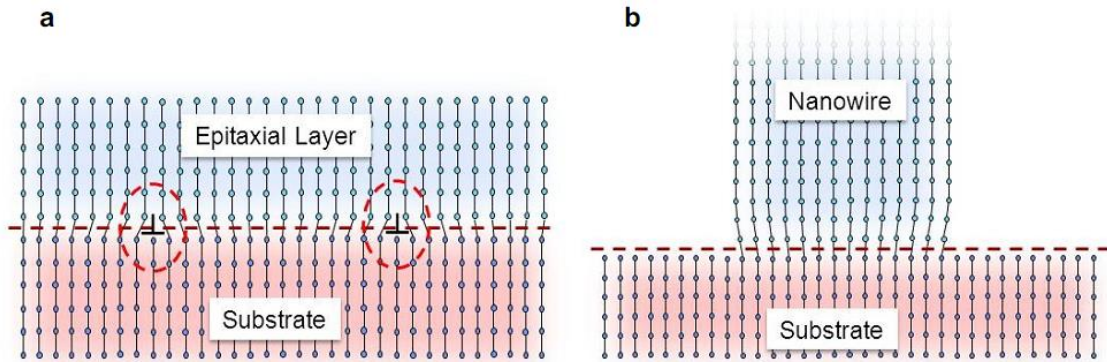
Figure 2.2 Lattice mismatch (a) causes dislocations in epitaxial III-V layers on silicon, but **(b)** nanowires with small footprints can accommodate it. This figure was adapted from reference [18].

Top-down bonding of III-V materials onto silicon wafers was also extensively studied. With this approach, incompatibilities due to lattice mismatch and growth temperature are mitigated. However, direct wafer bonding inevitably requires pristine material and surface conditions [39] [40]. Thus it is extremely difficult to achieve wafer-scale bonding on a post CMOS-process wafer due to its highly complex terrain. On the other hand, it is also not possible to perform bonding before CMOS-process, as III-V is not tolerated in most silicon processes. The only solution left is to bond small dies of III-V onto wafers with CMOS electronics already fabricated. In this case, both scalability and yield pose a challenge, on top of the still difficulty bonding process.

The last major approach of III-V integration with silicon is through indirect wafer bonding. Different from direct wafer bonding, an intermediate layer consisting of metal, epoxy, solder balls or other materials fills the voids between silicon and III-V to hold them together [18]. The surface imperfection is thus tolerated, at the expense of an interlayer which may be complex and expensive. Furthermore, the patterning and alignment required for bonding greatly constrains fabrication process flows in an intolerable manner. Plus scalability and yield still remain as a challenge for indirect wafer bonding.

The above three main approaches of integrating III-V on silicon clearly do not fully satisfy the requirement of CMOS compatibility. The obstacles include choosing the right material, processing at the right temperature, and debating between integration at the front-end-of-line or back-end-of-line. These dilemmas are difficult, and for that reason, some prefer to implement silicon optoelectronics by using traditional electronic materials like germanium or silicon itself. This will be the topic of the next section.

2.1.2 Group IV photonics

Silicon (Si), the second most abundant element in Earth's crust, also possesses many desired properties for electronic processes which have made it the backbone for modern electronics. This motivated many to pursue the acquisition of silicon for integrated optoelectronics hoping it would control photonics on the similar level as controlling electronics. Germanium (Ge), another group IV element, has also received similar attention benefitting from its inherent compatibility with silicon.

However, a big roadblock stopped the dream of pure silicon optoelectronics from coming true. For indirect band gap structure, radiative carrier recombination obeying momentum conservation is extremely difficult and only occurs on the rare occasion when sufficient phonon assistance is offered. While both silicon and germanium are endued with wonderful properties in terms of light detection, guiding, modulating, and processing, the indirect band gap of group IV elements keeps them away from efficient light emission.

Despite the fundamental difficulties, impressive improvements have been made throughout the years. For silicon, nanostructures and texturing have been the key to achieving optical gain. Even silicon light-emitting diodes (LEDs) with over 1% efficiency have been fabricated. For germanium, the ability to engineer strain and doping has provided a powerful means of improving light emission [18]. Recently, even an electrically-injected germanium laser on silicon

was demonstrated [41]. Eventually, energy efficiency might be a bottleneck for these lasers made out of indirect bang gap materials to become applicable.

2.1.3 Our Approach

Our group has developed a unique growth mechanism to grow GaAs-based and InP-based nanoneedle/nanopillar/micropillar structures on a variety of lattice-mismatched substrates [1]-[4]. The discovery of nanoneedles on silicon was serendipitous, but their development was fervently pursued after immediately recognizing their potential for optoelectronic devices [42] [43].

The unique core-shell metastable growth mechanism possesses three key advantages over conventional nanowire growth methods, especially when it comes to optoelectronic integration on silicon. First of all, the growth occurs without any external catalyst like gold in VLS growth method, which would otherwise be poisonous to silicon devices. In addition, they are synthesized by low-temperature (400 ~ 460 ºC) metalorganic chemical vapor deposition (MOCVD), thus the growth condition was verified to be CMOS-compatible [5]. Furthermore, the unique core-shell growth mode also allows the base diameters of nanoneedles/nanopillars to scale with growth time, up to far beyond lattice-mismatched critical dimensions while still preserving single crystalline quality in the body [6].

To differentiate the names including "nanoneedle", "nanopillar", and "micropillar", Figure 2.3 is introduced here. Fig. 2.3 (a) shows a scanning electronic microscope (SEM) image of a GaAs nanoneedle, while Fig. 2.3 (b) shows one of InGaAs nanopillars. Nanoneedles and nanopillars share the same growth mechanism, but their geometries differ and are controlled by subtle variations in growth parameters such as temperature and material composition. Nanopillars can also be categorized as a subset of nanoneedles exhibiting truncated and flat tops. When the base diameter of nanoneedle/nanopillar exceeds $1\mu m$, it is referred as "micropillar" in this context. Fig. 2.3 (b) meanwhile demonstrated the flexibility of nanoneedles to grow on a variety of lattice-mismatched substrates, such as polysilicon in this case. Past experiments also reported growth on GaAs substrates and even insulators such as sapphire [2], [44].
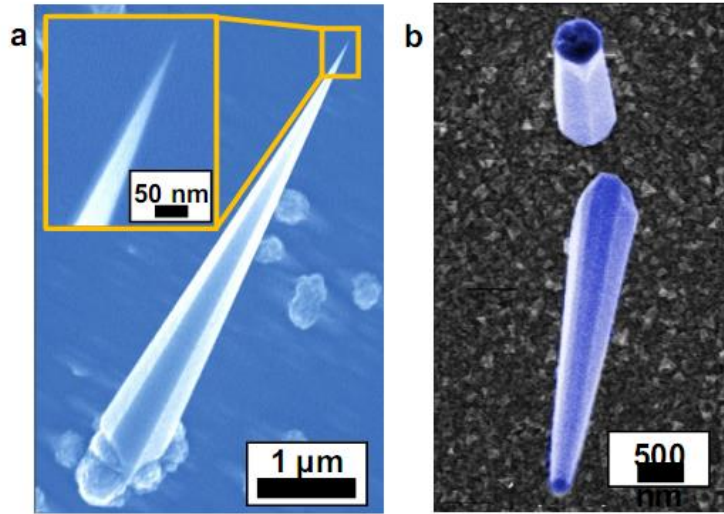
Figure 2.3 SEM images of nanoneedles and nanopillars on silicon. (a) An SEM image showing a GaAs nanoneedle grown on silicon substrate, adapted from ref. [2]. The nanoneedle tapers down to an atomically sharp tip as highlighted by the inset. **(b)** An SEM image showing nanopillars with truncated tops grown on polysilicon substrate, adapted from [3].

Being able to scale up in size overcomes the long-standing drawback of nanowires whose large surface-to-volume ratio induces severe surface recombinations. This also has practical implications from a device perspective. Microstructures are often more well-suited for optical devices, because their size can host more than one wavelength of the light and bigger structures can better survive the rigors of fabrication processes. The large size empowers the optical performance of our micropillars vastly, eclipsing traditional nanowires in optoelectronic functionality. This integrated material template has enabled high-performance optoelectronic devices for light emission [1], [45]- [47], light detection [45], [48], [49], and photovoltaics [50]. An integrated optical link was also demonstrated in Figure 2.4, showing the potency of the micro/nano-structures for optical interconnect with higher speed and lower power consumption than their traditional electrical counterparts [51]. This can be crucial, to the increasing bandwidth demands of communication network. In the rapidly growing field of photovoltaics, cost is becoming the major competition factor. While III-V nanowires offer strong light absorption and potential for high energy conversion efficiency, the use of native substrates is yet very expensive. Integration of III-V micropillars on silicon substrate incurs minimal real estate cost while still offering full functionality, and thus promises the realization of high-efficiency and cost-effective solar cells.
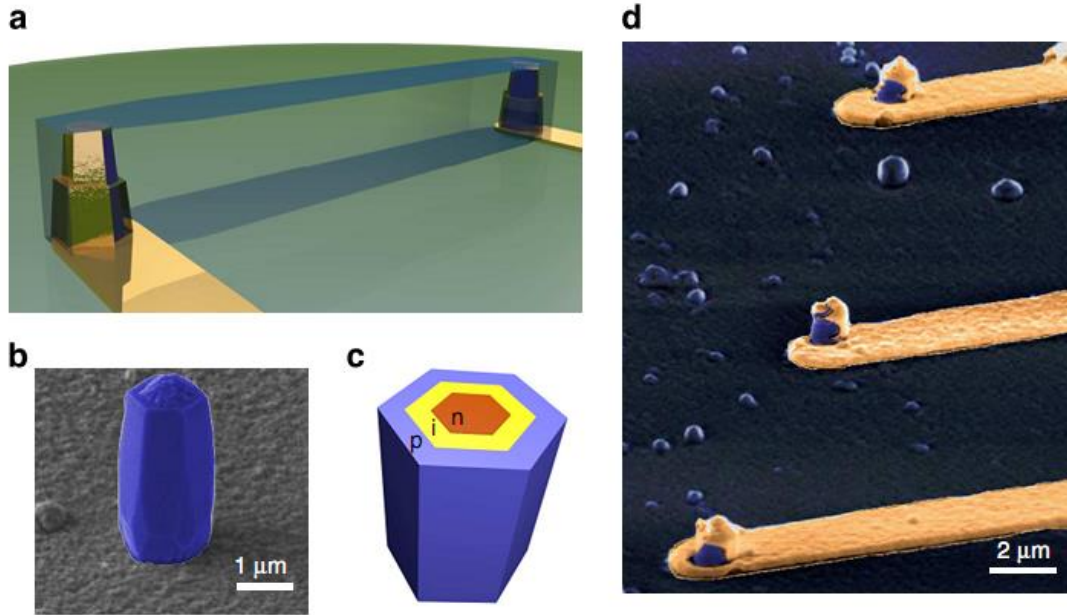
Figure 2.4 Assembling photonic circuits via nanostructure growth. (a) A schematic of an optical link formed by interconnecting two optoelectronic devices fabricated from GaAs-based nanoresonator structures grown on silicon. **(b)** An SEM image shows the hexagonal nature of the as-grown resonator. **(c)** Through core-shell growth, radial p-i-n junctions form within each structure, providing the basis of our nano-optoelectronic devices. **(d)** An SEM image shows a fabricated array of such device. Figures are adapted from [51].

2.2 Indium Phosphide Nano/Micropillars Grown on Silicon

Located at the center of "Energy Gap versus Lattice Constant" chart for semiconductors [52], InP is an ideal candidate as a growth template to bridge silicon and alloys of compound semiconductors. Hence InP micropillars grown on silicon are particularly suitable for developing communication wavelength on-chip laser sources, as well as multi-junction high efficiency solar cells. Most importantly, with a very low surface recombination velocity (SRV), InP-based nanostructure is less susceptible to recombination at free surfaces [53]. Being able to scale the single crystalline structures with diameter exceeding 1 µm further facilitates high photon luminescence yield and outstanding optical characteristics [7]. Given the superior material quality, a thorough material characterization is necessitated in order to understand the growth mechanism and to better harness it. In the three sections below, we aim at answering the following questions through various characterization techniques: (1) how InP grows on silicon and how stress is relaxed around the hetero-interface; (2) how InP micropillar remains single crystalline when its diameter is far beyond the critical value.

2.2.1 Growth

Growth of InP nanostructures studied here occurred on (111)-silicon substrate at 450-460 ℃ in an Emcore D75 MOCVD system. Details of growth can be found in ref. [4]. Trimethylindium

8

(TMIn) and tertiarybutylphosphine (TBP) were adopted as indium and phosphorus precursors, respectively. Prior to growth, the silicon substrate was cleaned with acetone, methanol, and rinsed with DI water. The substrate was then deposited with SiO_2 and exposed with photolithography, the surface was then chemically treated with TMAH (tetramethylammonium hydroxide). TBP was flown into the reactor when substrate temperature was higher than 200 ℃. A pre-growth *in-situ* annealing was performed at 540 ℃ for 3 min. Reactor temperature was then lowered and kept at the growth temperature, which ranged from 400 to 460 ℃. TMIn was introduced into the reactor afterward to prevent self-catalyst effect of indium at low temperature. The total flow rate during the growth was fixed as 12 slm. The mole fractions of TBP and TMIn were held as 2.36 x 10^{-3} and 1.89 x 10^{-5} respectively.

The growth results in nano- and micro-pillars with tapered sidewalls whose size is scalable by growth time. Inside the exposed areas, the pillars are randomly distributed. As shown in the large scale scanning electron microscopy (SEM) image in Figure 2.5 (a), both upright and slanted micropillars stem along the equivalent <111> directions of silicon. We obtained at least one upright InP pillar per 40 μm^2 area. Since each single micropillar is large enough, it will be processed and used as a single device, as evident by the optically pumped laser [7]. Hence, different from the cases where an ensemble of nanowires would be required to function as a laser [54], or a single nanowire needed to be removed from the native substrate and optically pumped from the side [36], [55], [56], high density may be neither necessary nor desirable. However, periodic and precise-position-controlled growth is indeed more desired and is the next goal to work towards, upon which better control of pillar orientation can also be realized. Despite the stochastic nature, our nanostructures can be repeated for more than 500 runs. This reproducibility signifies the potential of this work as an important pathway for heterogeneous integration.

The substrate we used in this work is (111)-Si, which is not compatible with CMOS processes, where (100)-Si is commonly used. As studied by one of our previous papers [5], we grew InGaAs/GaAs nanopillars on (100)-Si-based functional metal-oxide-semiconductor field effect transistors (MOSFETs). The MOSFETs were shown to have maintained their performance after the nanopillar growth, providing a direct demonstration of CMOS compatibility. Room-temperature operation of optically pumped lasers was also achieved. In order to control the orientation of nanopillars, as an example, part of the (100)-Si substrate was etched to expose Si (111) planes using an anisotropic Si etchant TMAH. It was shown that nanopillars can grow on Si (111) planes with a predetermined orientation. In the case of InP pillars reported here, (111)-Si substrate was chosen first, for the ease of characterization and device fabrication. In the future, similar study will be pursued as in the InGaAs/GaAs case above. The InP pillars can be grown on the Si (111) facet etched on the (100)-Si substrate, to be CMOS process compatible. More studies are in progress in terms of characterization and device fabrication.

Figure 2.5 (b) exemplifies a micropillar grown at 450 ℃, which possesses a diameter of about 1 µm, and height of ~8.9 µm. The pillars assumed a hexagonal pyramidal shape, similar to our previously reported InGaAs-based structures grown on silicon. However, there is a distinct difference between the growth of InGaAs and InP micropillars. In the former case, a continuous polycrystalline film is found to cover the entire substrate and embrace the base of the single crystalline pillars. In fact, this poly-InGaAs layer grows simultaneously with the InGaAs pillars and prevents the very bottom part of the pillars from expanding. As the growth proceeds, an inversely tapered 'root' forms at the bottommost portion of the pillar. Such tapering effectively

shrinks the exact InGaAs/Si contact area to ~60 nm in diameter, thus reducing the strain energy accumulating within the III-V structure [6]. In the growth of InP pillars, however, no continuous poly-InP layer is observed [4]. This can be attributed to the long diffusion length of indium adatoms, as well as the large lattice mismatch between InP and silicon. Compared to $In_{0.2}Ga_{0.8}As$ (lattice mismatch ~ 6% with Si), InP experiences a much higher misfit strain (~ 8%) with the heterogeneous substrate. The much higher elastic energy due to larger lattice mismatch in the latter can effectively inhibit the wetting of InP on silicon. In addition, the presence of Ga in the ternary compound also changes the wetting behavior of the material. Since Ga has a much shorter diffusion length than indium, we believe that Ga settles down readily on the substrate without much clustering and acts as nucleation sites for the subsequent nanostructure and polycrystalline layer growth. Indium, which can diffuse much longer distance, tends to form large and sparsely distributed clusters before anchoring to the substrate for pillar nucleation. These two factors result in the formation of continuous layer in InGaAs but not in InP. In the absence of a poly-InP layer wrapping around, the entire pillar base is in direct contact with the substrate. With a lattice mismatch as high as 8% between InP and silicon [38], a large footprint implies a huge amount of elastic energy built up in the structure. A stress relaxing mechanism must exist around the interface such that the InP pillars can remain single crystalline when the lateral size scales up to close to a micron.
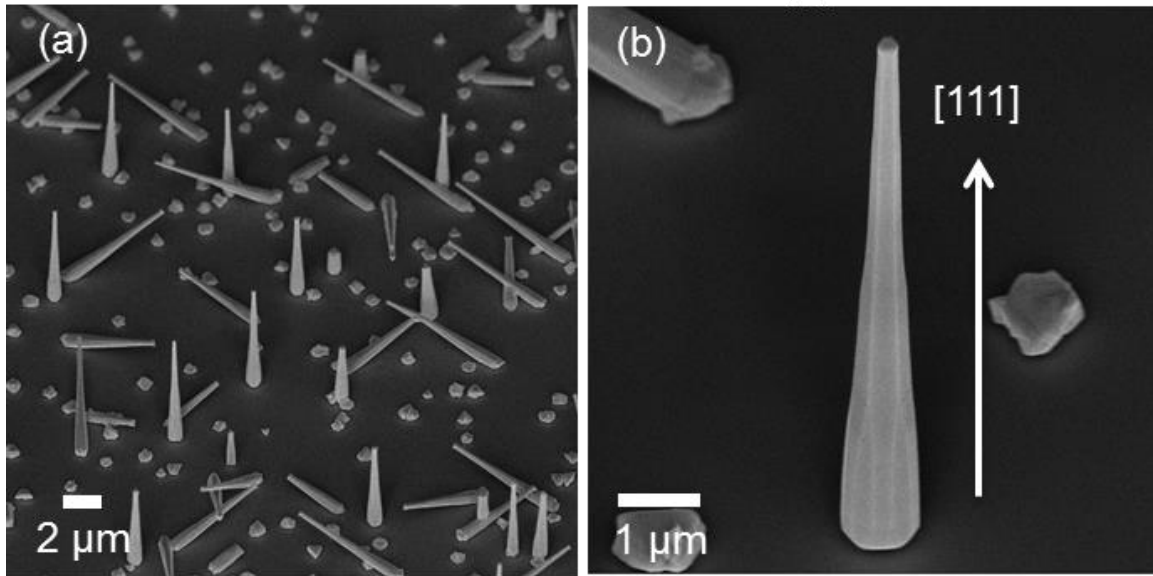
Figure 2.5 InP micropillars and InP/Si interface. (a) 45° tilt view of an ensemble of upright and slanted pillars grown on silicon substrate, as seen by scanning electron microscopy (SEM). **(b)** 45° tilt view SEM image of a typical upright micropillar. The image reveals a pillar with tapered sidewalls, hexagonal cross-section, diameter of ~1.0 μm and height of ~8.9 μm. [8]

To further prove that the growth indeed assumes core-shell mode, $InP/In_{0.2}GaAs/InP$ double heterostructure was demonstrated [4]. The InP core diameter is designed as 450 nm, while both of the InGaAs layer and InP shell thicknesses are chosen as 100 nm. The structural schematic

10

and 30º-tilt SEM image of the nanopillar are shown in Figure 2.6 (a) and (b), respectively. It is considered that the flat top results from the InGaAs layer growth. Due to the growth condition variation across the sample surface, some short nanopillars with a height of ~320 nm are also found. InGaAs layer is exposed on the top of those short nanopillars. The InGaAs layer can be removed by selective wet etching while leaving InP layers intact, resulting in a trench between two InP layers, as shown in Figure 2.6 (c). The measured thickness of InGaAs intermediate layer and InP shell agree with the designed ones. Two smooth boundaries of the trench can be seen at the original InGaAs/InP interfaces. It indicates that good interfaces are formed between the two materials. Furthermore, suggested by the excellent appearance of outer interfaces, the 100-nm-thick InGaAs layer could grow with a good crystal quality, despite over 2% lattice-mismatch respect to InP. The ability of growing double heterostructure further confirms that the InP nanoneedle growth follows a core-shell manner. Furthermore, it also reveals a potential approach to integrate high-performance optoelectronic devices in silicon transparency range monolithically with silicon.
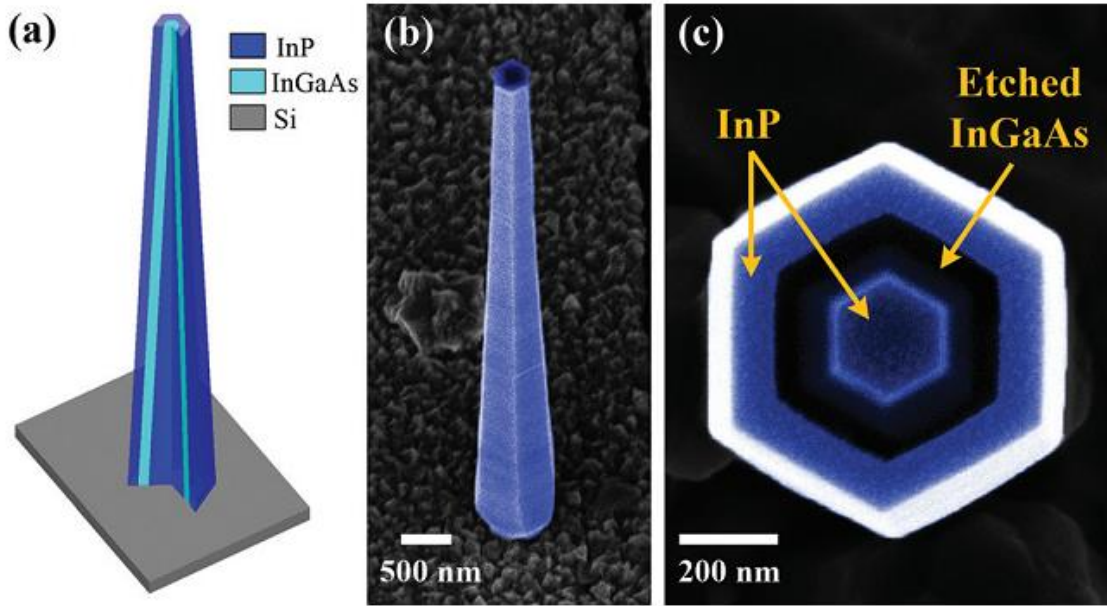
Figure 2.6 Nanopillar with InP/InGaAs/InP double-heterosturcture. (a) Schematic illustrating the core-shell structure of the nanopillar. **(b)** 30º-tilt SEM image of InP/InGaAs/InP nanopillar. **(c)** Top-down view of a nanopillar with InGaAs layer removed by selective etching. Figures are adapted from [4].

2.2.2 Crystal Phase

Due to the nature of nanostructures, mutation of the crystal structures occurs during growth. Crystal phase is an important perspective to study the material, and strongly relates to the optoelectronic performance of the device later on. Therefore, it is necessary to introduce the background of crystal structure for III-V materials here. More detailed description can be found in [57].

A crystal or crystalline solid is a solid material whose constituents (such as atoms, molecules or ions) are arranged in a highly ordered microscopic structure, forming a crystal lattice that extends in all directions. In III-V crystals, the atoms are all in sp^3 hybridization. Each III- (or V-) atom is bonded to four V- (or III-) atoms, resulting in a tetrahedral configuration. Each bond is a single bond formed by overlapping of sp^3 orbitals. With the absence of π-electron overlap, the two groups linked together by a single bond can rotate freely with respect to each other. Two rotational eigenstates – staggered state and eclipsed state, are of particular interest.

In theory, each covalent bond in a sp^3 hybridized system can be either staggered or eclipsed. To form a closely packed atomic layer, 3 of the 4 covalent bonds have to be in staggered state. The remaining covalent bond, which is responsible for inter-layer linking, can be either staggered or eclipsed. This freedom subsequently gives rise to the two most common crystal phases in III-V materials – zincblende (ZB) and wurtzite (WZ) structures. ZB structure, consisting of purely staggered bonds, is usually more energy favorable due to its higher degree of symmetry. On the other hand, WZ structure is considered asymmetric due to the presence of an eclipsed bond along c-axis or [0001]. Thus, the major difference between ZB and WZ structures is how the atomic layers are linked together. The staggered bonds in ZB structures along c-axis leads to an ABCABC stacking sequence of the atomic layer, while the eclipsed bonds in ZB result in an ABAB sequence. Figure 2.7 shows how the atoms are stacked in ZB and WZ structures.
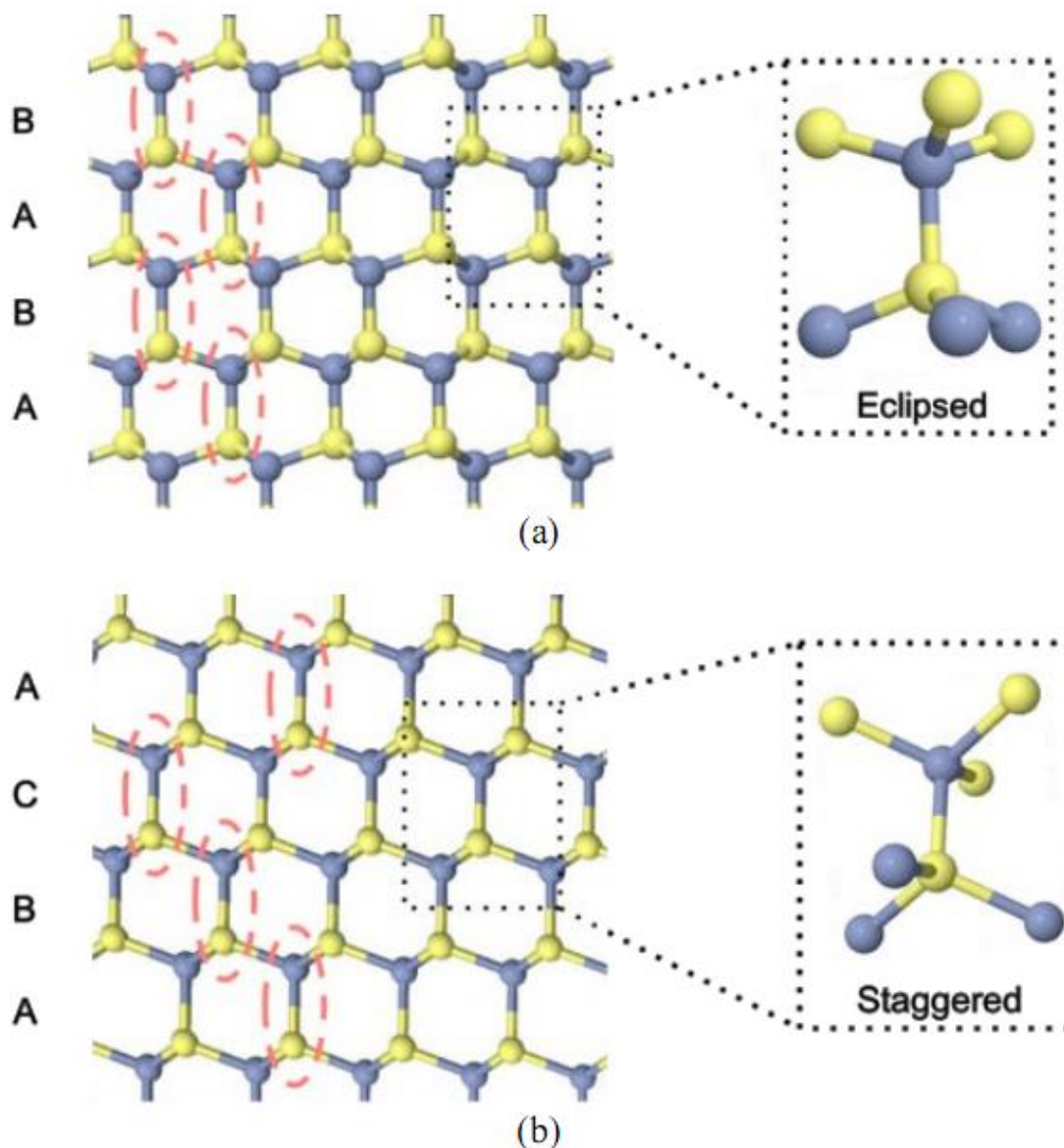
Figure 2.7 Schematic diagrams of (a) Wurtzite and **(b)** Zincblende lattices. Red circles highlight the position of the concerned III-V pair in each layer. These schematics are adapted from [57].

In staggered conformation, the separation between an atom and its third nearest neighboring atom is the farthest, thus minimizing the repulsion between the air. On the other hand, eclipsed conformation exhibits mirror symmetry and allows maximum attraction for the aforementioned pair. In a III-V crystal, the third nearest neighbor of a III-atom must be a V-atom, and vice versa. If the compound involves elements with high electronegativity, the bond becomes highly polarized with electrons pulled towards that element (e.g. N in a GaN crystal). This polarization induces attractions between the third nearest neighbors and thus favors the eclipsed state. However, if the bond is highly covalent (e.g. Ga-As and In-As bonds), electrons are more fairly

13

shared between the two elements and thus more confined within the bond. Attraction between the third nearest neighbors is negligible. In this case, a staggered configuration is preferred to lower repulsion between the neighboring bonds. A more accurate way to determine the favorable crystal phase in III-V material is to calculate the free energy, with lower value being more stable. The result shows that nitride compounds prefer WZ phase (except for BN), all the other III-V compounds are more stable in ZB phase. This agrees well with the predictions based on ionicity theory.

For nanostructures whose surface energy can no longer be neglected, free energy experiences change compared with its bulk form. In general, nanostructures grow along [111] in ZB or [0001] in WZ. The sidewalls of the nanowire, which contribute to most of the surface areas, are composed of planes perpendicular to the growth directions. In ZB, the sidewalls are along $\{1\bar{1}0\}$ and $\{\bar{2}11\}$, while for WZ the equivalent planes are $\{1\bar{1}00\}$ and $\{11\bar{2}0\}$. The same number of dangling bonds are broken when creating ZB $\{1\bar{1}0\}$ and WZ $\{11\bar{2}0\}$, thus they have the same surface energy. On the other hand, 4 dangling bonds are broken when exposing ZB $\{\bar{2}11\}$ surface, but only 3 are broken for WZ $\{1\bar{1}00\}$ surface. Therefore, on average, WZ crystal has a lower surface energy than its ZB counterpart.

Depending on surface-to-volume ratio, WZ structure is more favored for nanowires below critical diameter (~100 nm) for surface energy to be accounted for. This has been reported on nanowire growth via VLS and selective area growth [38]. As the diameter expands further, nanowire tends to evolve into a mixture of WZ and ZB phases. However, our unique growth mode leads to micropillars with pure WZ crystal phase. The next section will explain more about the growth mechanism and how this could happen. This peculiarity gives rise to many unique properties in WZ crystals, including the presence of spontaneous and piezo-electric fields [57], strong 2nd harmonic emission [58], etc. In addition, WZ crystals have polarization dependence on crystal orientation and different band structures from ZB crystals, which will be further discussed in Chapter 3.

2.2.3 Material Characterization

To study how single crystalline InP stems on silicon, we studied the InP/Si interface with high resolution scanning transmission electron microscope (HR-STEM). All the high resolution high angle annular dark field (HAADF) images were taken with the transmission electron aberration corrected microscope (TEAM I) operated at 80 kV at the National Center for Electron Microscopy, Lawrence Berkeley National Lab. In STEM mode, the best resolution can be as small as 0.1 nm. Sample preparation involves the use of focused ion beam (FIB) and micro-manipulator to create a thin slice, or a lamella, of the hetero-interface. In particular, we chopped off the top part of the InP pillar with ion beam such that only the bottommost ~400 nm remained. Pt was then deposited onto the frustum to passivate the hetero-interface in the subsequent top-down ion beam milling. These special treatments help minimize curtaining effect (i.e. roughening of the lamella surface) that would have occurred if the pillars were thinned down in full length. Figure 2.8 (a) shows an SEM image of the pillar cross-section halfway through the milling process. The entire pillar base, with a width of ~900 nm, is indeed in direct contact with silicon without any inverse tapering. The sample was first aligned along the [1$\bar{1}$00] zone axis of InP. Since ZB [$\bar{2}$11] looks exactly the same as WZ [1$\bar{1}$00], any stacking faults would be

invisible along this orientation. This simplifies the identification of any misfit defects that may appear at the interface. Figure 2.8 (b) displays an HAADF image of the InP/Si interface. Since indium has a much larger atomic number than silicon, InP appears to be much brighter than silicon in the z-contrast image. We note that the hetero-interface is a little blurry due to the nanoscopic roughness induced by TMAH etch prior to the growth to facilitate pillar nucleation. The lattice continues seamlessly from silicon to InP in spite of the blurriness at the interface. In particular, silicon is aligned with InP in a way that Si [$\bar{2}$11] // InP [1$\bar{1}$00] and Si [111] // InP [0001]. These observations indicate that InP pillars do nucleate directly on silicon without any amorphous materials in between. Such direct contact is a necessary condition for good electrical conductivity across the hetero-interface, which is crucial to fabricating real devices on silicon.

Information in the reciprocal space can reveal the strain state of InP close to the hetero-interface. Figure 2.8 (c) displays the Fast Fourier Transform (FFT) of the HAADF image in Fig. 1d. Two sets of diffraction spots, belonging to InP and silicon, can be clearly seen. Diffractions from InP (wurtzite lattice) and silicon (diamond lattice) are registered with 4-digit Bravais-Miller indices and 3-digit Miller indices, respectively. In particular, the diffractions of InP 11$\bar{2}$2 and Si 1$\bar{3}$1 are collinear with the transmitted beam at the center. This indicates that InP and silicon are relaxed to their own lattice spacing rather than strained to accommodate for the lattice mismatch elastically. To find out the origin of the stress relaxation mechanism, we applied filtering in the spatial frequency domain such that only the InP 11$\bar{2}$0 and Si 0$\bar{2}$2 diffraction pairs remain. Figure 2.8 (d) illustrates the corresponding filtered image in real space, revealing vertical (11$\bar{2}$0) planes in InP and (02$\bar{2}$) planes in silicon only. Most of the InP (11$\bar{2}$0) planes in the upper half are seen to stem seamlessly from the Si (02$\bar{2}$) planes below. However, there exist some locations at where one InP (11$\bar{2}$0) is connected to two Si (02$\bar{2}$), as indicated by red arrows. These are in fact misfit dislocations that propagate along the [1$\bar{1}$00] direction. When connected together, the five misfit dislocations outline the contour of the silicon surface, attesting to the roughening effect of TMAH etch during sample preparation. Moreover, the planes in the vicinity of the misfit dislocations are considerably bent, revealing the presence of strain in these regions. Interestingly, these dislocations appear periodically in every 12th or 13th InP (11$\bar{2}$0) planes. On average, 27 Si (02$\bar{2}$) planes are matched with 25 InP (11$\bar{2}$0) planes in the presence of dislocations. The ratio of the two numbers, 1.08, accounts for exactly 8% lattice mismatch between silicon and InP. We believe that these periodic misfit dislocations effectively relax the misfit stress between the two materials [59], [60], leading to the high-quality growth in the bulk material of the pillar that is remote from the hetero-interface.

15
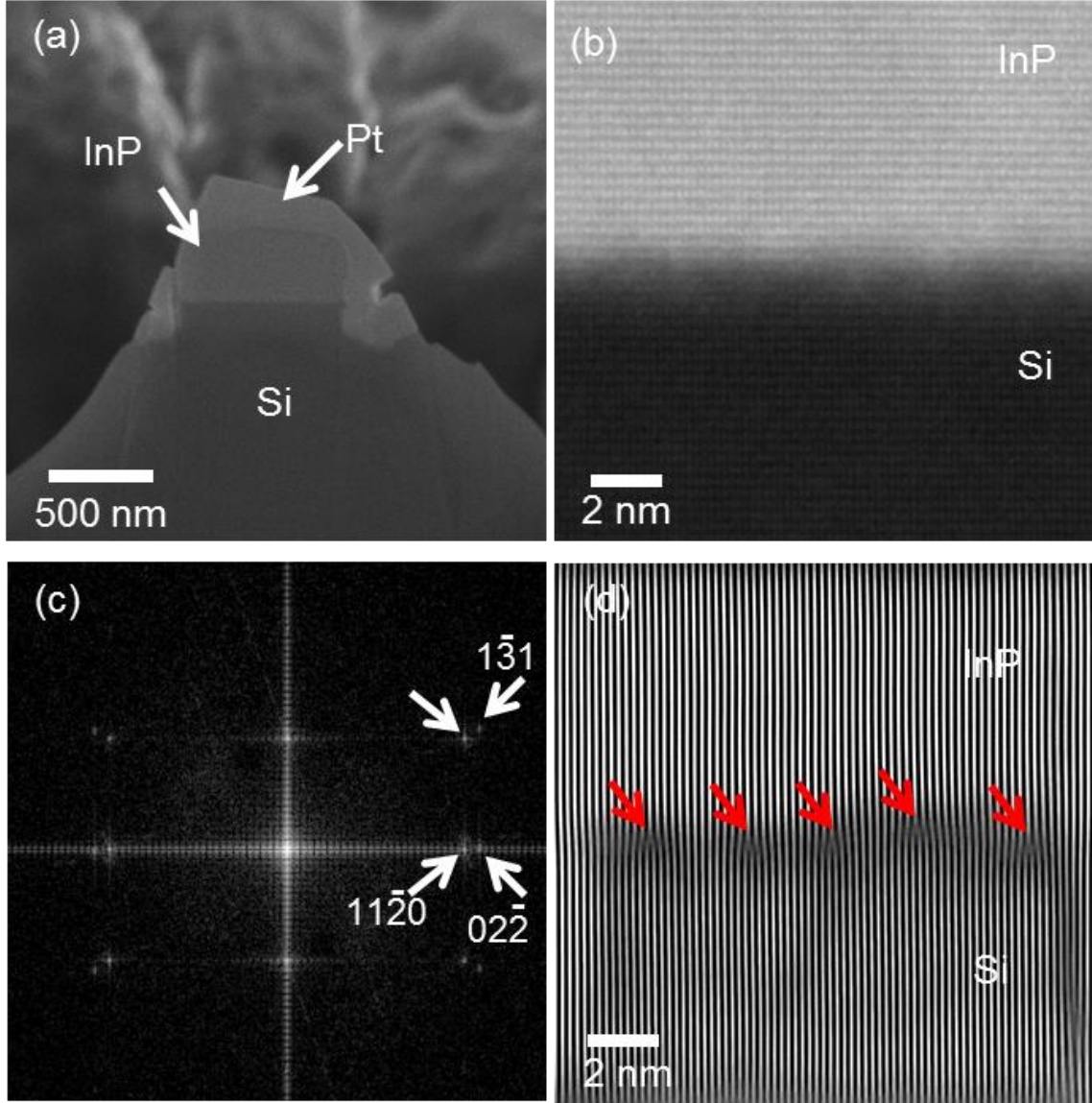
Figure 2.8 InP micropillars and InP/Si interface. (a) SEM image of a pillar cross section prepared by FIB. Pt is used as the passivation layer for top-down ion beam milling. The entire InP pillar is seen to stem on top of silicon without any tapering at the base. **(b)** HAADF image showing the exact InP/Si interface taken along the $[1\bar{1}00]$ direction. **(c)** FFT of the high-resolution image in (b). **(d)** By applying filtering in the FFT such that only the **$11\bar{2}0$** and **$02\bar{2}$** diffraction patterns remain, periodic dislocations (indicated by red arrows) can be clearly observed at the hetero-interface. [8]

While misfit dislocations can be clearly identified along $[1\bar{1}00]$, stacking disorders can only be seen along $[11\bar{2}0]$. Figure 2.9 (a) displays a HAADF image of the interface taken along the $[11\bar{2}0]$ zone axis. InP is observed to grow directly on silicon along the entire 90-nm interface, although the border is a bit uneven due to nano-roughening during TMAH etch. Figure 2.9 (b) shows the hetero-interface at higher magnification. Immediately above the InP/Si interface is a transition region composed of ZB-phased crystal with stacking faults and twinnings. InP then

16

stabilizes into WZ phase above this 4-nm transition region. We attribute the formation of stacking disorders to the very high growth rate during the initial nucleation stage. The high deposition rate possibly inhibits the adatoms from migrating to the most energy favorable sites before incorporating into the lattices. When the growth slows down and stabilizes later on, the large surface-to-volume ratio favors the formation of WZ lattice, which subsequently becomes the dominant crystal phase in the micropillar growth. Figure 2.9 (c) displays the zig-zag arrangement of the pure WZ InP lattice under high magnification, resolving individual atomic columns clearly in the binary compound. Since indium is much heavier than phosphorus, the former appears much brighter and larger in size in the z-contrast image. Nevertheless, one can still observe the polarity clearly from the highly asymmetric dumbbells – the tiny phosphorus atom is sitting on top of the gigantic indium atom in the pair. This configuration implies that the top facet of the pillar is terminated with group V. A group V terminated surface is believed to be more stable [21] and is consistent with what we observed in InGaAs nanopillars [61] and other nanowire work. Remarkably, pure WZ phase is very hard to achieve for InP nanowires, except for a few cases reported on InP substrate with relatively high growth temperatures [56], [62], [63]. When growing on a lattice-mismatched substrate under a CMOS post-process compatible temperature, it is extra challenging. These metastable micro-structures therefore provide lots of possibilities for exploration of new physics as well as unprecedented functionalities.
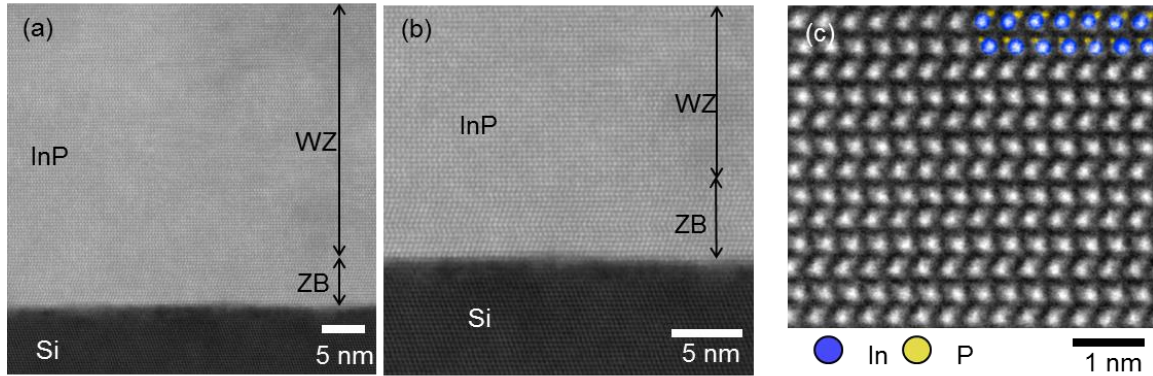
Figure 2.9 Crystal phase of InP pillars. (a) HAADF image showing the exact InP/Si interface taken along the [$11\bar{2}0$] direction. ZB phase is found at the bottommost ~4 nm above the InP/Si interface. **(b)** Zoom-in view of the InP/Si interface. **(c)** High resolution HAADF image showing the polarity of the InP crystal in the micro/nano-structure. The top facet is terminated with Phosphorus atoms. [8]

To further study the epitaxial relation between InP and silicon, X-ray power diffraction (XRD) would be an excellent technique to apply on a large ensemble of wires. In our case, however, the density of pillars is much lower than other nanowire work. This can be observed from the SEM image in Figure 2.5 (a). With such a low surface coverage, the signal obtained from the nano- and microstructures would be too weak and board for meaningful analysis. Instead of XRD poles, we can study the epitaxial relation between InP and silicon of a large number of pillars through their growth orientations. As revealed in the low magnification SEM image in Figure 2.5 (a), the pillars are growing only along the four identical <111> directions of the silicon substrate. Such observation suggests that $[0001]_{InP}//<111>_{Si}$. In addition, such

17

epitaxial relation has also been observed in cross sectional TEMs as shown above of nearly 10 different samples grown with different orientations. We believe these observations would be sufficient to show the epitaxial relation between InP and Si.

2.3 Summary

In summary, direct growth of III-V nanostructures on the silicon-based microelectronic platform provides a pathway towards heterogenous optoelectronic integration. Our method of growing III-V nanoneedles/nanopillars on silicon substrate is superior to traditional nanowire growth benefiting from its unique core-shell mode growth mechanism by low-temperature MOCVD without any external catalyst. The diameter of the pillars can then go far beyond the lattice-mismatch critical dimension and offer outstanding optical gain and other optoelectronic characteristics. Furthermore, the growth condition can be adjusted to achieve single crystalline pure wurtzite phase, which is ideal for achieving optimal optical efficiency. Among the III-V materials, InP stands out as a promising material platform for laser sources, solar cells, photodetectors, as well as other integrated optoelectronic devices.

Chapter 3
Tailoring the Optical Characteristics of Micro-sized InP Nanoneedles Grown on Silicon

This section reports distinct optical characteristics of InP nanoneedles which are varied from mostly-zincblende, zincblende/wurtzite-mixed, to pure-wurtzite crystalline phase. We achieved, for the first time, pure single-crystal wurtzite-phase InP nanoneedles grown on silicon with bandgap 80 meV larger than that of zincblende-phase InP. Being able to attain excellent material quality while scaling up in size promises outstanding device performance of these nanoneedles. At room temperature, a high internal quantum efficiency of 25%, and optically-pumped lasing are demonstrated for single nanoneedle as-grown on silicon substrate. Recombination dynamics proves the excellent surface quality of the InP nanoneedles, which paves the way towards achieving multi-junction photovoltaic cells, long-wavelength heterostructure lasers, and advanced photonic integrated circuits.

3.1 Photoluminescence

Optical characterization is paramount for leveraging III-V material for better performance in optoelectronic integration. Photoluminescence (PL) is a powerful tool to probe the fruitful process in light-matter interaction. Part of its utility is in the elegance and simplicity of the concept. In a typical PL experiment for direct energy band gap semiconductors, a light-source that provides photons with an energy larger than the band gap energy is used to excite the material. Once the photons are absorbed, electrons and holes are formed with finite momenta k in the conduction and valence bands, respectively. The excitations then undergo energy and momentum relaxation toward the band gap minimum. Finally, the electrons recombine with holes which may or may not emit a photon. Many factors influence this process, therefore lead to a wealth of information about this material, including but not limited to band gap, scattering properties, recombination dynamics.

In the following sections, we utilize this powerful method to reveal the fascinating optical characteristics of InP nanoneedles grown on silicon, and further tailor them to facilitate excellent device performance.

3.2 Energy Band Gap

3.2.1 Crystal Phase of Nanoneedles

In this section, InP nanoneedles were grown on a surface-roughened silicon (111) substrate using low-temperature metalorganic chemical vapour deposition (MOCVD) in a catalyst-free environment. The nanoneedles were verified to be core-shell structures with dimensions that can be scaled up in direct proportion to the growth time [4]. A range of growth temperatures were explored (400-450°C), and samples grown at two temperatures were found to be of particular

interest (labeled "sample A" and "sample B" in what follows). Sample A, grown at 425°C, consists of very long needles with a taper angle of approximately 3°, as seen in Figure 3.1 (a). Sample B, grown at a higher temperature of 450°C, features shorter nanoneedles with a taper angle of about 8° (Figure 3.1 (b)). Both needle types have a clearly faceted hexagonal cross-section. It is worth noting that the base diameters of these nanoneedles are both around 0.8 µm, far beyond the lattice-mismatch critical dimension (around 40 nm) [38]. Longer growth time yielded nanoneedles with diameters above 1µm (up to 1.4 µm demonstrated), which are not shown here.

High-resolution transmission electron microscopy (HRTEM) was used to study the structural composition of the InP nanoneedles. With the use of focused ion beam (FIB) and micro-manipulator, we cut across the center of the nanoneedle and transferred the thin slice, or lamella, to a liftout grid. The lamella was then further thinned down to electron transparent thickness with Argon ion beam. HRTEM images and diffraction patterns were obtained from the thin lamella. More details on the method are described in [6]. Nanoneedles from sample A consist of a ZB/WZ-mixed polytypic crystal phase (referred as "mixed-phase nanoneedles"), as shown in Figure 3.1 (c). Nanoneedles from sample B are made up of essentially pure WZ crystal phase (referred as "WZ-phase nanoneedles"), with minimal stacking faults mostly confined to the root region and terminated at the sidewalls (Figure 3.1 (d)), benefitting from the core-shell growth mode. In Figure 3.1 (e), a bright field TEM image of the WZ-phase nanoneedle lamella is displayed, highlighting the major body area where the zoomed-in HRTEM image in Figure 3.1 (d) corresponds to.
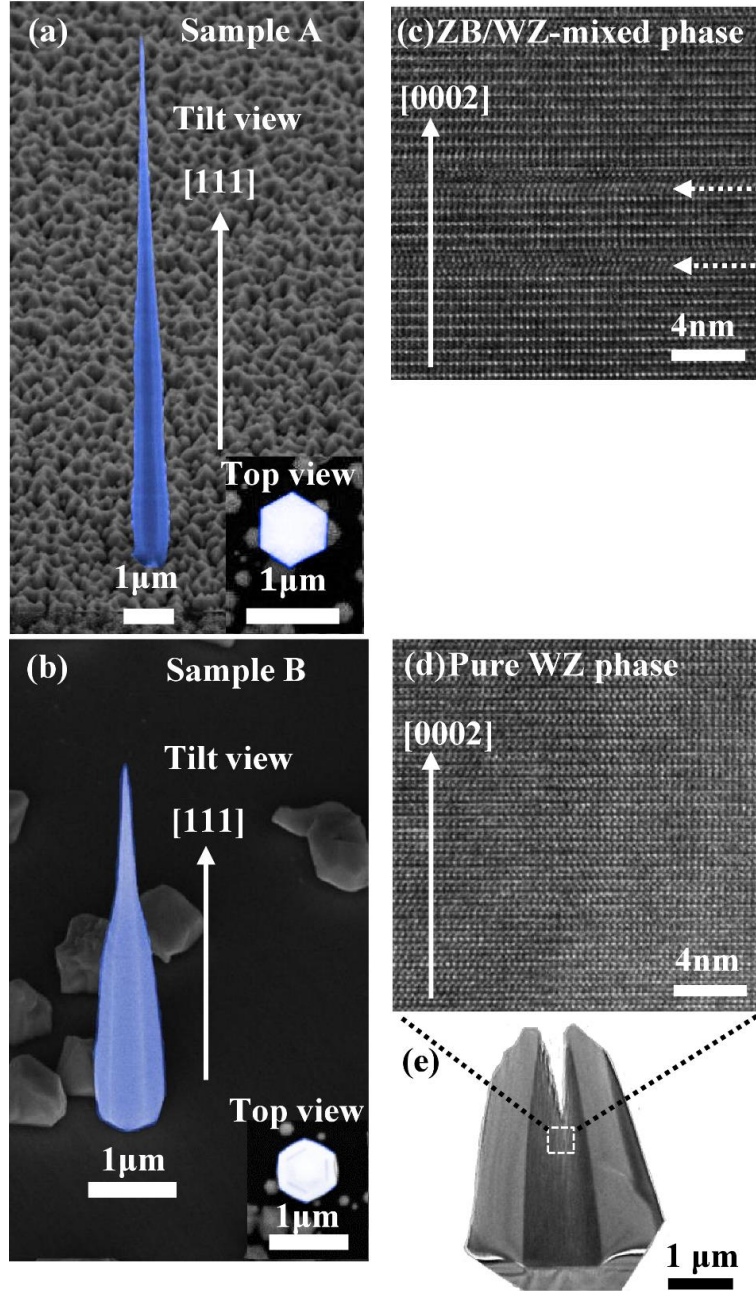
Figure 3.1 InP nanoneedle structure and phase composition. Sample A: ZB/WZ-mixed polytypic crystal phase. Sample B: pure WZ crystal phase. **(a)** 45° tilt view and top view (inset) of a typical mixed-phase nanoneedle from sample A, as seen by scanning electron microscopy (SEM). The images reveal a needle with a sharp tip (3° taper angle), hexagonal cross-section, diameter of 0.8 µm and a height of 15.2 µm. **(b)** 45° tilt view and top view (inset) SEM images of a typical WZ-phase nanoneedle from sample B. The images reveal a needle with a sharp tip (8° taper angle), hexagonal cross-section, diameter of 0.8 µm and height of 5.8 µm. **(c)** HRTEM image of a typical nanoneedle from sample A, exhibiting ZB/WZ-mixed polytypic crystal phase. Dashed arrows indicate two major stacking faults in this region, caused by ZB-phase mixed in WZ-phase. **(d)** HRTEM image of a typical nanoneedle from sample B, in pure single-crystal WZ phase. **(e)** Bright field TEM image of a thin lamella cut from the center of a WZ-phase nanoneedle with FIB. The dashed box highlights the area in the major body part from where the zoomed-in HRTEM image of (d) is taken. [7]

3.2.2 PL with CW Excitation

Micro-photoluminescence (μ-PL) measurements were done by delivering continuous-wave (CW) excitation from a diode laser to individual InP nanoneedles as-grown on a silicon substrate. Results shown here are all from typical nanoneedles that can represent the average performance of all nanoneedles on the same sample in terms of PL spectrum and intensity. For the typical mixed-phase nanoneedles from sample A, we observed a significant blue-shift in the PL spectrum with increasing pump power at 4K. As shown in Figure 3.2 (a), the PL emission peak shifts from 1.35 to 1.45 eV, at a rate of about 27.7 meV per ten times of pump power increase (per decade). In addition, a smaller portion of nanoneedles from sample A (Figure 3.2 (b)) exhibit a second emission peak around 1.41 eV, which matches the bandgap (E_g ~1.41-1.42 eV) of the ZB-phase InP (referred as "ZB-emission"). For WZ-phase nanoneedles (sample B), the PL spectrum consists of two peaks – a WZ-phase band-edge emission at 1.49 eV (referred as "WZ-emission") and an emission peak at 1.45 eV that saturates rapidly with increasing pump power (Figure 3.2 (c)). The fact that the peak at 1.45 eV was observed at nearly the same energy for thousands of nanoneedles tested suggests that the recombination involves bulk-related states, such as carbon-induced impurities [53] or radiative defects [64]. In contrast to mixed-phase nanoneedles, WZ-phase nanoneedles did not exhibit an observable blue-shift for either the 1.49 eV WZ-emission peak or the 1.45 eV emission peak (referred as "defect-emission").

Figure 3.2 (d) illustrates the band structure for ZB/WZ InP heterojunction at 0K, reconstructed from theoretical calculations [65]. A larger bandgap of 1.49 eV and a valence band offset of 0.11 eV are found in the pure WZ crystal phase of InP as compared to pure ZB-phase InP. The alternating of these two crystal phases within a given nanoneedle sample will generally introduce a type-II band alignment, whereby electrons are confined to ZB-phase segments and holes are confined to WZ-phase segments. The space charge due to carrier separation then induces an electric field across the heterojunction between the ZB and WZ segments, which brings about band bending at the interface, thus generating a triangular potential well with quantized energy levels [66]. Under a higher pump power, more carrier charges accumulate at the interface, thus enhancing the band-bending. The effective potential well width is then reduced so as to raise energy levels, causing a blue-shift in the PL emission as pump power increases. This blue-shift is usually regarded as experimental evidence for type-II band structure [67], [68]. As such, we conclude that the significant blue-shifts observed in the PL spectra of mixed-phase nanoneedles originate from the prevailing type-II band structure. The observation of ZB-emission from some of the nanoneedles on sample A (Figure 3.2 (b)) is likely due to the formation of more ZB phase induced by fluctuations in local growth conditions across the sample wafer [69]. We call such needles as "mostly-ZB-phase nanoneedles" in the following context.
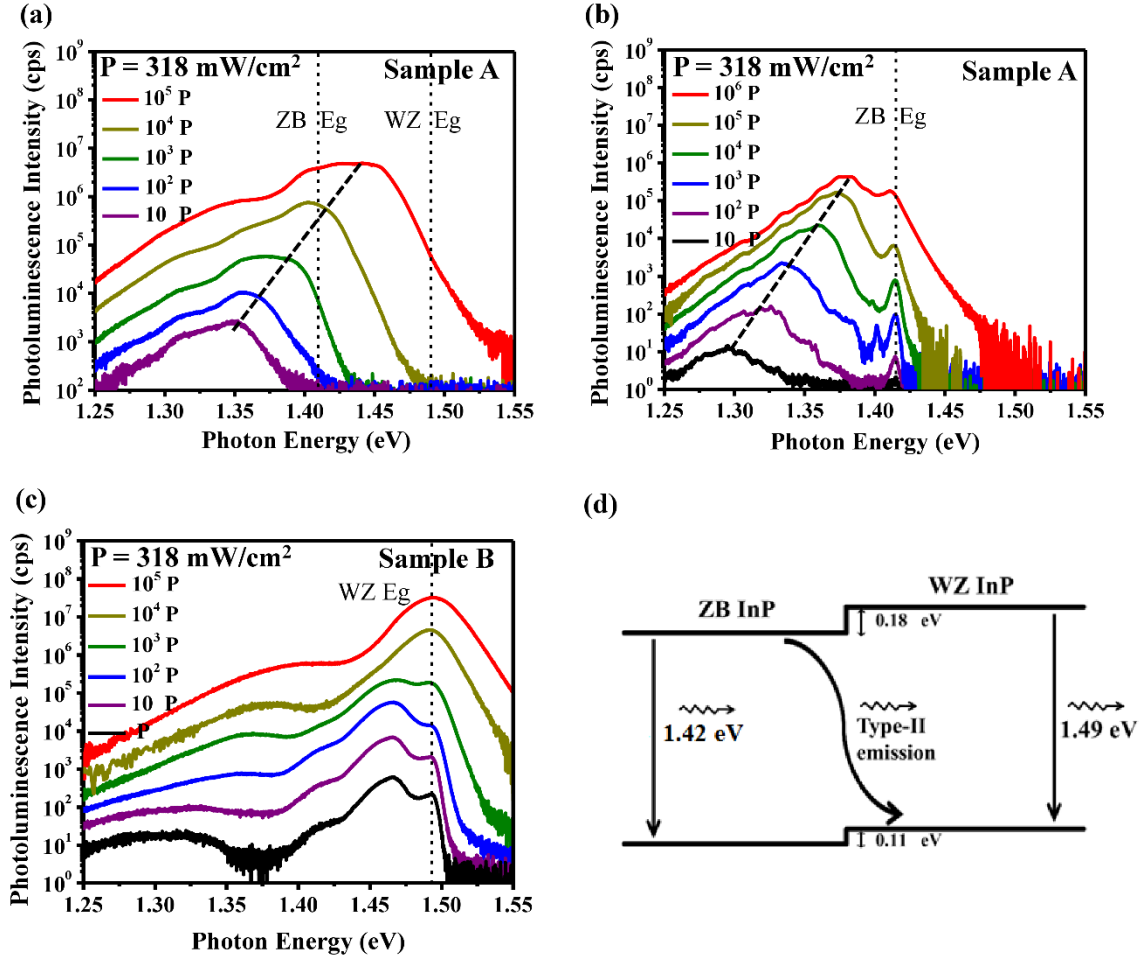
Figure 3.2 PL spectra at 4K under a range of laser pump powers (660-nm CW diode laser, power density from P to 10^5 P, with P=318 mW/cm^2). **(a)** A typical mixed-phase nanoneedle from sample A, displaying type-II emission with a significant blue-shift of 27.7 meV per decade, from 1.35 eV to 1.45 eV. **(b)** A mostly-ZB-phase nanoneedle from sample A that exhibits a ZB band-edge emission peak at 1.41 eV in addition to the type-II emission peak. **(c)** A typical WZ-phase nanoneedle, showing WZ band-edge emission at 1.49 eV and defect-emission at 1.45 eV. **(d)** Band structure of ZB/WZ InP heterojunction at 0K; WZ-phase InP has a larger bandgap and valence band offset of 0.11 eV compared with ZB-phase InP. The three carrier recombination paths (ZB band-edge, WZ band-edge, and type-II indirect recombination) are illustrated. [7]

3.2.3 Temperature-dependent PL

In order to further shed light on the origin of the PL for each type of nanoneedle, temperature-dependent CW-PL measurements were performed (Figures 3.3 (a-c)). The temperature evolution of the PL spectrum for the mostly-ZB-phase nanoneedle (Figure 3.2 (b)) is illustrated in Figure 3.3 (b). The type-II peak gradually saturates with increasing temperature until about 110 K, above which only the ZB-emission peak remains. The ZB-emission peak energy is shown as a function of measurement temperature (T) by the dark blue curve in Figure 3.3 (d), which can be fitted very well with the Varshni equation $E_g = 1.413-4.9\times10^{-4}T^2/(T+327)$, revealing a bandgap of 1.413 eV at 0K [70], [71]. For WZ-phase nanoneedles, the defect-emission peak saturates as

23

temperature rises, while WZ-emission preserves (Figure 3.3 (c)). The WZ-emission peak energy, shown as a function of temperature by the red curve in Figure 3.3 (d), can also be fitted well using a slightly modified Varshni equation: $E_g = 1.496-4.9\times10^{-4}T^2/(T+260)$, revealing a bandgap of 1.496 eV at 0K [70]- [72]. Intriguingly, a typical mixed-phase nanoneedle (Figure 3.2 (a) and 3.3 (a)) exhibits type-II emission all the way up to 298 K, with peak energy fluctuating (green curve in Figure 3.3 (d)). However, we no longer observe blue-shift behaviour with increasing pump power above 110 K, partly due to a broadened PL spectrum at higher temperature. Fig. 3e shows the normalised PL spectra for the three types of nanoneedles at room temperature. As far as we know, this is the first thorough analysis of the emission spectra of InP nanostructures as the crystal phase and temperature vary.
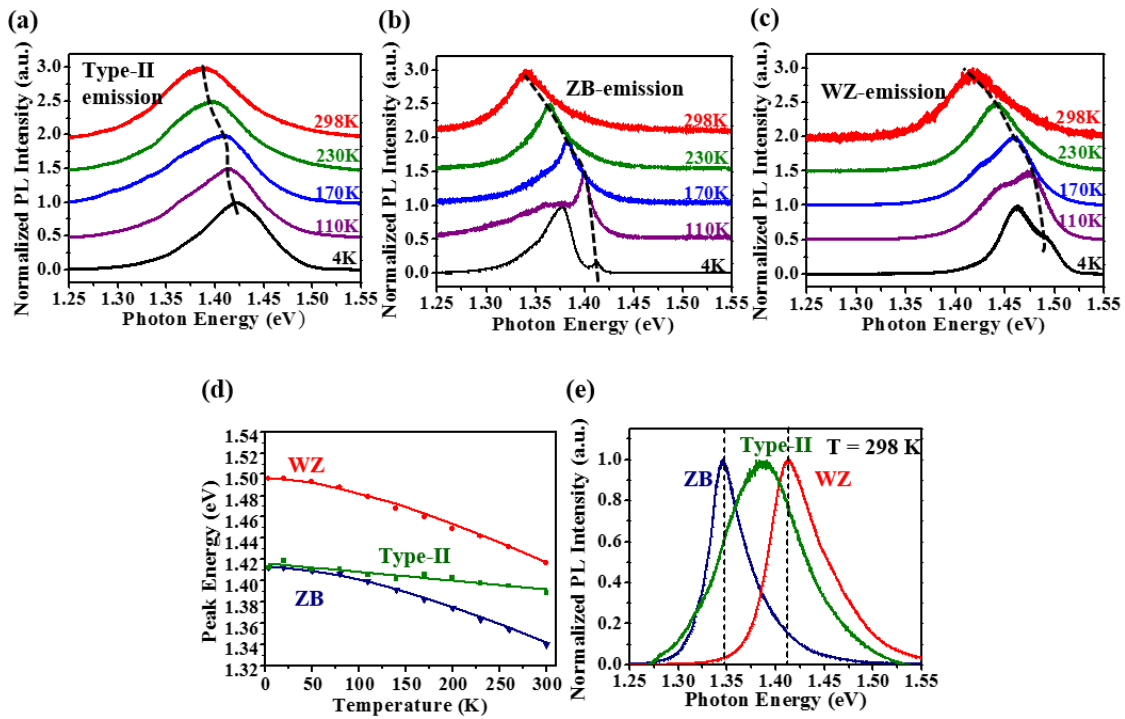
Figure 3.3 Temperature-dependent PL spectra of InP nanoneedles. Temperature ranges from 4 to 298K; the nanoneedles are pumped by 660-nm CW diode laser at an excitation power density of 2×10^4 P (P=318 mW/cm^2). **(a)** Typical mixed-phase nanoneedle. **(b)** Mostly-ZB-phase nanoneedle. **(c)** Typical WZ-phase nanoneedle. **(d)** PL emission peak energy as a function of temperature for the three needle categories in a-c. The dark blue curve corresponds to ZB-emission in (b), fitted with the Varshni equation (see text for details). The red curve corresponds to WZ-emission in (c), fitted with a modified Varshni equation (see text for details). The green curve corresponds to type-II emission in (a). **(e)** Room-temperature PL spectra for the three types of nanoneedles, showing emission peaks at 1.34 eV (dark blue, ZB-emission), 1.41 eV (red, WZ-emission) and 1.39 eV (green, type-II emission). [7]

3.3 Polarization-dependent Photoluminescence

Distinctive differences between the optical properties of the different InP crystal phases can also be seen by studying the polarization of the ZB-emission and WZ-emission (shown in Figure 3.4)

at 298 K. The as-grown nanoneedles were mechanically removed and placed horizontally onto a carrier substrate. Polarization measurement was performed by inserting a linear polarizer into the PL signal collection path and tuning the polarization angle with respect to nanoneedle as depicted in Figure 3.4 (a). Figure 3.4 (b) displays the PL spectra collected from the replaced nanoneedles, for one with ZB emission and one with WZ emission respectively. As seen in Figure 3.4 (c) [72], for ZB type crystal, recombination is between the s-like conduction band electrons which has Γ_6 symmetry and the p-like doubly-generate LH and HH bands with Γ_8 symmetry. The emitting light therefore should be completely unpolarized. A hexagonal WZ crystal, on the other hand, exhibits a completely different symmetry. The s-like conduction band has Γ_7 symmetry, while the p-like hole bands split into three separate hole bands due to a combination of the spin-orbit interaction and crystal field splitting. The lowest energy hole states (highest lying energy bands) having a symmetry of Γ_9 while the two higher energy hole bands (B and C bands) have Γ_7 symmetry. The recombination between Γ_7 and Γ_9 is dipole allowed only for E field perpendicular to the c axis of the nanowire and forbidden for E field parallel to the c axis. The measured PL data are plotted in polar coordinate in Figure 3.4 (d), the ZB-emission is strongly (74%) polarized parallel to the nanoneedle axis, due to the dielectric contrast between the higher-index nanoneedle bulk and the surrounding air. In contrast, the WZ-emission is strongly (78%) polarized perpendicular to the nanoneedle, because the hexagonal WZ-phase crystal undergoes valence band splitting as described above.

25
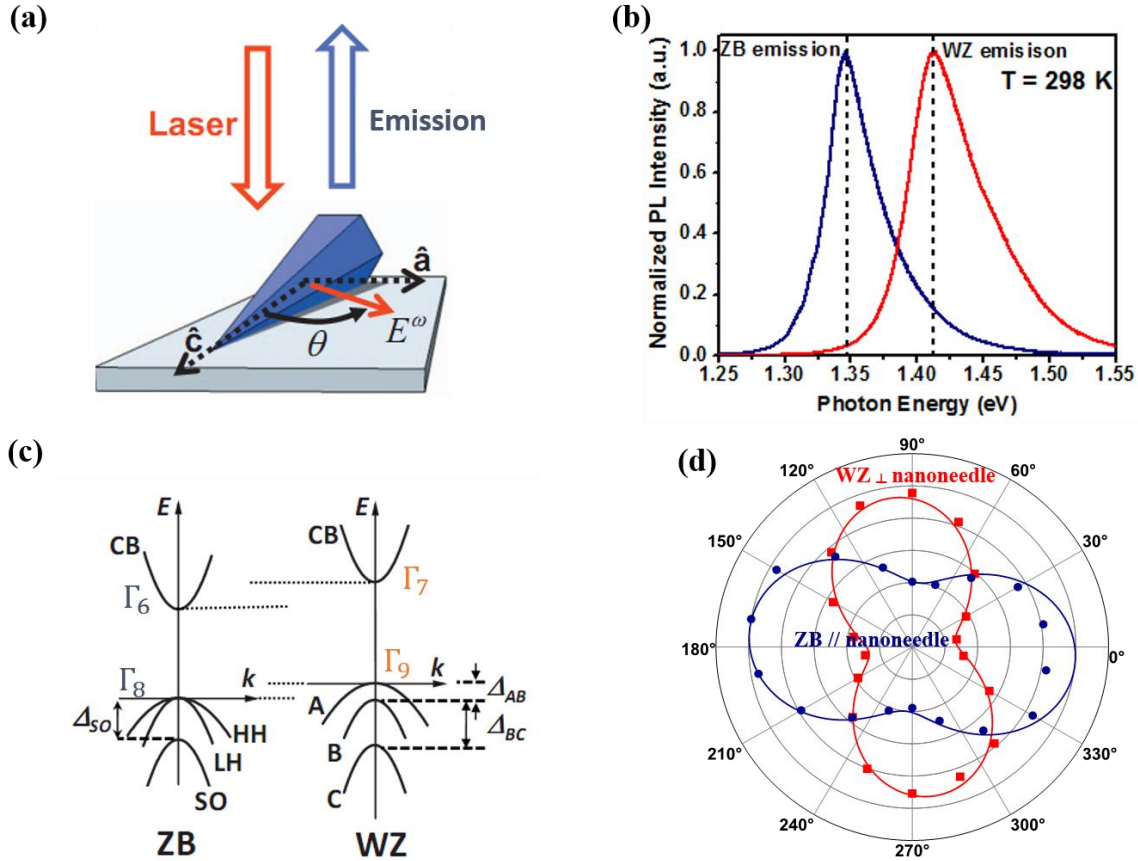
Figure 3.4 Polarization dependence of ZB and WZ emission. (a) Schematics showing the measurement configuration with nanoneedle mechanically removed from asgrown substrate and transferred onto another substrate, with figure adapted from [58]. **(b)** PL spectra collected from the transferred nanoneedle, with ZB phase and WZ phase respectively. **(c)** Band structure for ZB crystal and WZ crystal adapted from [72]. **(d)** Polarization dependence of the integrated PL intensity for ZB-emission (dark blue) and WZ-emission (red), with the solid line indicating a fit to $\sin^2\theta$. The radial scale lines represent normalized PL intensity, while the tangential scale lines represent polarization angle with respect to the nanoneedle axis. This figure is adapted from [7].

3.4 Time-resolved Photoluminescence

Charge carrier dynamics in semiconductors directly reflect the nature and quality of materials. This makes it essential to characterize the material system with precise and efficient measurement techniques. The carrier recombination lifetime is highly dependent on the nature and dimension of the materials and interfaces. Surface effects, passivation as well as the presence of impurities and defects can introduce significant variations in this parameter. Since photoluminescence is a direct monitor of the interaction between light (photon) and matter (carrier), the general methodology to probe the carrier recombination dynamics is to conduct PL in time domain in addition to spectral domain [73].

Time-resolved photoluminescence (TRPL) via time-correlated single photon counting (TCSPC) is particularly suited for fast charge carrier dynamics in the nanosecond regime for common III-V compound semiconductors. Time correlated single photon counting (TCSPC) was used to probe the carrier decay rate through the PL emission, by incorporating an avalanche photodiode (APD) into the μ-PL setup as shown in Figure 3.5. Through calibration with the titanium – sapphire femtosecond laser source, the impulse response of the TRPL setup was derived and found to offer a timing resolution of about 40 ps, with a decay tail of approximately 300 ps due to carrier transition delay inside the APD. When the carrier decay lifetime exceeds one time period of the pulsed laser source (12.5 ns), an electro-optic-modulator based pulse picker was used to reduce the repetition frequency from 80 MHz to 8 MHz, enabling long decay time to be measured more accurately. The laser pulses are then delivered to a beam splitter where one trace of the beam activates the TCSPC start signal through a photodetector. The other trace of the beam continues to illuminate the sample via a high-NA objective. The PL collected from the sample then activates a stop signal for the TCSPC electronics through the APD. The time interval between the start and stop signal is then measured many times to account for the statistical nature of photoluminescence emission. The delay times are sorted into a histogram that plots the occurrence of emission over time after the excitation pulse. Carrier recombination lifetime is then obtained by fitting of this histogram with an exponential decay function.

26
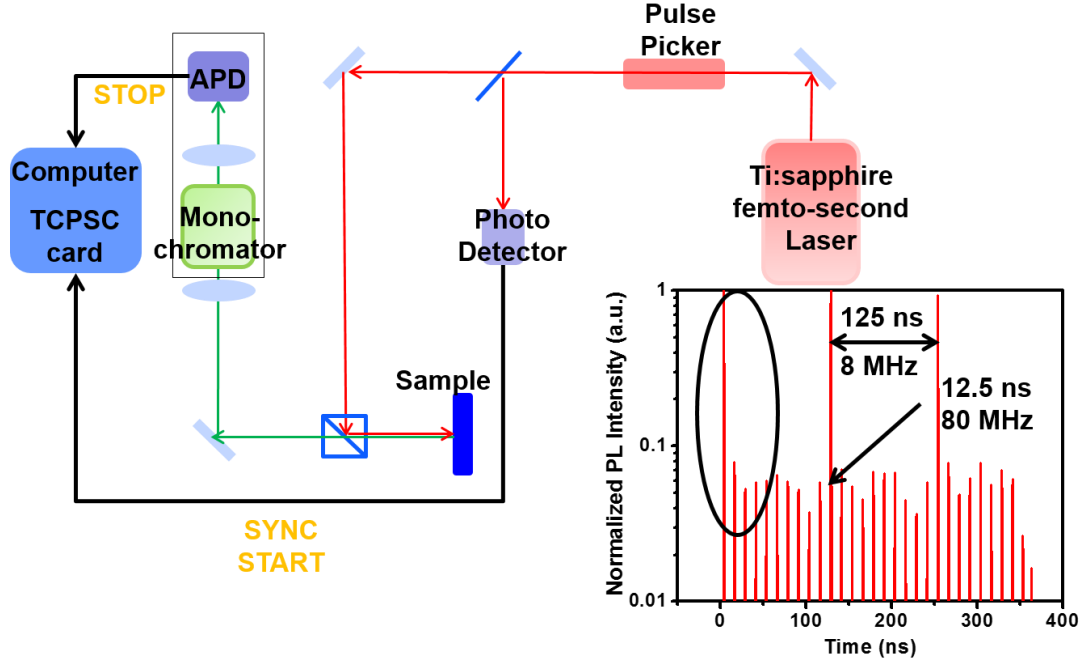
Figure 3.5 Optical setup for time-resolved photoluminescence (TRPL) measurement with time-correlated single-photon counting (TCSPC) method. The inset figure shows that laser pulses are selected by a pulse picker to reduce repetition frequency from 80 MHz to 8 MHz to accommodate samples with longer carrier recombination lifetime.

Figure 3.6 displays TRPL decay traces under varying pump powers for mixed-phase nanoneedle (Fig. 3.6 (a)) and WZ-phase nanoneedle (Figure 3.6 (b)), fitted with exponential decay functions. For mixed-phase nanoneedle, the temporal behavior of the type-II emission peak was studied. Under a very low pump power density of about 9.7 Wcm^{-2} (defined as P' here), the fitted decay curve yields an extremely long carrier lifetime of 13.5 ns. This can be attributed to the type-II band structure, which induces spatial separation of electrons and holes [74] [75]. The carrier lifetime falls as the pump power increases, as can be seen by the purple, blue, green and yellow lines in Figure 3.6 (a).

The detection wavelength for WZ-phase nanoneedle was varied with increasing pump power from the defect-emission peak at 1.45 eV (Figure 3.6 (b)) to the WZ-emission peak at 1.49 eV (Figure 3.6 (c)). Under the same low pump power of P', the defect-emission peak exhibits a long lifetime of 10.5 ns. When pumped at 20P' and 50P', the WZ-emission peak at 1.49 eV emerges and becomes dominant while the defect-emission peak saturates. This leads to carrier lifetimes of around 6 ns for saturated defect-emission, and bi-exponential behaviour caused by an overlap with the WZ-emission peak. This confirms that the defect-emission at 1.45 eV, which is the result of impurities or radiative defects, is not sufficiently dominant to confine a large proportion of carriers. Probing at 1.49 eV, the carrier lifetime remains at around 300 ps (Figure 3.6 (c)) even though the power density increases from 40P' (purple) to 600P' (yellow); this is as a result of the fact that the resolution limit of the timing system has almost been reached.

27

We note that the TRPL decay curves for both mixed-phase and WZ-phase nanoneedles are single exponential, indicating a lack of non-radiative recombination and dominance of radiative recombination even at very high pump powers [76], [77]. The ability to scale up the size of the nanoneedles is beneficial for nanostructure-based optoelectronic devices, as it essentially reduces the surface recombination probability. Meanwhile, the absence of a fast non-radiative recombination portion in the decay curves indicates the superior surface quality of the InP nanoneedles [78].

The carrier lifetimes of mixed-phase nanoneedles and WZ-phase nanoneedles are further compared in Figure 3.6 (d). At 10P', the carrier recombination speed of pure WZ-phase nanoneedles is around 30 times faster than that of mixed-phase nanoneedles. This indicates that the band-edge recombination of WZ-phase nanostructures offers much higher emission efficiency than the indirect type-II recombination of mixed-phase nanostructures.
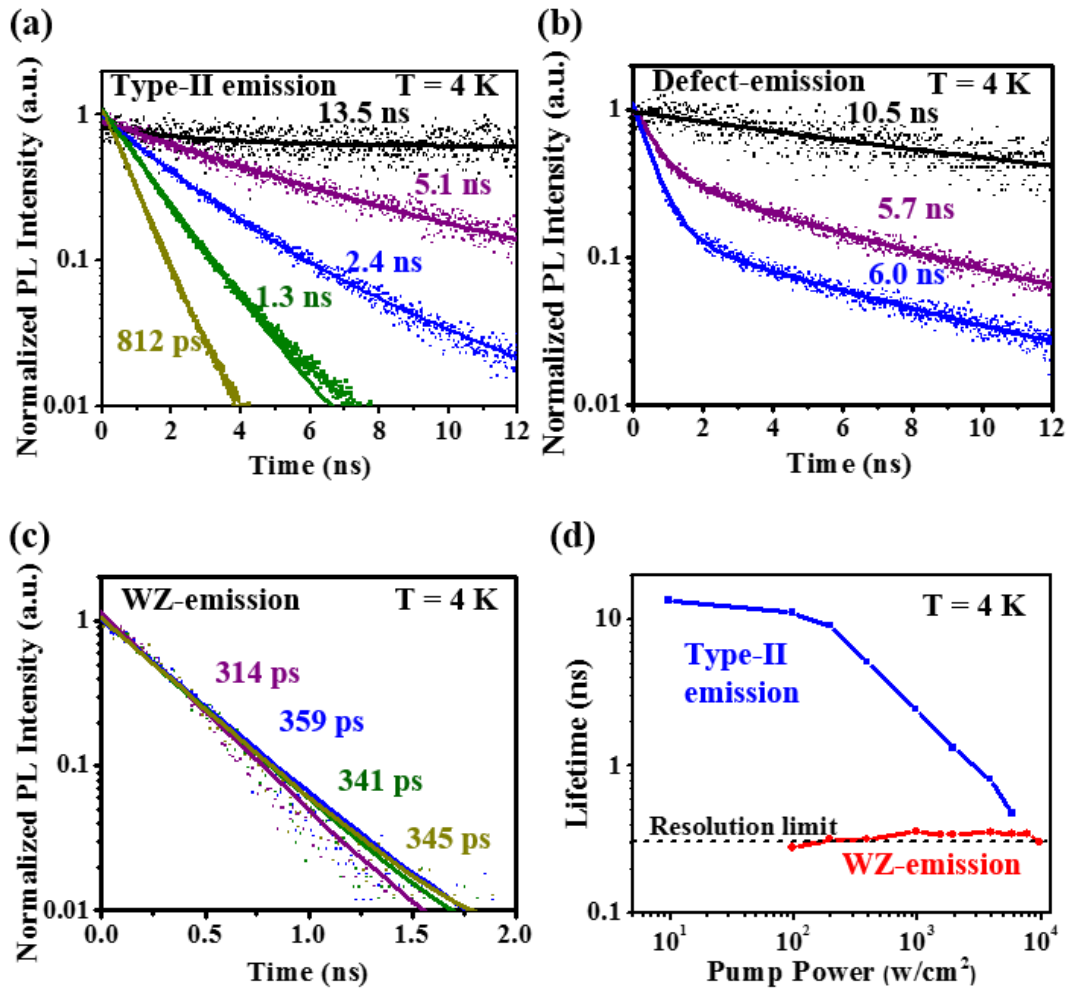
Figure 3.6 Carrier recombination dynamics. TRPL data (dots) measured using the TCSPC method, pumped by a titanium:sapphire fs laser at 750 nm. The data are fitted with an exponential decay function (solid curves). **(a)** Type-II emission from typical mixed-phase nanoneedles with increasing pump power. Carrier lifetime is 13.5 ns at P' = 9.7 Wcm^{-2} (black), 5.1 ns at 40P' (purple), 2.4 ns at 100P' (blue), 1.3 ns at

28

200P' (green) and 812 ps at 400P' (yellow). **(b)** Defect-emission (1.45 eV) obtained with WZ-phase nanoneedle with increasing pump power. Carrier lifetime is 10.5 ns at P' = 9.7 Wcm^{-2} (black), 5.7 ns at 20P' (purple) and 6.0 ns at 100P' (blue). **(c)** WZ-emission (1.49 eV) from WZ-phase nanoneedle with increasing pump power. Carrier lifetime is 314 ps at 40P' (purple), 359 ps at 100P' (blue), 341 ps at 200P' (green) and 345 ps at 600P'(yellow). **(d)** Comparison of the carrier recombination lifetimes of mixed-phase nanoneedle and WZ-phase nanoneedle for varying pump powers. [7]

3.5 Internal Quantum Efficiency

The IQE of a system is intimately linked to the carrier recombination lifetime, and is an important figure of merit for optoelectronic devices such as photovoltaic cells. This difference between WZ and mixed-phase nanoneedles is further underscored when IQE values are obtained through directly comparing the PL intensities pumped by a pulsed laser at different temperatures [79]. Assuming a 100% IQE at 4K for all nanoneedles pumped to saturated PL intensities, 10% IQE at room temperature (298 K) can be obtained for mixed-phase nanoneedles, while typical WZ-phase nanoneedles offer a more-than-doubled efficiency of around 25% (Figure 3.7 (a)). A detailed PL intensity comparison is shown in Figure 3.7 (b) under varying CW-laser pump powers at both 4K and 298K. Notably, WZ-phase nanoneedles typically yield a PL intensity more than three orders of magnitude larger than that of mixed-phase nanoneedles. With respect to photovoltaic applications, III-V nanostructures offer more efficient light absorption and significant cost reduction, especially when they are grown on silicon substrate [80]. However, nanostructures are known to suffer from undesired non-radiative surface recombinations brought about by a large surface-to-volume ratio. These non-radiative losses can significantly reduce the IQE, resulting in a decrease in the open-circuit voltage (VOC) [81], [82]. Given their ability to be scaled up to diameters far above the critical dimension, the InP nanoneedles reported here offer an outstanding IQE while still conferring the other advantages of nanostructure photovoltaics. Furthermore, a larger bandgap can also increase Voc [81], which makes single-crystal WZ-phase InP nanoneedles on silicon stand out as a promising candidate for high-efficiency low-cost photovoltaics.
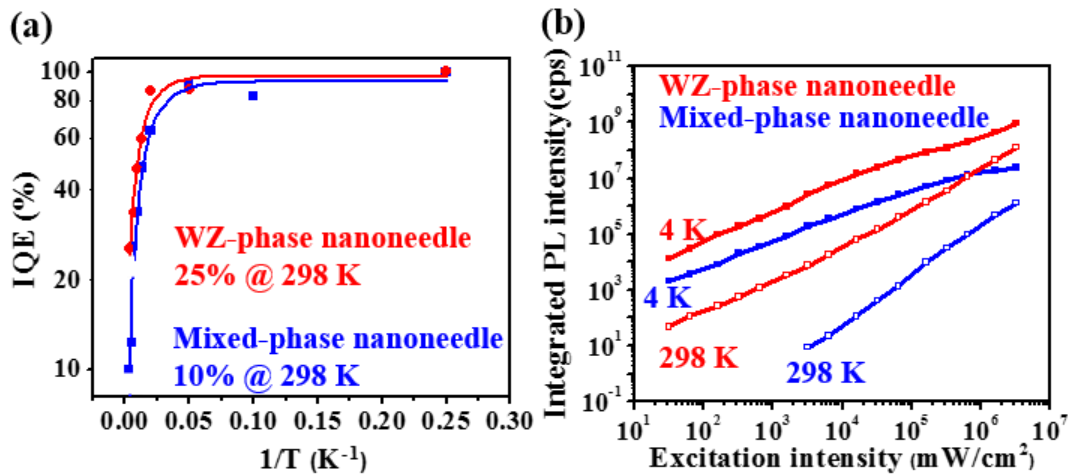
Figure 3.7 Internal quantum efficiency. (a) IQE data (dots) extracted from power-dependent PL measurements at different temperatures, fitted with Arrhenius equation (curves). Blue plot: mixed-phase nanoneedle, where IQE is 10% at 298K. Red plot: WZ-phase nanoneedle, where IQE is 25% at 298K. **(b)** Comparison of the integrated PL intensities at different pump powers for typical mixed-phase nanoneedle (blue) and WZ-phase nanoneedle (red), at 4K (solid dots) and 298K (empty dots). The emission from mixed-phase nanoneedles at room temperature is too weak to be collected below $1x10^3$ mW/cm^2 power density (shown by the blue curve with empty dots). [7]

3.6 Nanolasers Integrated on Silicon

3.6.1 Laser Characterization

Each as-grown nanoneedle provides a natural optical cavity, supporting unique helically-propagating resonance modes [1], [83]. The large size of the nanoneedle ensures that modes are well confined inside the cavity, leading to very effective gain-mode overlap. Combined together, this enables optically-pumped lasing of single nanoneedle as-grown on silicon. Figure 3.8 (a) demonstrates lasing (at 4 K) at different photon energies for the nanoneedles shown in Figures 3.2 (a)-(c), respectively. The close gain-mode matching suggests the potential to tune the lasing wavelength by tailoring the crystal phase, and is an area worthy of future exploration. Upon lasing, nanoneedles demonstrate an ultrafast carrier lifetime of around 50 ps (red plot, Figure 3.8 (b)) [84]. The bi-exponential appearance is due to the fact that the resolution limit of the TRPL timing system, whose impulse response is shown by the blue curve, has been reached.

Room-temperature laser oscillation is demonstrated with InP nanostructures on silicon for the first time, to the best of our knowledge, by optically pumping an upright mixed-phase nanoneedle from the top. The typical spectrum of a room-temperature nanoneedle laser is shown in Figure 3.8 (c). A gain model was established, followed by rate equation analysis, in order to fit the corresponding light-light (L-L) curve [1]. The fitted L-L curve in Figure 3.8 (d) reveals an estimated cavity quality factor (Q) of 308, and a spontaneous emission coupling factor (β) of approximately $5x10^{-4}$. Details about the fitting method are in the following sections. When the pump power is below lasing threshold, only a small spot of spontaneous emission could be observed on the camera image. Upon lasing, strong speckle patterns appear (see inset in Figure 3.8 (d)), which is usually regarded as a classic signature of lasing oscillation. The fact that mixed-phase nanoneedles rather than pure WZ-phase nanoneedles are able to lase at room temperature is somewhat counter-intuitive. We attribute this to the influence of the taper angle of the nanoneedle sidewalls on the optical cavity's quality [1], [83]. Sidewall taper is the primary loss mechanism for our as-grown cavities; the smaller taper angle of mixed-phase nanoneedles results in less light leakage through the cavity sidewalls and therefore a better optical cavity. Engineering the taper angle thus offers an avenue to improve future laser performance. Simulation results about how to optimize laser cavity will be discussed in section 3.6.3.
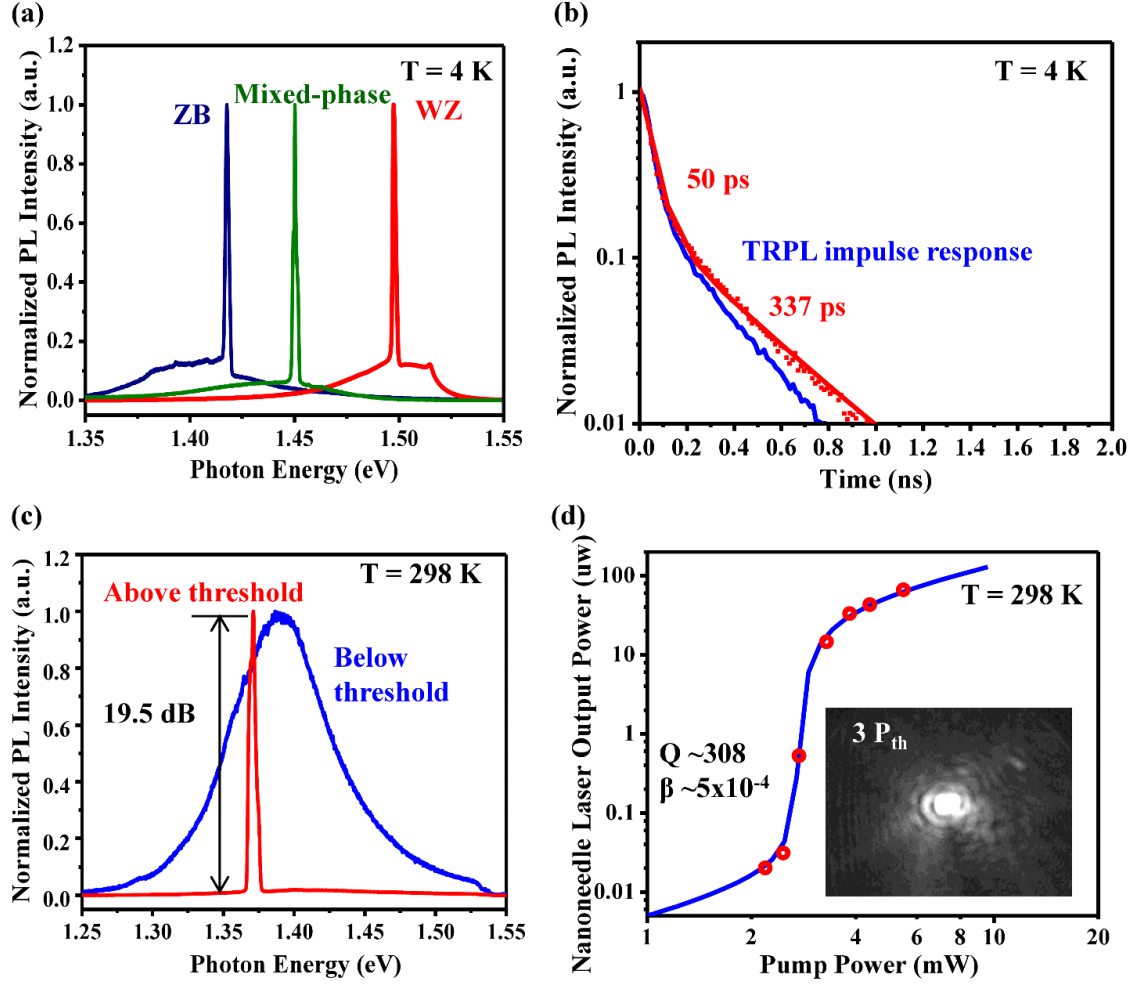
Figure 3.8 InP nanoneedle lasing. Nanoneedles optically-pumped by a titanium:sapphire fs laser at 750 nm. **(a)** Lasing spectra observed at different photon energies for typical WZ-phase nanoneedles (red), typical mixed-phase naoneedles (green), and mostly-ZB-phase nanoneedles (blue). All PL intensities are normalized for visibility. **(b)** TRPL decay curves for WZ-phase nanoneedles after lasing (red line). The lifetime falls to approximately 50 ps, and tail is due to bi-exponential system impulse response (blue curve, resolution limit 40 ps with 300 ps tail). **(c)** Typical lasing spectrum of a room-temperature laser, achieved by optically pumping an upright mixed-phase nanoneedle from the top plane. Spectra below (blue) and above (red) lasing threshold are normalized for visibility. A high suppression ratio of 19.5 dB and full width at half maximum of 5.5 meV (3.6 nm) is obtained after lasing. **(d)** Corresponding L-L curve for the nanoneedle laser in **c**. Analysis reveals a Q of 308 and β of 5x10^{-4}. Both pump power and nanoneedle laser emission are converted into average powers. Inset shows the speckle patterns above the lasing threshold (P_{th}) of 2.7 mW, and signifies lasing oscillation. [7]

3.6.2 Laser Modeling

After obtaining experimental data, it is critical to analyze these data and extract useful information. This section starts with gain analysis, followed by rate equation analysis, to probe how gain interacts with cavity. Finally, we will be able to obtain important parameters

determining how our nanolasers perform. Details about the laser modeling methodology used here can be found in the supplementary information of [1].

When conducting fitting for the laser L-L curve, a gain model needs to be constructed firstly. Starting from Fermi's golden rule to model photon generation by electron-hole recombination, a material gain spectrum can be derived as

$$g(\hbar\omega) = \frac{\pi e^2}{n_r c \varepsilon_0 m_0^2 \omega} |M|^2 \int_0^\infty \rho_r (f_c - f_v) dE \quad (3.1)$$

where n_r is material refractive index, c is speed of light, ε is vacuum permittivity, m_0 is electron mass, and ω is the radial frequency of the electronic transition. M is calculated from the momentum matrix element and describes the strength of the transition. f_c and f_v are Fermi functions representing the distribution of electrons and holes, respectively. ρ_r is the reduced density of electronic states in a material. Please note that quantization effects are not seen here, due to the size of nanoneedle being beyond the de Broglie wavelength of electrons and holes. Thus, we use density of states for 3-dimensional bulk material as below,

$$\rho_r = \frac{1}{2\pi^2} \left(\frac{2m_r}{\hbar^2} \right)^{\frac{3}{2}} \sqrt{\hbar\omega - E_g} \quad (3.2)$$

where E_g, $\hbar$, m_r are the energy band gap, reduced Planck constant, and reduced effective mass, respectively.

In real experiments, intraband scattering effects need to be included as well, by convolving the gain spectrum in 3.1 with a Lorentzian lineshape function characterized by τ_{in} – the intraband scattering carrier lifetime. We fit the width of PL spectrum to obtain τ_{in} thus to estimate the broadening of gain spectrum. The analytical spontaneous emission spectrum used for fitting is generated by the gain spectrum in Equation (3.1) convolved with Lorentzian lineshape and following Einstein's AB coefficient treatment:

$$r_{sp}(\hbar\omega) = \frac{2n_r e^2 \omega}{hc^3 \varepsilon_0 m_0^2} |M|^2 \int_0^\infty \rho_r f_c (1 - f_v) \frac{\hbar/\pi\tau_{in}}{\left(E_g + E - \hbar\omega \right)^2 + (\hbar/\tau_{in})^2} dE \quad (3.3)$$

The fitting of a typical PL spectrum representing spontaneous emission from sample A (mixed-phase nanoneedle) is demonstrated in Figure 3.9, with which we obtained $\tau_{in} \sim 30$ fs.
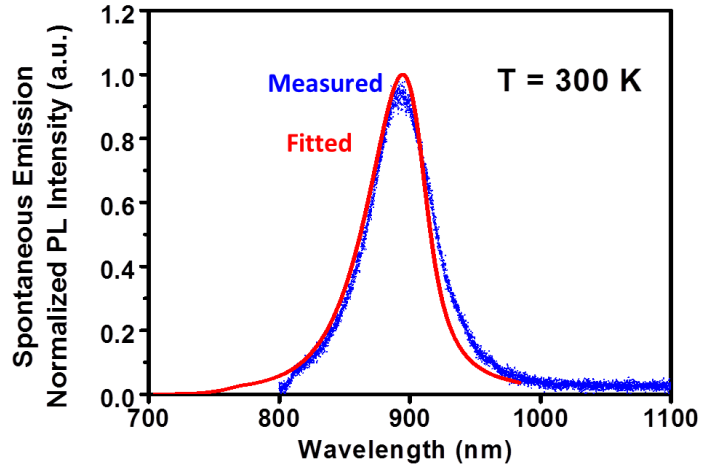
Figure 3.9 Fitting of spontaneous emission spectrum. The experimental PL spectrum at room temperature from a typical mixed-phase nanoneedle of Sample-A (blue) is fitted (red) with the spontaneous emission spectrum in expression (3.3). The fitted value for intraband scattering carrier lifetime is ~30 fs.

By plugging this τ_{in} value back into the gain equation (3.1 convolved with Lorentzian lineshape), we can generate a series of gain spectra under different carrier concentration N. Obtaining the peak gain value under each carrier concentration level, we can plot maximum gain versus carrier concentration, as shown by Figure 3.10 blue curve. We then use a logarithmic gain model to fit the curve,

$$g(N) = g_0 \ln(\frac{N+N_s}{N_{tr}+N_s}) \qquad (3.4)$$
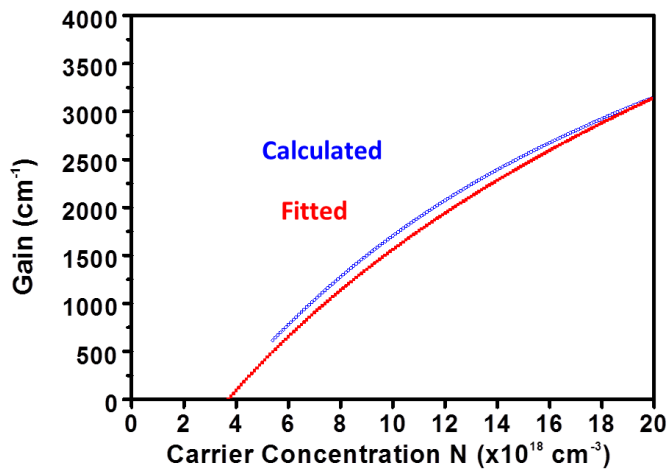
Figure 3.10 Gain model. Peak gain versus carrier concentration calculated from gain spectrum equation (blue) is fitted with logarithmic material gain model (red). The fitting parameters used here are $g_0 = 3500\ cm^{-1}$, $N_{tr} = 3.2\times10^{18} cm^{-3}$, and $N_s = 8\times10^{18} cm^{-3}$.

With this way to obtain gain value at each carrier concentration level, we are now able to fit the laser L-L curve by performing rate equation analysis. Then quality factor Q and spontaneous emission coupling factor β can be extracted from the fitting. The modified rate equation to suit optical pumping rather than electrical pumping is as follows，

$$\frac{dN}{dt} = \frac{\eta_a P}{h\nu V} - (AN + BN^2 + CN^3) - v_g gS \qquad (3.5)$$

$$\frac{dS}{dt} = \Gamma\beta(BN^2) + \Gamma v_g gS - \frac{S}{\tau_p} \qquad (3.6)$$

where N and S are carrier concentration and photon density in the cavity, respectively. P is the average power of the pump laser (converted from peak power of a pulsed laser), η_a is the injection quantum efficiency, A, B, C are the carrier recombination coefficients, v_g is group velocity, Γ is confinement factor, τ_p is photon lifetime.

Numerically solving differential equations (3.5) and (3.6) for the transient behavior of the carrier and photon densities, we can construct L-L curve to fit the experimental data. We treat spontaneous emission coupling factor β and threshold gain g_{th} as fitting parameters, the result is as shown in Figure 3.8 (d). Then Q factor can be calculated as

$$Q = \frac{2\pi n_g}{\lambda \Gamma g_{th}} \qquad (3.7)$$

In fitting L-L curve, we found that Q mainly determines the threshold pump level, while β is responsible for how high the "knee" is in the curve. In Figure 3.8 (d), we obtained a Q factor of ~308, and β~5×10^{-4}. As can be seen from the result, our current Q factor is relatively modest, the next section will discuss how to optimize the laser cavity. The parameters used for fitting in this section are listed in the Table 3.1.

m_e^*	0.077 m_0 kg
m_{hh}^*	0.6 m_0 kg
m_{lh}^* ($m_r = \left(\frac{1}{m_e} + \frac{1}{m_h}\right)^{-1}$)	0.12 m_0 kg
E_p ($|M|^2 = \frac{m_0 E_p}{6}$)	20.7 eV
E_g	1.306 eV
τ_{in}	30 fs
n_r	3.075
N_{tr}	3.2×10^{18} cm^{-3}
N_s	8×10^{18} cm^{-3}
g_0	3500 cm^{-1}
A	0
B	$5\times10^{-10} cm^3/sec$
C	0
n_g	4.2
Γ	1

Table 3.1 Parameters used for gain modeling and rate equation analysis.

3.6.3 Laser Cavity Optimization

Despite the reversed index contrast between InP nanoneedle (n~3.4) and silicon substrate (n~3.6), sufficient optical feedback or Q factor is still attained for laser oscillation in nanoneedle structure. Even non-negligible absorption by silicon at the nanolaser wavelength can be overcome. This seemingly counter-intuitive phenomenon encourages us to unveil the physical insight of mode propagation inside nano-cavity. As the study reveals, modes inside nanoneedle/nanopillar adopt a helically propagating fashion instead of the conventional Fabry-Perot resonance. While theoretical and experimental explanations can be found in ref. [83], intuitively speaking, helically-propagating modes can have nearly total internal reflection at the nanoneedle-silicon interface because their wavevectors strike that boundary with grazing incidence at extremely shallow angles. On the other hand, the helical propagation modes are very sensitive to the cavity shape and geometry, which makes it critical to engineer and optimize the cavity. Some preliminary results analyzing a few aspects that influence laser cavity are introduced here.

During laser characterization of both sample A and B in Figure 3.1, it is found that nanoneedles from sample A tend to have much lower lasing threshold than those from sample B. It is a little counter-intuitive because sample B possesses a much better material quality compared with sample A. Thus more thoughts need to be put into another key determiner of laser – the optical cavity. The biggest difference we observed from sample A and B is the taper angle of the nanoneedle top, with nanoneedle from sample A having ~3° while that from sample B showing ~8°. We thus simulated the field profile and Q factor for nanopillar cavities with different sidewall taper angles, as shown in Figure 3.11. Lumerical's finite-difference time-domain (FDTD) simulation was performed in 3D space. The results are enough to convince us that even a little sidewall tapering will result in increased light leakage thus reduced cavity Q factor. This can explain the contrast between nanolasers on sample A and B to some degree.
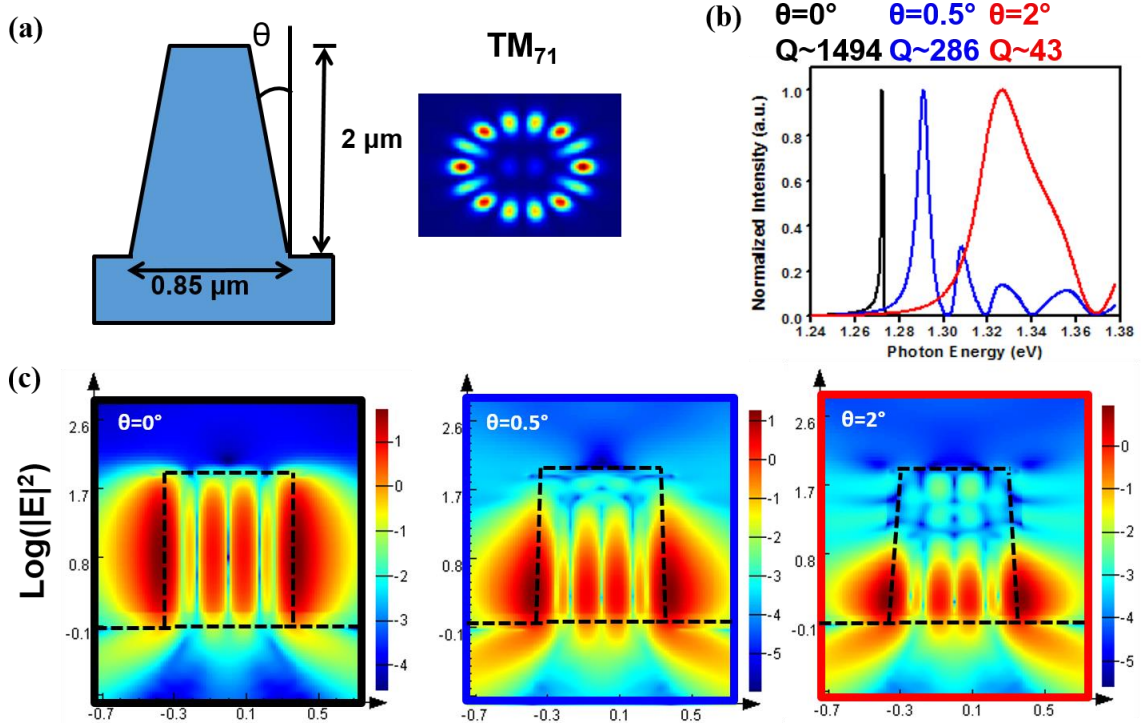
Figure 3.11 Effect of nanopillar sidewall taper on optical modes simulated with 3D FDTD. (a) Geometric parameters and helical mode used in this simulation. **(b)** Simulated optical resonance spectra for nanopillars with taper angle of 0°, 0.5°, and 2° respectively. A decrease of Q factor is observed with increased taper angle. **(c)** Vertical field profile for the nanopillars with taper angle of 0°, 0.5°, and 2° corresponding to (b). Light leakage is seen for increased taper angle.

In addition, we notice that sample A has a continuous wetting layer surrounding nanoneedles while sample B possesses none or only some clusters. This results from the growth condition variation [57]. However, the wetting layer causes inverse tapering at the nanoneedle root because it follows a core-shell growth fashion. This is similar with what happened to the growth of InGaAs/GaAs nanopillars on silicon, and full explanations can be found in ref [6]. While without the continuous wetting layer, the root of InP nanoneedle is in direct contact with the substrate without any inverse tapering, like what was validated in Figure 2.8. This leads us to investigating the influence of inverse tapering on optical cavity. In Figure 3.12, an inverse taper angle of 30° is introduced in the root part, while top tapering is kept at 2°. With FDTD simulation, we found that cavity without inverse tapering (length of the tapered bottom L=0) only has a Q factor of ~43, while by introducing a 100-nm inverse-tapered bottom Q increases to ~296. Intuitively, inverse tapering brings in a high index-contrast InP/air interface at the bottom of nanoneedle which enhances the optical feedback. This further explains why nanoneedles on sample A with wetting layer are easier to lase than those on sample B whose roots sit entirely on silicon substrate.
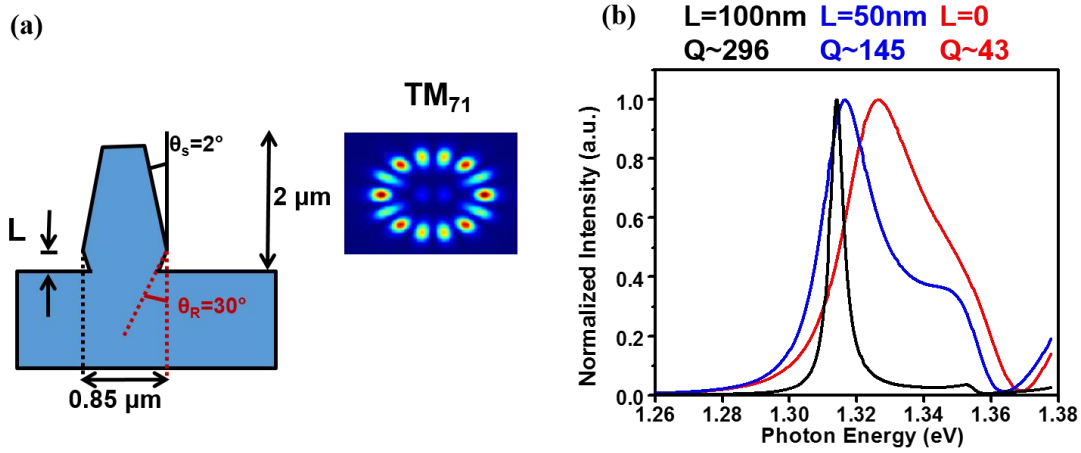
Figure 3.12 Effect of nanopillar bottom inverse taper on optical modes simulated with 3D FDTD. (a) Geometric parameters and helical mode used in this simulation. **(b)** Simulated optical resonance spectra for nanopillars with the length of bottom inverse-tapered part of 0, 50, and 100 nm, respectively. An increase of Q factor is observed with increased taper length.

Based on the simulation results above, we attempted geometry optimization during the growth process. Instead of a continuous growth, we performed a secondary growth (i.e. regrowth) by masking the bottom portion of an already grown nanopillar with thin layers of silicon dioxide (SiO$_2$) and amorphous silicon prior to regrowth. The final geometry is shown in the schematics of Figure 3.13 (a). From the optical spectra in Figure 3.13 (b), we can see this regrown structure has the Q factor enhanced almost by 8 times, with a much narrower spectrum linewidth. Figure 3.13 (c) and (d) compare the vertical field profiles for the original as-grown structure and the regrown structure, respectively. It clearly demonstrates the influence of regrowth on optical cavity, in the following aspects: (1) it reduces top tapering thus cavity loss; (2) it adds a "kink" which works similar with bottom tapering, introducing optical feedback to the helical modes; (3) it confines the optical modes mostly in the upper body part, away from the defect-rich root part. In addition to optimizing the optical cavity, this regrowth process also brings in a few other winning advantages for making an optoelectronic device, which include eliminating the shunt path between the n-type shell (of the p-i-n junction inside the nanopillar) and p-type silicon substrate. More details can be found in ref [50].
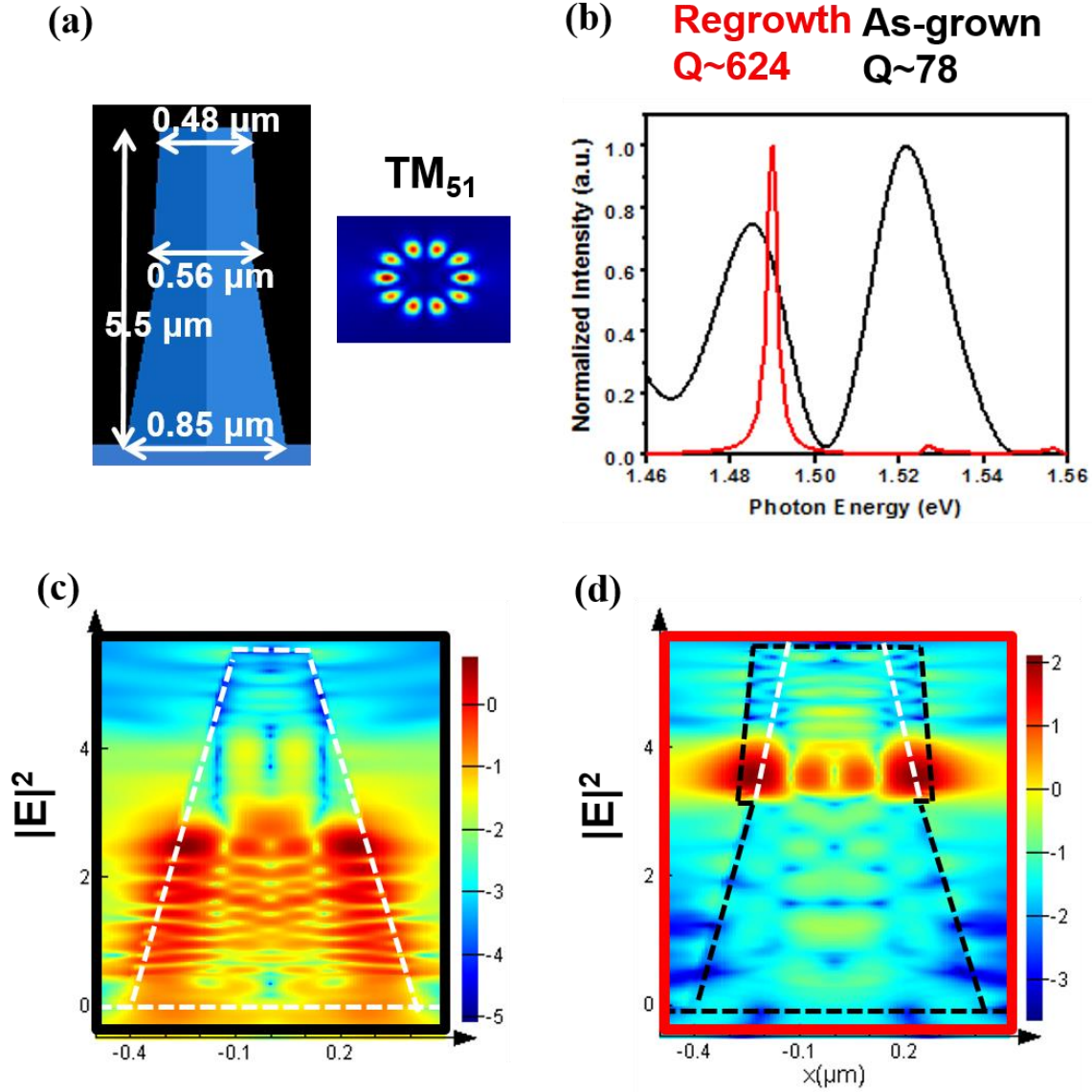
Figure 3.13 Internal quantum efficiency. (a) IQE data (dots) extracted from power-dependent PL measurements at different temperatures, fitted with Arrhenius equation (curves). Blue plot: mixed-phase nanoneedle, where IQE is 10% at 298K. Red plot: WZ-phase nanoneedle, where IQE is 25% at 298K. **(b)** Comparison of the integrated PL intensities at different pump powers for typical mixed-phase nanoneedle (blue) and WZ-phase nanoneedle (red), at 4K (solid dots) and 298K (empty dots). The emission from mixed-phase nanoneedles at room temperature is too weak to be collected below 1×10^3 mW/cm^2 power density (shown by the blue curve with empty dots).

3.7 Summary

This chapter discusses using optical characterization tools to probe the crystal phase and material quality of InP nanoneedles grown on silicon. It provides the guideline for growth conditions and lays the foundation for the next chapter.

In summary, high-quality InP nanoneedles were grown directly onto a silicon substrate using a low-temperature MOCVD technique. Three types of nanoneedles were explored, composed of ZB/WZ-mixed phase, mostly ZB-phase, and single-crystal WZ-phase, respectively. The optical properties of each category of nanoneedles were studied and linked to the physics of the different underlying band structures. Mixed-phase nanoneedles exhibit type-II emission from 4 to 298K, with significant blue-shift behavior observed up to 110K. The spatial separation of carriers leads to an extremely long recombination lifetime of 13.5 ns at 4K and an IQE of 10% at room temperature. In contrast, pure WZ-phase nanoneedles show a band-edge emission of 1.49 eV at 4K and 1.41 eV at 298K, which is approximately 80 meV higher than the bandgap of conventional ZB-phase InP. This more efficient band-edge emission results in a carrier recombination in the pure WZ-phase nanoneedles that is around 30 times faster (300 ps at 4K), and an IQE that is more than twice as large (25% at 298K), as compared to the mixed-phase nanoneedles. All three classes of nanoneedles are able to achieve optically-pumped lasing at different wavelengths, with an ultrafast lifetime of 50 ps. InP nanolasers grown on silicon could form the basis of long-wavelength heterostructure III-V lasers that are compatible with silicon technology. With higher bandgap and internal quantum efficiency, single-crystal WZ-phase nanoneedles are highly promising nanostructures for use in optoelectronic devices such as photovoltaic cells. We thus have found a good growth condition to provide an excellent material platform for nanoneedle/nanopillar-based optoelectronic devices.

Chapter 4
Wurtzite-phased InP Micropillars with Low Surface Recombination Velocity

The direct growth of III-V nanostructures on silicon has shown great promise in the integration of optoelectronics with silicon-based technologies. Our previous work showed that scaling up nanostructures to micro-size while maintaining high quality heterogeneous integration opens a pathway towards a complete photonic integrated circuit and high-efficiency cost-effective solar cells. In Chapter 3, we have demonstrated that single-crystal WZ-phase nanoneedles/nanopillars stand out among other crystal phases to serve as an excellent material platform for optoelectronic devices. In this chapter, we present a thorough study of the surface quality to further investigate the wurtzite-phased InP mateiral. Surface recombination velocity is crucial for evaluating surface quality especially for nanostructures, yet there has not been a straightforward and reliable methodology to obtain it. By simply combining internal quantum efficiency with carrier recombination lifetime, we obtain an accurate and surprisingly low surface recombination velocity of 1.1×10^3 cm/sec for InP micropillars. In addition, we extract, for the first time, the radiative recombination B coefficient of 2.0×10^{-10} cm^3/sec for pure wurtzite-phased InP. These values are comparable with those obtained from InP bulk. Exceeding the limits of conventional nanowires, our InP micropillars combine the strengths of both nanostructures and bulk materials, and will provide an avenue in heterogeneous integration of III-V semiconductor materials onto silicon platforms.

4.1 Carrier Recombination Lifetime and IQE

Surface recombination velocity (SRV) is historically used to evaluate the surface quality of materials. Its importance sparkles great interests in the realm of InP nanowires, with SRV values reported via different characterization methods [76], [77], [85], [86]. But the precisions of these values suffer from undesirable effects induced by polytypism and over-simplification through some level of estimations. Here, we demonstrate a new but straightforward methodology to characterize the surface quality of InP micro/nano-pillars as-grown on silicon, and compare our results with the well-known values of InP bulk.

Carrier recombination lifetime τ consists of a radiative portion τ_r and a non-radiative portion τ_{nr}, defined as

$$\tau^{-1} = \tau_{nr}^{-1} + \tau_r^{-1} = SRV \times (SA{:}V) + B \times N \quad (4.1)$$

where SA:V is the surface area to volume ratio, B is defined as the radiative recombination coefficient, and N stands for excess carrier concentration. The overall effective lifetime τ can be measured directly with time-resolved photoluminescence (TRPL). At room temperature, non-radiative recombination dominates such that τ_{nr} is shorter than τ_r. Hence with $\tau \approx \tau_{nr}$, SRV is usually estimated as $(SA{:}V \times \tau)^{-1}$. Although neglecting radiative recombination induces inaccuracies in calculating SRV, this estimation is still widely adopted because there was no

obvious way to separate τ_{nr} and τ_r. Here we propose a straightforward method to extract τ_{nr} and τ_r from τ, by simply considering another equation of these two unknowns. It is worth noting that this method was also proposed in ref 48 for another material system and purpose, similar time as our study was firstly conducted. And very recently Gao et al. proposed a different method to characterize IQE and τ, which requires steady-state condition [56], [87]. Another relevant study under pulsed excitation condition was also conducted and would be of interest here as well [88].

Figure 4.1 (a) lays out the experimental setup used to implement this method. It consists of the aforementioned μ-PL setup (blue background), in conjunction with time-correlated single-photon counting (TCSPC) facility (pink background) for TRPL measurement. In order to calculate SRV, carrier recombination lifetime τ is first obtained from TRPL measurement at 298 K, as shown in Figure 4.1 (b) highlighting the impulse response of the system. Under each pump power, the fitted effective lifetime τ within one pulse period (12.5 ns) contributes to one data point in Figure 4.1 (c). With the same series of pump powers, the "effective" internal quantum efficiency (IQE) is then evaluated within the same time window (12.5 ns) by normalizing the PL intensities (integrated across the whole spectrum from Figure 4.1 (d)) at 298 K with that at 4 K [79], displayed in Figure 4.1 (e). Assuming 100% of IQE is reached at 4 K under each pump power (P), IQE at room temperature is defined as $I_{298K}(P)/I_{4K}(P)$. It is worth noting that, the exact same pump conditions need to be used for Figure 4.1 (c) and Figure 4.1 (e), which is critical for our method here.
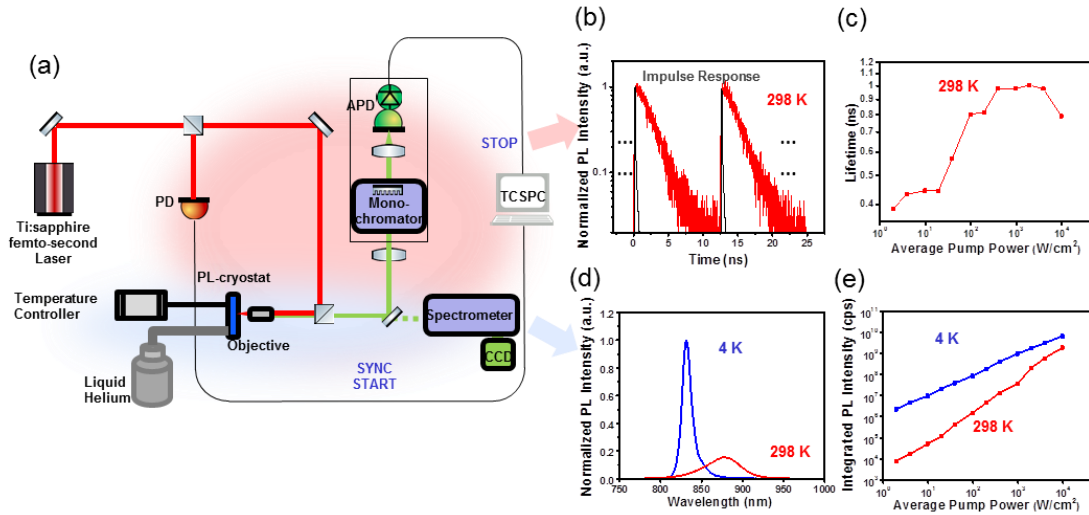
Figure 4.1 Experimental setup for photoluminescence measurements. **(a)** Layout of experimental setup, consisting of the μ-PL setup (blue background), combined with TRPL setup (pink background). **(b)** An example figure for a train of typical carrier lifetime decay curves (red) generated from TRPL setup at 298 K, with impulse response reflecting the system resolution of around 40 ps (dark gray). **(c)** An example figure of lifetime values fitted from (b), under different pump powers. **(d)** An example figure displaying typical PL spectra from a single pillar at 4 K (blue) and 298 K (red). **(e)** A figure exemplifying PL intensities (integrated over a span of wavelengths from (d)) under various pump powers, at 4K (blue) and 298 K (red), obtained with μ-PL setup. [8]

4.2 Methodology to Calculate Surface Recombination Velocity

In Figure 4.2 (a), we show the dependence of the overall carrier lifetime τ as a function of average pump power density. In the low injection regime, non-radiative recombination is the dominant factor. As the carrier density increases, more of the non-radiative recombination centers become saturated, τ therefore increases rapidly with pump power in this regime. At higher carrier injection level, however, τ becomes dominated by radiative recombination whose lifetime decreases with carrier concentration. Notably, this two-phase dependency has only been reported for InP bulk material [89]. The increase of lifetime in the low injection region was usually out of reach for nanostructures due to the low photoluminescence yield at room temperature. The key development enabling the capture of data lies in both the bigger size of our pillars and the compact µ-PL setup with high collection efficiency. Obtained under the same experimental conditions, IQE is plotted against carrier concentration, as depicted in Figure 4.2 (b). Theoretically, IQE can be expressed as

$$IQE = \tau_r^{-1} / (\tau_{nr}^{-1} + \tau_r^{-1}) \qquad (4.2)$$

Combining equations (4.1) and (4.2), the two unknowns τ_{nr} and τ_r can be resolved, revealing the fascinating physics underlying. The extracted τ_{nr} (red) and τ_r (green) are plotted against carrier concentration in Figure 4.2 (c). The effective lifetime τ (blue), the same as that shown in Figure 4.2 (a), is also included in Figure 4.2 (c) for easier comparison. It can be observed that at low injection level, τ_{nr} is almost equal to τ and increases until all non-radiative recombination centers are saturated at around 0.5 kW/cm^2, where τ is about 1.0 ns. As carrier injection gradually rises, τ starts to drop while τ_{nr} stays at around 1.2 ns. This validates that radiative recombination cannot be neglected especially at higher carrier concentration.

On the other hand, while appearing much longer than τ_{nr}, τ_r always decreases with carrier concentration based on the relation $\tau_r^{-1} = B \times N$ for undoped materials. By plotting τ_r^{-1} as a function of N in Figure 4.2 (d), the radiative recombination B coefficient can be obtained through linear fitting in the high injection regime. We note that the carrier concentration, is the most critical for the fitting of B coefficient. We adopted the method of estimating carrier concentration from Fermi level split, which was generated directly from PL intensity instead of pump power [90]. With a pulsed pump laser, the carrier concentration calculated here represents an averaged condition (see next section). The fitting result is just a preliminary estimation, and further work needs to be done as to improve the accuracy. Nevertheless, a value of 2.0×10^{-10} cm^3/sec is attained, which has never been reported experimentally for WZ-phased InP before. The fact that this is within the realm of the state-of-the-art numbers reported for ZB-phased InP bulk [91], [92] manifests the excellent emission efficiency of our InP micropillars. The high light extraction efficiency owes to the hexagonal pyramid shape, which is irregular enough so that photons not initially emitted into the escape cone have a higher chance of escaping after several internal reflections inside the pillar structure.
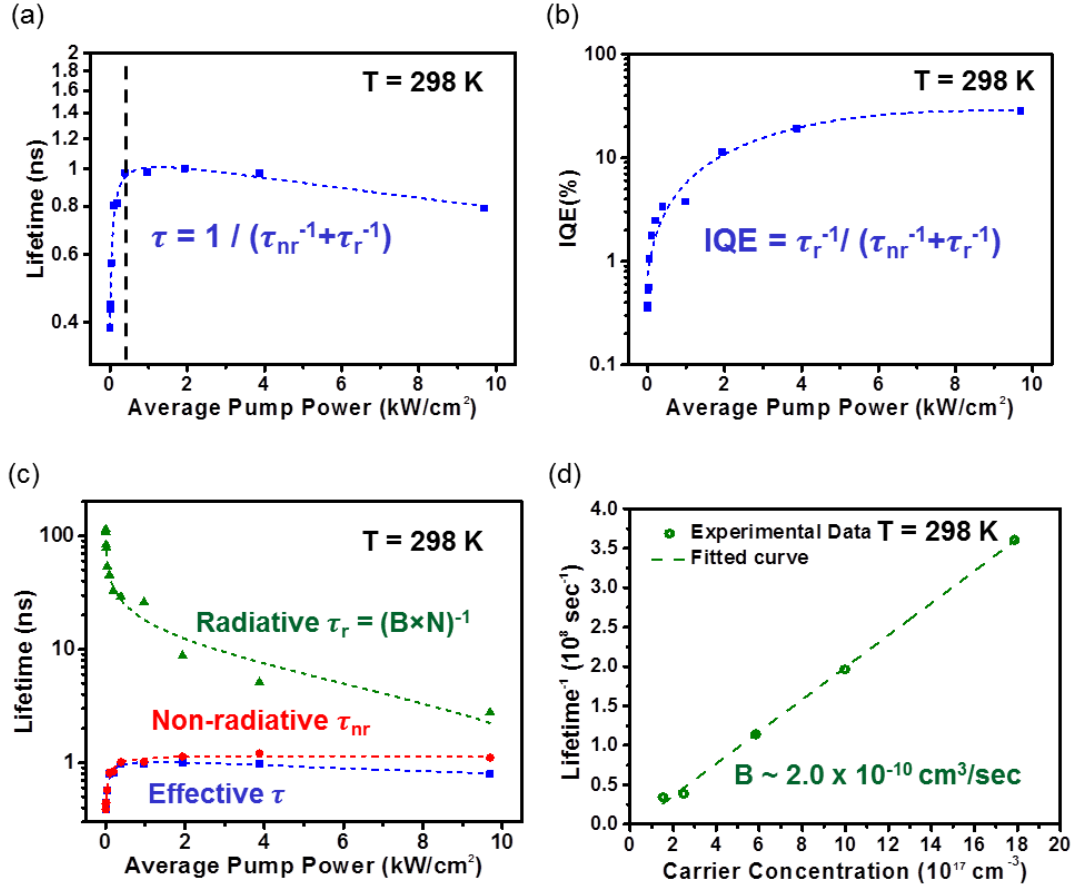
Figure 4.2 Methodology to separate τ_{nr} and τ_r. (a) Carrier lifetime τ measured from TRPL varying with average pump power density. **(b)** IQE values measured under the same condition as in (a). **(c)** Effective carrier lifetime τ (blue), the corresponding non-radiative recombination lifetime τ_{nr} (red) and radiative recombination lifetime τ_r (green), in dependence of average pump power density at 298 K, for the same pillar as in (a). Dashed lines in (a)-(c) are fitting curves merely to provide a guidance for the data points. **(d)** By fitting the green data in Fig. 4c with the relation $\tau_r^{-1} = B \times N$ in high carrier injection region, a radiative recombination coefficient B $\sim 2.0 \times 10^{-10}$ cm^3/sec is obtained. [8]

There are some tricky conditions that need to be stressed in order to better understand and utilize this method. First of all, the two equations we used (Equation 4.1 and 4.2) do not require steady state of rate equations. They are direct definitions independent of rate equations, and are valid at any instantaneous moment. Equation 4.1 [$\tau^{-1} = \tau_r^{-1} + \tau_{nr}^{-1}$] is a relation between effective carrier recombination lifetime τ, radiative lifetime τ_r , and nonradiative lifetime τ_{nr}. Equation 4.2 [IQE $= \tau_r^{-1}/(\tau_{nr}^{-1} + \tau_r^{-1})$] is also a direct definition of internal quantum efficiency or so-called "radiative efficiency" [93], which is the ratio between radiative carrier recombination rate and total carrier recombination rate. Therefore, these two equations are appropriate for both CW and pulsed excitations.

It is worth noting that the carrier concentration N in our work was not acquired from optical pump power. For carrier rate equation [$\frac{dN}{dt} = G_{gen} - R_{rec} = \frac{\eta_i I}{qV} - \frac{N}{\tau} - R_{st}$] [93] , a steady state is

not required unless one needs to relate recombination with generation $[\frac{\eta_i I}{qV} = \frac{N}{\tau} + R_{st}]$, so as to obtain carrier concentration N from injected current I (or optical pump power in our case). The methodology we used actually does not require this relation at any time, the carrier concentration information was obtained by another method, which will be explained in section 4.3.

Carrier recombination lifetime τ, especially the radiative part τ_r , is carrier concentration dependent. Therefore, the hidden information in Equation 4.2 is that IQE and τ need to have the exact same carrier concentrations at each instantaneous moment, so that $IQE(N) = \tau_r^{-1}(N)/[\tau_{nr}^{-1}(N) + \tau_r^{-1}(N)]$. Therefore, each data point in Figure 4.2 (b) for IQE corresponds to the exact same pumping condition as in Figure 4.2 (a) for TRPL. We understand that under pulsed excitation condition, the carrier concentration varies from some peak just after excitation to essentially zero as the carriers decay. This is exactly what a TRPL decay curve interprets, to show carrier recombination dynamics after an excitation pulse. In terms of our measurement in practice, the time period between pulses for our laser is T = 12.5 ns. And the carrier lifetime τ was fitted as a single exponential decay within this time window (12.5 ns), as an "effective" lifetime. Therefore, as long as the IQE was also an "effective" IQE averaged within this time window, it is consistent for both sides of the equation. Since the carrier lifetimes we obtained are in the range of τ = 1 ~ 7.5 ns, thus it takes 1.6 ~ 12 ns to emit most of the photons (estimated with $PL = 1 - e^{-\frac{t}{\tau}} = 80\%$). The PL signals used for IQE were collected within the valid regime of carrier recombination lifetime τ (12.5 ns), which makes this measurement consistent.

Pulsed laser also has to be used here for practical reasons. If a CW laser were used, a pump power equivalent to the peak power during a 120 fs pulse would have to be used, which would cause severe heating effects at room temperature. For example, for 1 mW of average power of our pulsed laser, peak power would reach 1mW * 12.5ns / 120fs = 104 W. The IQE values attained with CW pump under steady state were more conventionally reported, and certainly make more sense if one is to compare luminescence efficiency of a certain material systems with others [90]. This is not our purpose here, and the pulsed "effective" IQE is more appropriate for the method conducted in this work. Similar situations were reported popularly in the literature, by acquiring this "effective" IQE with pulsed excitation [79], [94]. To conclude, we believe it is both theoretically correct and practically more suitable to conduct our experiments with pulsed excitation for our purpose here.

Furthermore, the InP pillars studied here are intrinsic and not intentionally doped, with a background doping density of around $10^{15} \sim 10^{16} cm^{-3}$ in general. Note that we fitted B constant in the high injection regime where the injected carrier concentration is on the level of $10^{17} cm^{-3}$, large enough to neglect the background doping. Even if we included background doping concentration of $10^{16} cm^{-3}$, and used the relation $\tau_r^{-1} = B(N_D + N)$ instead, the fitting result we obtained for B was also around $2 \times 10^{-10} cm^3/sec$.

4.3 Method to Calculate Carrier Concentration N for Fitting B Constant

In order to fit for the radiative recombination B constant in Figure 4.2 (d), an exact carrier concentration N value needs to be obtained. Here we show our method of obtaining N.

Luminescence intensity $I_{sp}(hv)$ (photon counts per second per energy interval per area) at the pillar surface can be estimated from the PL counts obtained in experiment. For pulsed condition, we estimated that the photons were collected within the rectangular time intervals (t) equal to carrier recombination lifetime (τ). The effect of this approximation is shown in Fig. S1. Therefore, the pulsed $I_{sp}(hv)$ is adjusted as

$$I'_{sp}(hv) = I_{sp}(hv)/ \text{ (number of pulses per second) / (carrier recombination lifetime } \tau). \quad (4.3)$$

The relation between $I'_{sp}(hv)$ and Fermi level split ΔF can be expressed as [90]

$$I'_{sp}(hv) = \alpha \cdot \frac{(hv)^3}{4\pi^2 h^3 c^2} \cdot \frac{1}{e^{\frac{hv-\Delta F}{kT}}} \quad (4.4)$$

Therefore, corresponding Fermi level split values can be calculated, with an estimation of absorptivity (α) of our pillar from numerical simulation,

$$\Delta F = hv + kT \cdot ln[\frac{4\pi^2 h^3 c^2}{\alpha \cdot (hv)^3} \cdot I'_{sp}(hv)] . \quad (4.5)$$

In the high injection regime, when the excess carrier density ($> 10^{17} cm^{-3}$) is large compared to the background doping concentration of the material ($10^{15} \sim 10^{16} cm^{-3}$), the carrier concentration N can be expressed as

$$N = [n_i^2 \cdot e^{\frac{q \cdot \Delta F}{k \cdot T}}]^{1/2}. \quad (4.6)$$

With the calculation above, the fitted B constant is $\sim 2.0 \times 10^{-10} cm^3/sec$. The error of this estimation mainly comes from the accuracy of carrier recombination lifetime τ. In the case of Figure 4.3, the standard error from fitting τ is around 0.6%, which causes 0.01% deviation in ΔF, resulting in an error of only 0.3% in the carrier concentration N. Therefore, the fitted value for B is justified for pulsed excitation, with a standard error of 0.3%.
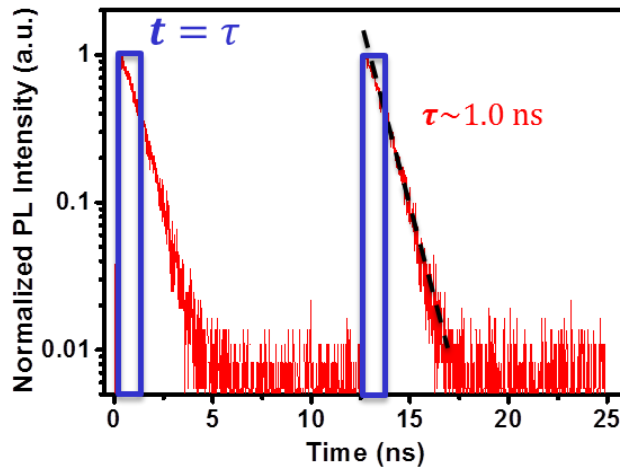
Figure 4.3 The effect of the approximated carrier concentration. TRPL decay curves with a time period of 12.5 ns between the pulses, and a fitted lifetime of around 1.0 ns (in red). Carrier concentration calculated is taken as a constant value (in blue) right after the laser pulse, which lasts for a time interval (t) equal to carrier recombination lifetime (τ). [8]

Please note that in Figure 4.2 (a-c), the specific carrier concentration numbers are actually not needed at all for the purpose there. The only part in our study that requires specific carrier concentration numbers is fitting for B constant in Figure 4.3. With the carrier concentration as an averaged value here, the B constant we obtained is a preliminary estimation. The purpose of doing it here is to show the B constant calculated with this method is comparable to the reported value for ZB-phased InP. For WZ-phased InP, no experimental result of B has ever been reported. We think this preliminary B value from our experimental method will be of interest for the general audience of Nano Letters.

4.4 Evaluation of Surface Quality

To evaluate the effect of growth temperatures on the surface and crystalline quality of the InP micro/nano-structures, we performed TRPL and IQE measurements upon pillars grown at three different temperatures. Important information including τ_{nr}, τ_r and SRV are then extracted using the same methodology outlined above. SRV values are estimated from the saturated value of τ_{nr} and are compared for pillars grown at 450, 455, 460 °C while keeping other growth conditions constant. Comparison of lifetime progressing with carrier concentration is illustrated in Figure 4.4 (a). More than one hundred pillars were examined, and our data reveal that an increase in growth temperature can significantly improve τ_{nr} and SRV of the micro/nano-structures. We attribute these enhancements to the annealing of pillar surface as well as the reduction of possible non-radiative recombination centers in the crystal lattice. In all the three samples grown at different temperatures, τ_{nr} first increases then decreases with injected carrier concentration, similar to what we observed in Figure 4.2 (a) (Figure 4.4 (a) is plotted in log-log scale for clearer comparison). Taking the longest lifetime at the saturation point for each trace in Figure 4.4 (a), we plot the corresponding TRPL decay curves, displayed in Figure 4.4 (b). The effective carrier lifetime τ of each trace is obtained by single exponential decay function fitting. We took full set of data as in Figure 4.4 (a-b) for around 60 pillars, the lifetime spread is summarized as below:

(1) For pillars grown at 450 °C, $\tau = 0.98$-1.15 ns with an average of 1.03 ns;
(2) For pillars grown at 455 °C, $\tau = 1.30$-3.36 ns with an average of 2.01 ns;
(3) For pillars grown at 460 °C, $\tau = 3.59$-8.58 ns with an average of 5.55 ns.

Table in Figure 4.4 (c) summarizes the important parameters, including τ, τ_{nr}, and SRV, of the example pillars grown at different temperatures studied in Figure 4.4 (a-b). It is worth noting that the lifetime of micropillars synthesized at 460 °C can be as long as 7.4 ns, with the non-radiative portion calculated as 10.4 ns. This is the longest lifetime detected at room temperature for InP micro/nano-structures, to the best of our knowledge. Moreover, the SRV of the micropillars can reach ~1.1×10^3 cm/sec, which is favorably comparable with the reported value in InP bulk material [95], [96]. These exciting results verify that the WZ-phased InP micropillars studied here are endued with superior surface quality while still possessing the unique advantage of nanostructures, which is of paramount importance for various optoelectronic devices.

(c)

Growth temperature (°C)	τ (ns)	τ_{nr} (ns)	Surface recombination velocity (cm/sec)
450	1.0	1.2	12.0×10^3
455	2.4	3.4	5.0×10^3
460	7.4	10.4	1.1×10^3
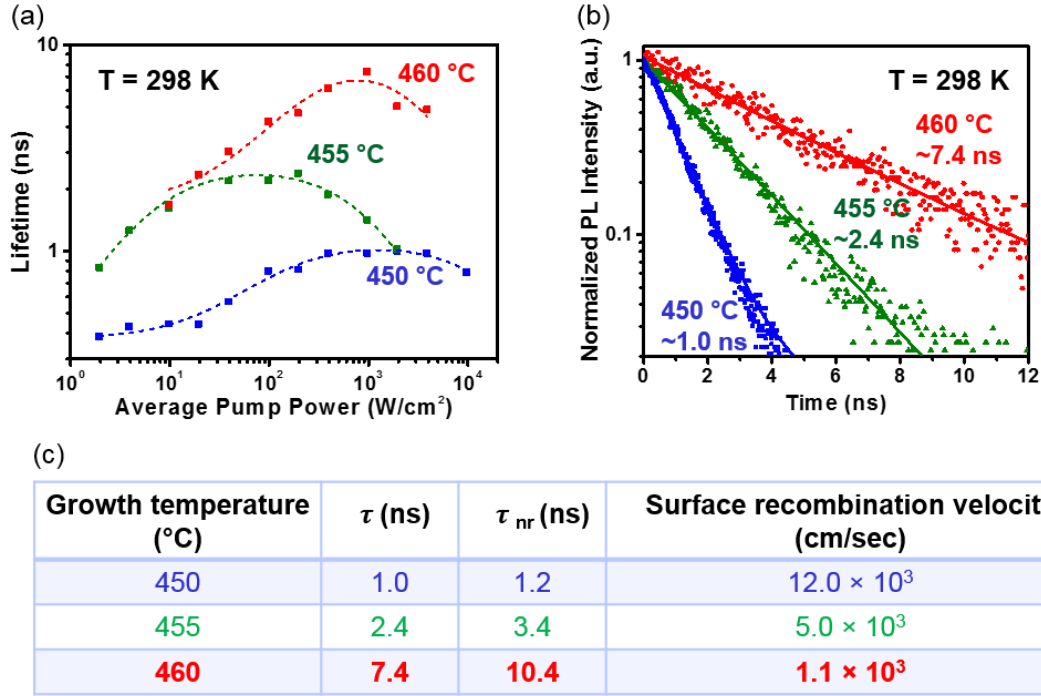
Figure 4.4 Carrier recombination lifetimes of InP micropillars. (a) Comparison of carrier lifetimes (τ) varying with average pump power density, for micropillars grown at 450 ℃ (blue), 455 ℃ (green), and 460 ℃ (red). **(b)** Corresponding TRPL decay curves for the micropillars in (a), by taking the longest lifetime at the saturation point for each trace. **(c)** A summary of values obtained of τ, τ_{nr}, and SRV for micropillars grown at at 450 ℃ (blue), 455 ℃ (green), and 460 ℃ (red). [8]

Non-radiative recombinations occur mainly at crystal defects and surface states. Embodied by the HR-TEM image in Figure 2.8 (d), misfit dislocations are confined at the InP/Si interface where the lattice-mismatch strain is relaxed, leading to excellent material quality in the bulk part remote from the hetero-interface. When we broke the root part of micropillars from as-grown silicon substrate and transferred them to a foreign silicon substrate, a remarkable increase in carrier lifetime was observed. Figure 4.5 (a) exemplifies that after being transferred, the lifetimes of micropillars grown at 450 ℃ can be doubled compared with that of a typical as-grown micropillar (1.0 ns). Such drastic improvement proves the high concentration of non-radiative recombination centers, i.e. misfit dislocations, is indeed well confined in the root part of micropillar and at the InP/Si interface. Carrier lifetime also shows great improvement after surface passivation with wet chemical etching, i.e. HCl(2M):H_2O:Citric Acid(0.5M) = 1:1:0.5 [97]. For micropillars grown at 455 ℃, lifetimes before and after surface passivation were compared for the same pillar, showcasing in Figure 4.5 (b) an improvement from 1.9 ns to 2.9 ns. Combining these two experiments, we conclude that the non-radiative recombination takes place both at the defect centers inside the pillar body and at free surface outside the pillar. Therefore, a more rigorous form of Equation 4.1 should be written as

$$\tau^{-1} = \tau_{nr}^{-1} + \tau_r^{-1} = (\tau_{body}^{-1} + \tau_{surf}^{-1}) + \tau_r^{-1} = \tau_{body}^{-1} + SRV \times (SA{:}V) + B \times N, \qquad (4.7)$$

47

where τ_{body} and τ_{surf} separate the effects from non-radiative recombinations inside the material body and outside at the surface. From this new form we can tell that the method in our previous context underestimated the value of τ_{surf} and thus overestimated SRV. The real SRV values should be even smaller than the results reported above. In our attempt to quantify τ_{body} by measuring nanopillars with different diameters as reported in ref [56], however, similar relations was not found between τ_{nr} and d, indicating τ_{body} might also be changing with the diameter. A more complete method to further separate τ_{body} from τ_{surf} in order to characterize SRV even more accurately is beyond the scope of the present work, and remains a topic for future investigation. However, we observed that SRV values of micropillars grown at 460 ºC can be improved by neither mechanical removal nor chemical surface passivation. Thus the SRV of ~1.1×10^3 cm/sec exhibits a good evaluation of material surface quality for our case here. Meanwhile, this again agrees with our hypothesis that higher growth temperature not only reduces the concentration of misfit defects inside micropillar body, but also anneals the surface. Further increasing the growth temperature is also not of interest here, since a lower growth temperature is desired for a more flexible CMOS post-process thermal budget [37]. All of our optoelectronic devices were based on InP pillars grown at 450 ºC, which have already shown excellent performances [7], [49], [50].
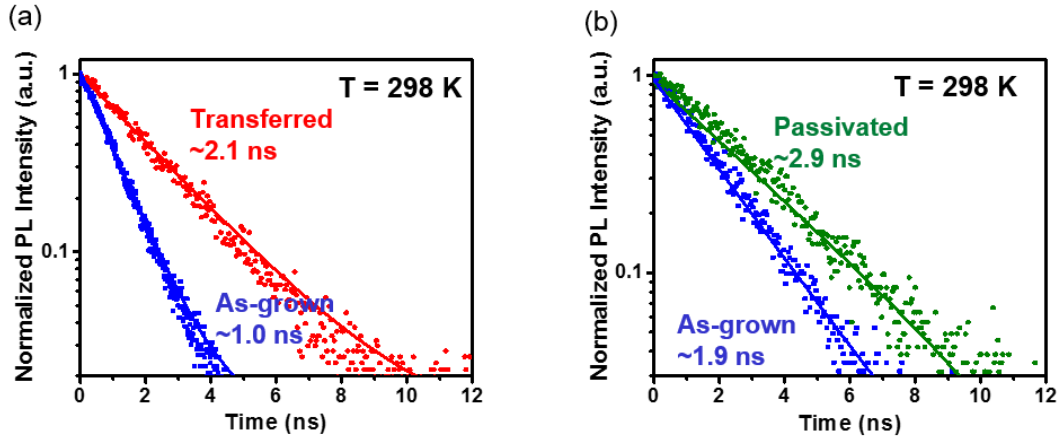
Figure 4.5 Carrier recombination lifetimes of InP micropillars. (a) Example of the lifetime improving from ~1.0 ns (blue) to ~2.1 ns (red) after being transferred from its as-grown silicon substrate to a foreign silicon substrate, for a micropillar grown at 450 ºC. **(b)** Example of the lifetime improving from ~1.9 ns (blue) to ~2.9 ns (green) after wet chemical surface passivation, for a micropillar grown at 455 ºC. For (b)-(d), TRPL decay data (dots) are fitted with single exponential decay function (curves) to obtain the values of τ. [8]

4.5 Summary

The combination of carrier recombination lifetime and IQE values measured at room temperature facilitates the separation of radiative and non-radiative parts of the lifetimes and enables revelation of key information. From non-radiative lifetime, SRV is calculated and found to improve as growth temperature increases. Micropillars grown at 460 ºC yields an SRV value of ~1.1×10^3 cm/sec, signifying a remarkable surface quality compared with conventional nanowires.

Radiative recombination B coefficient is also characterized, for the first time for wurtzite-phased InP. Both SRV value and B coefficient are close to the reported values for ZB-phased InP bulk. The above material and optical studies show that the InP micropillars integrated on silicon are endued with advantages of both bulk material and nanostructures. This unprecedented metastable direct growth of InP micropillars monolithically on silicon provides an avenue in the integration of optoelectronics with silicon-based technologies.

Chapter 5
High-Contrast Grating for Integrated Optoelectronics

High contrast grating (HCG) is an emerging element in integrated optoelectronics. Compared to other elements, HCG has very rich properties and design flexibility. Some of them are fascinating and extraordinary, such as broadband high reflectivity, and high quality factor resonance - all it needs is a single thin-layer of HCG. Furthermore, it can be a microelectromechanical (MEMS) structure. These rich properties are readily to be harnessed and turned into novel devices. In this chapter, we will investigate the physical origin of the extraordinary features of HCG, and explore its applications in novel devices for integrated optoelectronics.

5.1 High-Contrast Subwavelength Grating

Optical gratings are among the most fundamental building blocks in optics. They are well understood in two regimes: the diffraction regime where the grating period (Λ) is greater than the wavelength (λ), and the deep-subwavelength regime where the grating period is much less than the wavelength. However, there lies a relatively unexplored third regime, where the grating period is between the wavelength of the high-index grating material and that of the low-index surrounding material. The gratings show distinctive characteristics in this regime which are enhanced by higher index contrast. We call it sub-wavelength or near-wavelength regime.

In physics, a high contrast grating is a single layer of near-wavelength grating physical structure where the grating material has a large contrast in index of refraction with its surroundings. The refractive indices for HCG bars and the low-index surrounding materials range in 2.5~3.6 and 1.0~2.5, respectively. To suit the purpose of this dissertation, the second low-index material in the substrate beneath HCG bars are ignored, thus HCG bars are fully surrounded by the same low-index material such as air. The schematic of such a HCG structure is depicted in Figure 5.1. Please note that other types of gratings usually have no index contrast between the grating bars and the substrate. Furthermore, the period of grating bars lies in the subwavelength domain of the low-index material. The light shines on the top surface of HCG with incident characteristic angles θ and φ - the incident direction between the incident beam and the y-z or x-z plane, respectively. Two special conditions are $\varphi = 0$ and $\varphi = 90°$, where the light propagation direction is perpendicular and parallel to the grating bars respectively. Thus we term the former case as transverse magnetic (TM) and later as transverse electric (TE) polarization. The HCG is polarization sensitive by its nature of 1D periodicity.
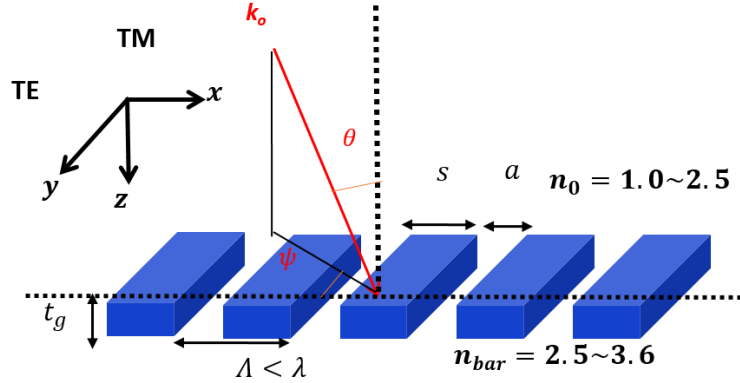
Figure 5.1 Simplified HCG structure, showing subwavelength grating bars with high-index material surrounded by low-index material. The period of the grating Λ lies between the wavelength of the low-index material and that of the high-index material. The bars have a thickness of t_g, width of s, and airgap of a.

The theory of HCG has been extensively studied and summarized in [15]. A brief overview is given here to explain intuitively how it works. Figure 5.2 (a) plots the schematics of HCG in a three-coordinate system. We assume along y-direction the grating bars are uniform and infinite, while them being periodic in x direction. The grating bars can be considered as merely a periodic array of waveguides with wave being guided along z direction. The thickness of the bars is exaggerated to show the wave propagation inside. The plane is divided into three regions, with region I and II interfaced by input plane while region II and III interfaced by exit plane. Upon its incidence at the input plane, light will couple into multiple waveguide array modes in region II. In Figure 5.2 (b) we show the mode profile of the different modes. The 0th-order and 2nd-order mode profiles are both symmetric across the HCG bar, but the 1st-order mode is asymmetric. These modes propagate to the exit plane and get reflected. They reach the input plane and get reflected again. After some bounces back-and-forth, eventually there would be reflection light from the input plane and transmission light coming out of the exit plane. The HCG properties can be fully explained by waveguide array modes and their interference due to abrupt index change at the input and exit planes. If two modes fully destructively interfere, thus to cancel each other at the exit plane, then high reflection is achieved at the input plane. On the other hand, when two modes are perfectly impedance matched with the input plane, then high transmission is realized at the exit plane. The thickness of an HCG is one of the most important design parameters since it determines the interference effect. It is realized that in order to better govern HCG properties, the best working condition with HCG is with only two guided modes. It is worth noting that when it's surface-normal incidence, only even modes can be excited. Thus we mostly work with 0th-order and 2nd-order modes. Therefore, we call this wide wavelength range the "dual-mode regime", where only two waveguide array modes have real propagation constants in z direction and, hence, carry energy. This is a unique feature of HCG, being distinct

from diffraction optical gratings, guided mode resonance, Wood's anomaly, and photonic crystals.
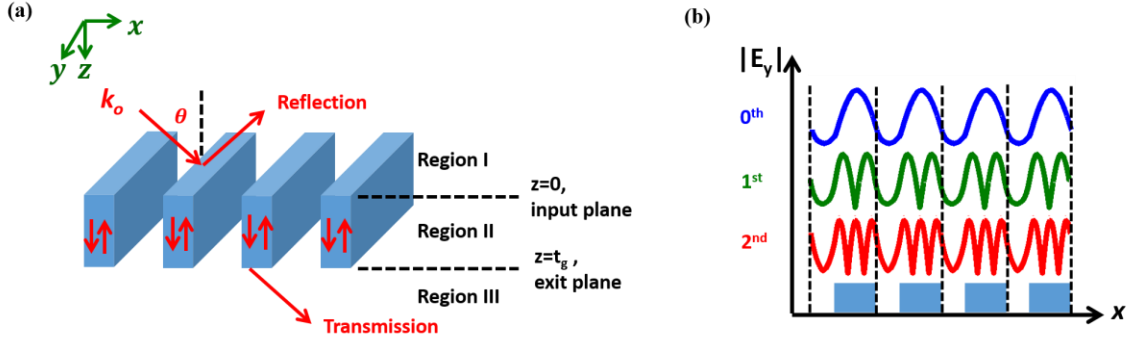
Figure 5.2 Working principle of HCG. **(a)** Light is incident at the input plane of HCG and propagates along z-axis inside HCG bars to excite waveguide array modes, whose characteristics can be fully explained by interference effect. **(b)** Mode profile in the x-y plane of the waveguide array modes inside HCG.

Figure 5.3 displays the reflectivity contour versus wavelength λ and HCG thickness t_g, for TE-polarized and TM-polarized optical gratings under surface-normal incidence, respectively. In both cases, a fascinatingly well-behaved, highly ordered checker-board pattern appears and reveals a strong dependence on both λ and t_g. This is the dual-mode regime located between the cutoff wavelengths of the 2nd-order and 4th-order waveguide array modes.
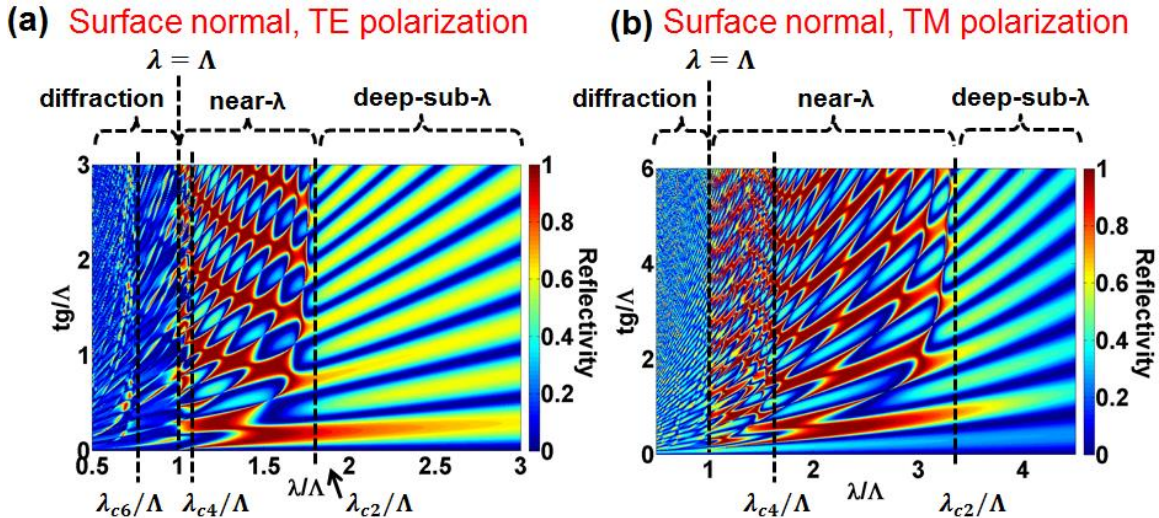
Figure 5.3 Simulated reflectivity contour plot for (a) TE mode and, (b) TM mode optical gratings with a certain thickness t_g in three wavelength regimes – diffraction regime, deep subwavelength regime, and the near/sub-wavelength regime.

The unique and rich properties of HCG have enabled a large variety of applications, which have promoted HCG from a simple optical element to a platform for functionality integration of optoelectronics. The characteristics of HCG include but are not limited to ultra-high reflection and transmission over a broad spectral range and/or various incident beam angles, phase front engineering, high optical Q resonance, coupling, filtering, optomechanical effect, etc. Various optoelectronic devices and functionalities have been demonstrated using HCG as the key element, such as tunable HCG-VCSELs [9], [10], low-loss hollow-core waveguide [13], planar reflectors and lenses [12], fast optical phased array for beam steering [98], vertical-to-in-plane coupler [99], high Q resonators for bio-sensing [100], optical switches [101], laser optomechanics [14], etc. A complete review of the HCG properties and applications can be found in [15].

In this dissertation, we focus on two key features of HCG and their implementations in one of the most important semiconductor laser categories - vertical-cavity surface-emitting laser (VCSEL). Before we introduce what HCG can offer in a VCSEL environment, it is necessary to give a brief overview of VCSEL including its advantages and challenges. This is done in the next section.

5.2 Vertical-Cavity Surface Emitting Lasers

5.2.1 Semiconductor Diode Laser

A diode laser is an electrically pumped semiconductor laser in which the active laser medium is formed by a p-n junction of a semiconductor diode similar to that found in a light-emitting diode. The laser diode is the most common type of laser produced with a wide range of uses that include fiber optic communication, barcode readers, laser pointers, optical storage disc reading and recording, laser printing, laser scanning and directional lighting sources [102].

The first semiconductor diode lasers were fabricated in 1962 using homojunctions [103]. These lasers had high threshold current density and operated at cryogenic temperatures with low conversion efficiency. The concept of heterostructure semiconductor diode laser in 1969-1970 was a major breakthrough, with lasers realized at a low threshold current density (over ten times lower) and room temperature operation [103]. These double-heterostructure diode lasers provide both carrier and optical confinements, which improve the efficiency for stimulated emission, and make it possible to be used in practical applications. In 1970, the concept of quantum-well structures for diode lasers was proposed and realized experimentally [103]. The reduction of the confinement region for the electron-hole pairs to a tiny volume in the quantum-well region improves the laser performance significantly. In the late 1980s, strained quantum-well lasers were proposed to further improve the laser performance [103].

Two other important classes of lasers are gas lasers and solid-state lasers. The helium-neon (HeNe) gas laser and the Nd-doped YAG solid-state laser are two representations. Diode lasers differentiate from the other types of lasers primarily by the ability to be directly pumped by an electrical current, which leads to more than an order of magnitude higher power conversion efficiency compared with gas and solid-state lasers. Net size is another striking difference, with gas and solid-state lasers typically of tens of centimeters in length while semiconductor lasers in

the order of a cubic centimeter or so after fully package. In addition, semiconductor diode lasers have high reliability and long lifetime which can last on the order of hundreds of years, compared with thousands of hours for gas or solid-state lasers. However, semiconductor lasers usually have less coherent output thus wider linewidth compared with other lasers with much longer cavities. The use of diode lasers to pump solid-state lasers, e.g. diode-pumped Nd-YAG, may be a good way to combine the best advantages of both categories [93].

5.2.2 Evolution of VCSEL

Conventionally, semiconductor diode lasers are edge-emitting. As demonstrated by the schematics in Figure 5.4 (a), it consists of an active gain region (i.e. quantum well), two cleaved mirrors on two sides embracing the cavity to provide optical feedback, as well as top and bottom contacts forming a pn junction to provide pump energy (i.e. electrical pump) for the laser. The directions of current flow and optical feedback are therefore perpendicular to each other. Vertical-cavity surface-emitting lasers (VCSELs), however, have the optical cavity axis along the direction of current flow, as depicted in Figure 5.4 (b). The laser resonator consists of two distributed Bragg reflector (DBR) mirrors parallel to the wafer surface with an active region for the light generation in between. The two DBRs are doped as p-type and n-type respectively to enable current injection in the same direction as optical feedback.

Compared with edge-emitting lasers, VCSELs have some advantageous characteristics. First of all, the short cavity leads to large free spectral range (FSR), making it handy to achieve lasing in single longitudinal mode. The short cavity and small footprint also reduce lasing threshold and power consumption. Furthermore, the edge-emitting laser cannot function until it is cleaved out of a wafer to form the reflection mirrors at last. In contrast, the surface-emitting VCSELs facilitate wafer-scale fabrication and diagnostic testing during any fabrication step, which greatly boosts the fabrication yield and saves cost. In addition, the larger and better-defined output aperture on top of VCSEL produces a lower divergence angle of the output beam with high beam quality. This assists high-efficiency light coupling into optical fibers and other elements.
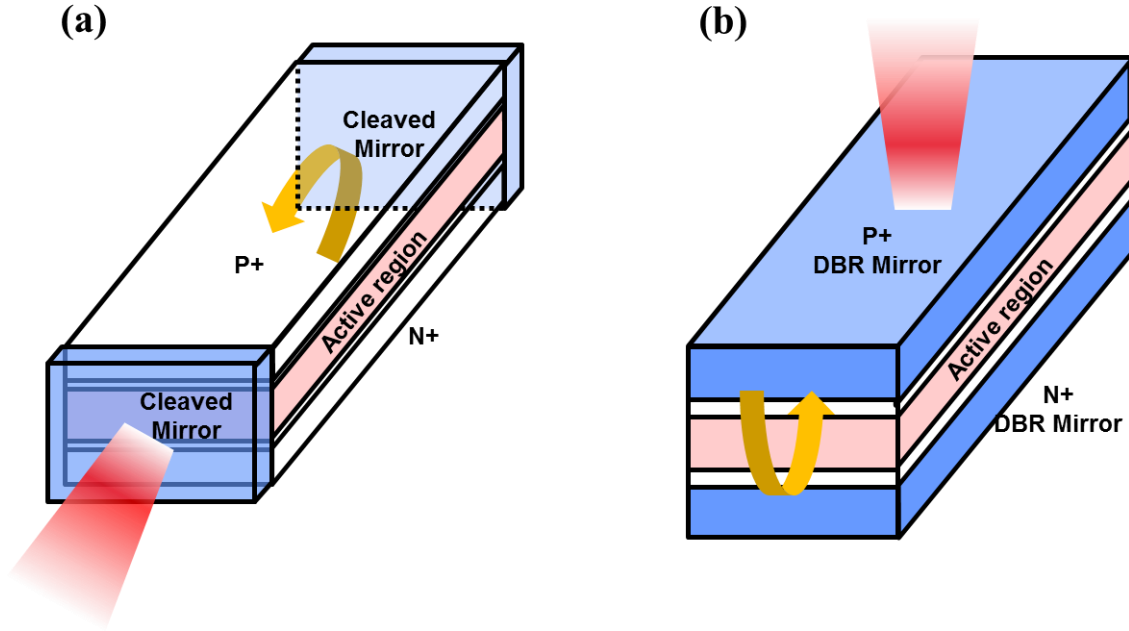
Figure 5.4 Structure comparison of surface-emitting lasers and VCSEL. (a) Schematics of a conventional edge-emitting semiconductor diode laser with the current injection perpendicular to optical feedback direction. The laser outputs beam from the side mirror. **(b)** Schematics of the typical VCSEL structure, with optical feedback between DBR mirrors in the same direction as current injection. The laser outputs beam from the mirror at the top surface.

However, things tend to behave like a double-edged sword. The short cavity of VCSEL causes a small overlap between the active gain region and optical field. It then relies on the mirrors to provide a much higher optical feedback to achieve lasing. A reflectivity above 99% is generally required for both DBR mirrors. The planar DBR-mirrors consist of layers with alternating high and low refractive indices. Each layer has a thickness of a quarter of the laser wavelength in the material. In general, the higher the required reflectivity is, the more high/low index pairs of DBR are needed. This does not only pose challenge to epitaxial growth, but also makes the fabrication process more complicated. The choice of materials for DBR pairs must accommodate index contrast and material compatibility (i.e. the match of lattice constant and thermal expansion) between the two materials. For GaAs-based VCSELs working in the short wavelength range (850-980 nm), GaAs/AlGaAs pair is a good candidate for DBR mirror. However, for InP-based long-wavelength (> 1μm) VCSELs, none of the few choices like InGaAsP/InP, AlInGaAs/AlInAs, or AlGaAsSb/AlAsSb offer an as-good index contrast. As the simulation shows in Figure 5.5, in order to achieve a reflectivity of 99.5%, the material combination suitable for long-wavelength VCSELs need to include more DBR periods compared with GaAs/AlGaAs. In addition, a general rule of thumb is, the more types of elements a compound semiconductor has, the worse the thermal conductivity becomes.
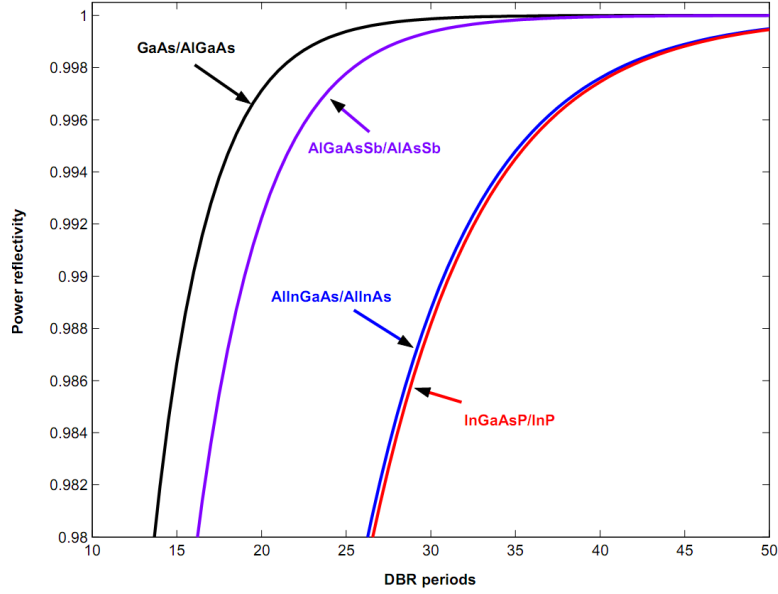
Figure 5.5 Comparison of the structures of edge-emitting laser and VCSEL. (a) Schematics of a conventional edge-emitting semiconductor diode laser with the current injection perpendicular to optical feedback direction. The laser outputs beam from the side mirror. **(b)** Schematics of the typical VCSEL structure, with optical feedback between DBR mirrors in the same direction as current injection. The laser outputs beam from the mirror at the top surface. Figure was adapted from [104], [105].

5.2.3 MEMS Tunable VCSEL

By integrating a MEMS (microelectromechanical system) structure with VCSEL cavity, one can change the length of optical cavity and thus tune the emitting wavelength. Bulk micromachining techniques are widely used to integrate silicon MEMS with CMOS microelectronics. Unlike surface micromachining, which uses a succession of thin film deposition and selective etching to create structures on top of a substrate, bulk micromachining defines structures by selective etching of the substrate. When this idea is generalized to the realm of MEMS VCSEL, it not only means the bonding of half VCSEL with silicon-based MEMS mirror, but also covers MEMS mirror made with other materials.

   As mentioned in the last section, the InP-based long-wavelength VCSEL platform lacks of appropriate material candidates to form DBR pairs with high index contrast and good thermal conductivity. Thus a lot of effort was devoted to the development of bulk-micromachined MEMS mirror for InP-based VCSELs. In ref. [106], the bulk-micromachined top mirror is made of dielectric material SiO_x/SiN_x and manufactured separately from the half-VCSEL. After bonding the top mirror with the half-VCSEL, the electrothermal energy actuates the top concave mirror thus tunes the wavelength. A single-mode continuous tuning range of 76 nm is realized around 1.55 µm. When made separately, the bulk-micromachined MEMS mirror also has more degrees of freedom for better design. For example, the concave shape of the top mirror here offers larger reflectivity for the center fundamental mode while suppresses higher-order side modes. This enables single-mode emission while keeping a large aperture for high output power. However, thermal tuning is usually very slow, on the order of hundreds of Hz. With electrostatic tuning, ref. [107] achieves 500 kHz tuning speed over 40-nm of tuning range. The InP-based

56

half-VCSEL chip was bonded on top of a silicon-on-insulator (SOI) chip with a silicon concaved MEMS mirror. A total tuning range of 55 nm was achieved around 1550 nm. However, bulk micromachining has several unavoidable disadvantages. First of all, the wafer bonding process is relatively complicated with low yield. The MEMS mirror and half VCSEL also need to be grown separately, which is rather costly. Furthermore, the bulk-micromachined MEMS is very bulky, limiting the tuning performance.

Surface micromachining overcomes the drawbacks of bulk micromachining. The first surface-machined MEMS VCSEL was experimentally demonstrated in 1995 [108], based on GaAs material system with emission wavelength around 935 nm. With the suspended MEMS cantilever, it achieves around 15 nm of tuning with electrostatic actuation. Following in 1996, single-mode tuning of 18 nm around 975 nm was demonstrated with a micromachined deformable membrane top mirror [109]. Throughout the years, several research groups have contributed to the major milestones in the performance improvement of MEMS VCSELs. The integration of dielectric DBR mirrors has largely increased the free spectral range (FSR) and extended the thermal MEMS tuning to over 102 nm [110].

5.3 HCG-VCSELs

5.3.1 High Reflection of HCG

As seen in Figure 5.3 for both TM and TE mode HCGs, in the dual-mode regime, there is the checker-board pattern with high reflectivity and low reflectivity periodically. These patterns strongly correlate with both HCG thickness (t_g) and wavelength (λ) and can be explained by interference effects. The reflectivity can reach as high as 100% with large tolerance in some areas.

Back in year 2004, Prof. Connie J. Chang-Hasnain and her students have discovered the unique broadband high reflectivity of this single layer of monolithic material [111], [112]. As described in the last section, due to the reduced gain overlap factor in the vertical cavity, VCSEL has very high requirement for mirror reflectivity, typically >99.5%. The traditional DBR mirror consisting of multiple layers of high/low index material pairs is not only bulky, but also poses challenge to epitaxial growth and fabrication. Figure 5.6 (a) plots the reflectivity over wavelength for both DBR and HCG. It is seen that HCG can offer reflectivity as high as DBR with almost three times broader bandwidth. Thus, this thin layer of monolithic gratings can actually replace the bulky DBRs as the reflection mirror in VCSEL. This is realized by bringing the index contrast from the vertical direction to the horizontal direction. Taking the structure in Figure 5.6 (b) as an example, an AlGaAs-based DBR mirror with R>99.5% is often as thick as $6\mu m$ with around 40 DBR pairs. But an AlGaAs-based HCG mirror with similar high reflectivity is only ~200 nm in thickness. This also leads to an over 100 times reduction in weight, promising for faster MEMS actuation. In addition, HCG mirror is polarization selective, which is desired for some applications such as optical coherence tomography (OCT).
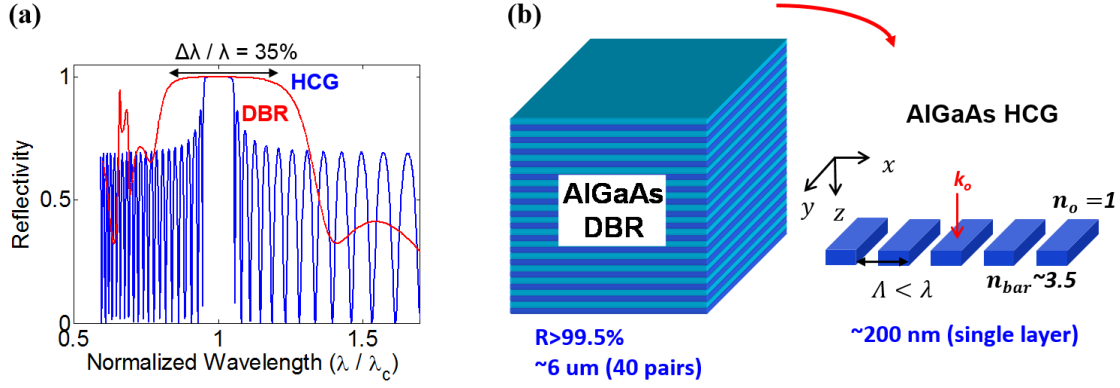
Figure 5.6 Comparison of DBR and HCG as high reflection mirrors. (**a**) HCG offers almost three times wider high-reflectivity range compared with a conventional DBR. (**b**) A ~60 μm thick bulky AlGaAs-based DBR mirror can be replaced by a single layer of HCG with only ~200 nm in thickness.

5.3.2 HCG Design in VCSEL

To design the HCG so that it can be utilized as a high reflection mirror, the first step is finding the correct thickness for the required wavelength. Figure 5.7 plots the dual mode region for TM mode and TE mode correspondingly. We can see multiple regions of high reflectivity close to 1. If we take λ=850 nm for example, then t_g=235 nm is a good design for TM mode while t_g=145 nm works well for TE mode. It is worth noting that usually a thinner thickness is preferred for fabrication feasibility. And a large fabrication tolerance can be obtained if the point we choose is located at the center of a big high-reflectivity region.
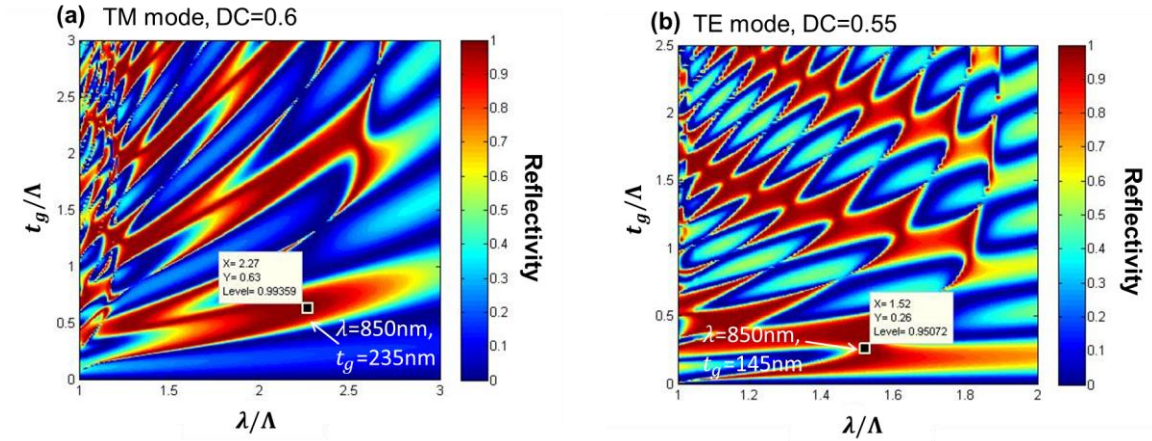
Figure 5.7 Simulated reflectivity contour plot with HCG thickness (T_g) versus wavelength (λ) reflectivity contour plot for (**a**) TM mode HCG under DC = 0.6, highlighting a high reflectivity design with λ~850 nm and t_g~235 nm. (**b**) TE mode HCG under DC = 0.55, highlighting a high reflectivity design with λ~850 nm and t_g~145 nm.

As mentioned above, a high fabrication tolerance of the HCG design is strongly desired, in order to control quality and reduce fabrication cost. The HCG thickness is determined by epitaxial growth with $\pm 10\%$ accuracy, and the period can be accurately written with ebeam lithography within $\pm 0.5\%$. The airgap (spacing between HCG bars) usually suffers from fluctuations of ebeam of about ± 20 nm, plus the variations during the following dry etching step. While fabrication errors are unavoidable, a design with large fabrication tolerance would be very much helpful. Figure 5.8 (a) shows the reflectivity contour with HCG airgap (a) versus period (Λ) for HCG design at λ=850 nm. A tolerance of >100 nm can be seen for HCG airgap with high reflectivity. If we pick Λ=385 nm and a=160 nm then plot out the reflectivity versus wavelength, a wide bandwidth of ~65 nm is achieved for TM mode, as seen in Figure 5.8 (b). Polarization selection is very important here, because VCSEL is prone to polarization mode hopping during direct modulation. We can see that while TM mode has a reflectivity >99%, that of TE mode is only around 55% which is far below the lasing requirement.
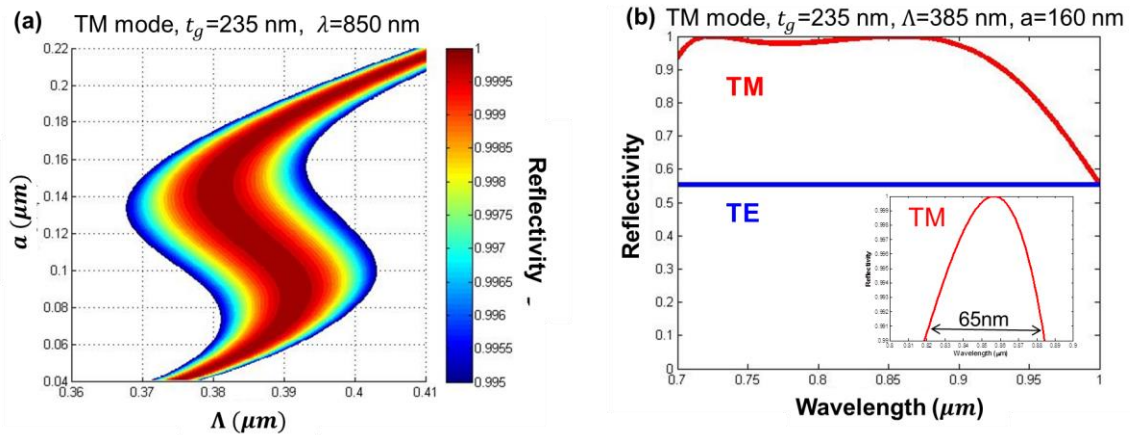
Figure 5.8 Simulated reflectivity of a TM mode HCG with thickness of 235 nm. (a) Reflectivity contour plot with HCG airgap (a) versus HCG period (Λ) simulated at λ=850 nm. **(b)** Reflectivity versus wavelength for one HCG design with Λ=385 nm and a=160 nm, showing a polarization selection towards TM mode with 65-nm bandwidth for R>99%.

5.3.3 Tunable HCG-VCSEL

The first HCG-based highly reflective mirror was experimentally demonstrated in year 2004 using a silicon HCG on top of SiO_2 [107], [111]. In 2007, we adapted this high reflection mirror to replace DBRs as the top mirror in VCSEL and demonstrated continuous-wave (CW) lasing HCG-VCSEL at 850 nm under room temperature [113]. Following in 2007 and 2008, we reported MEMS tunable HCG VCSEls with a 20-nm tuning range and 27 MHz tuning speed [9] [114]. A 1300-nm and 1550-nm InP-based HCG-VCSEL were demonstrated in 2010 [115], [116]. And in 2013, a single-mode tunable 1550-nm HCG-VCSEL with tuning range of 26.3 nm was achieved [10]. The tunable VCSEL was used as a source of external modulation for 40-Gbps differential-phase-shift-keyed signal and transmitted over 100-km dispersion-compensated link with negligible power penalty. In order to facilitate low-cost light sources for integrated silicon photonics, scalable flip-chip eutectic bonding was used in 2015 to produce VCSEL

heterogeneously integrated on a silicon-on-insulator (SOI) substrate. The hybrid laser adopted AlGaInAs-silicon as optical cavity with HCG reflector on the SOI substrate [117]. The VCSEL operates at silicon transparent wavelengths ~1.57 μm with >1 mW CW power outcoupled from the semiconductor DBR, and single-mode operation up to 65 °C. We achieved a 3-dB direct modulation bandwidth of >2.5 GHz, and error-free transmission over 2.5 km single-mode fiber was realized under 5 Gb/s direct modulation. A flexible HCG-VCSEL embedded in PMDS was also realized, which might open a new revenue for flexible light sources [118].

We show a GaAs-based 850-nm tunable HCG-VCSEL adopting the HCG design in Figure 5.9 as an example below. The design and fabrication methods are similar with [9]. An SEM image of a finished device is displayed in Figure 5.9 (a), highlighting the HCG MEMS mirror fully suspended and surrounded by air. Being supported by the two MEMS beams on both sides, the HCG can freely move downward with electrostatic actuation to realize continuous wavelength tuning. The light-current-voltage (LIV) characteristics in Figure 5.9 (b) demonstrated an ultralow threshold current of ~200 μA, output power of ~160 μW and turn-on voltage of about 2.5 V. The inset spectrum shows a single-mode lasing around 836 nm with side-mode suppression ratio (SMSR) of ~30 dB.
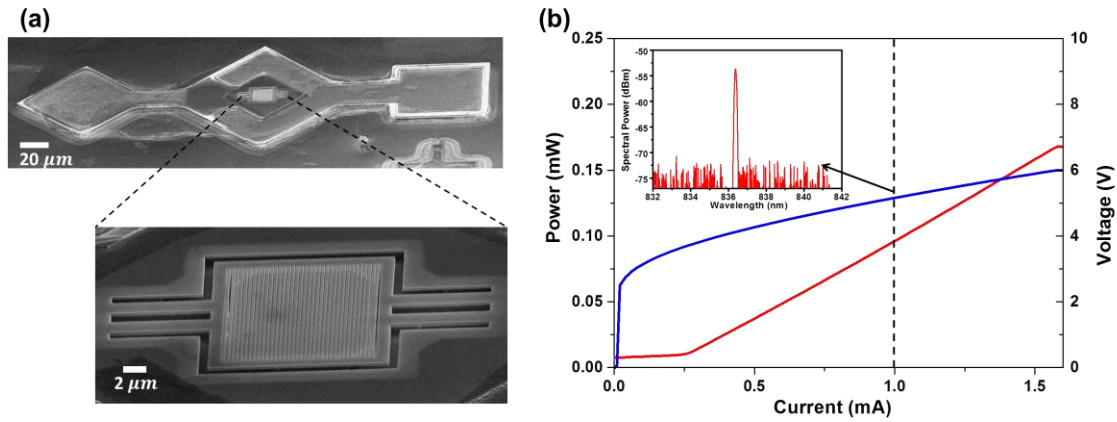
Figure 5.9 GaAs-based 850-nm tunable HCG-VCSEL. (a) SEM image of a finished HCG-VCSEL device, with an zoom-in view of the HCG area fully suspended in the air and supported by the MEMS tuning beams. **(b)** The LIV characteristics of a typical 850-nm single-mode HCG-VCSEL under CW operation.

A continuous wavelength tuning of ~14 nm was realized here, by applying a voltage on the HCG MEMS for electrostatic actuation. As shown in Figure 5.10 (a), without applying tuning voltage, the laser emits at 837 nm. And by increasing the tuning voltage, HCG MEMS will be pulled downward thus make the optical cavity shorter. Upon 4.6 V, the wavelength is tuned to ~832 nm before it stops lasing. When the voltage is further increased, another longitudinal mode that exists in the cavity starts lasing from the longer wavelength ~845 nm and continuously shifts to the center wavelength. The total tuning range accounting for the two longitudinal mode reaches ~14 nm here. We looked into the reason that limits the tuning range and simulated the HCG reflectivity contour of tuning airgap versus wavelength. The lasing resonance wavelength at each point obtained from performing rigorous coupled-wave analysis (RCWA) method of the

whole optical cavity was then overlaid on top of the reflectivity contour as in Figure 5.10 (b). It clearly shows that the reflectivity bandwidth of this particular HCG design poses a limit on the tuning range, and can be further improved by optimizing the HCG design.
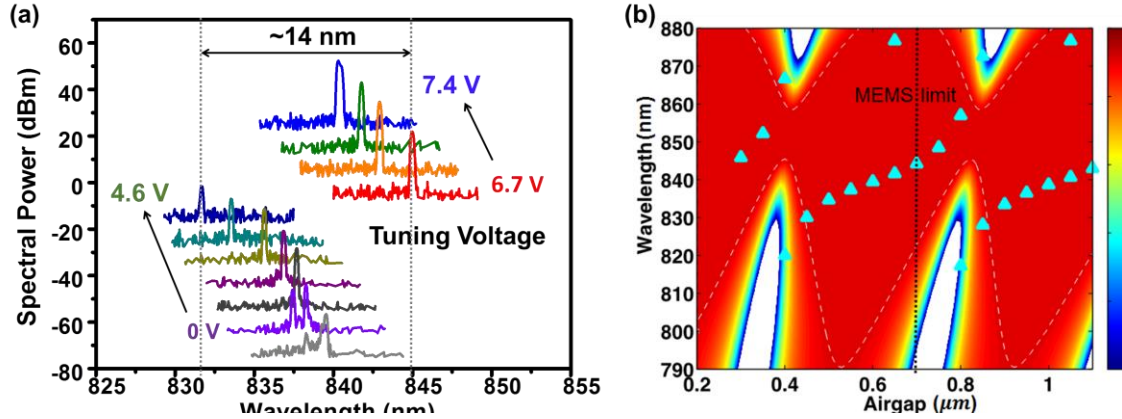
Figure 5.10 Wavelength tuning of the GaAs-based 850-nm HCG-VCSEL. (a) Tuning spectrum showing a continuous single transverse mode tuning of ~14 nm under CW operation. **(b)** Reflectivity contour of the HCG design in (a) with wavelength versus tuning airgap. The cavity resonance wavelength overlaid on top of the contour points out that the limitation of wavelength tuning here is caused by the reflectivity bandwidth of this particular HCG design.

5.4 Summary

Vertical-cavity surface-emitting lasers (VCSELs) are key optical sources in optical communications, with the advantages of low power consumption, low packaging cost, and ease of fabrication into arrays as well as wafer scale testing. Our group has developed a revolutionary single-layer, high-index contrast sub-wavelength grating (HCG), and implemented it as a reflection mirror in VCSEL. Compared with conventional reflective Bragg reflector mirrors (DBR), the seemingly simple-structured HCG provides ultra-broadband high reflectivity (R>0.99, $\Delta\lambda/\lambda$>35%) and high quality-factor resonance (Q>107). Monolithic, continuously tunable HCG-VCSEL has been demonstrated at 850 and 1550 nm. The ultrathin HCG drastically reduces the required VCSEL epitaxial thickness and greatly increases the tolerance toward variations in fabrication. The small footprint of HCG enables the scaling down of the mechanical actuator's structural geometry by at least a factor of 10, leading to over 1000 times reduction in the overall structural mass and a huge increase in the mechanical tuning speed. The widely tunable HCG-VCSEL will present extraordinary performance in applications such as optical communication, light detection and ranging. Its potential wide reflection band and fast tuning speed will be highly promising for high-resolution, real-time imaging in optical coherent tomography (OCT).

Chapter 6
HCG as Integrated Tuning Mirror for VCSEL

6.1 Motivation of 1060-nm tunable VCSEL

Vertical-cavity surface-emitting lasers (VCSELs) are key light sources in a variety of applications, including but not limited to data communications, optical interconnects, high-resolution displays, as well as laser sensing and printing. Compared with conventional edge-emitting lasers, the nature of vertical optical cavity endues VCSELs with numerous advantages. First of all, the relatively short vertical cavity makes it less challenging to achieve single-mode laser emission. The high-quality beam emitted from top surface is also easy to be coupled into fibers and other optical elements. Being able to be fabricated into arrays, wafer-scale VCSEL fabrication facilitates high-yield and low-cost mass production. Furthermore, the small footprint of VCSELs leads to small power consumption thus high energy efficiency.

Wavelength tunable VCSEL gained its popularity by enabling key functionalities in optical communication through wavelength-division multiplexing (WDM). The recent emergence of swept-source optical coherent tomography (SS-OCT) as well as light detection and ranging (LIDAR) poses another demand for mode-hop-free, fast and widely tunable VCSELs. Tunable VCSELs embracing microelectromechanical structures (MEMS) are promising due to its continuous tuning characteristics which lead to power efficiency and reduced cost.

The wavelength of 1060nm has been recognized as the most suitable for ophthalmic OCT (optical coherence tomography) imaging because it enables visualization of the choroidal vascular structure [119]. Although MEMS tunable VCSELs at other wavelengths (i.e. 850nm, 1550 nm) have been extensively developed, the first MEMS-VCSEL at 1060 nm was not demonstrated until very recently [119]. The work adopted HCG as the top mirror and anti-reflection coating design in the cavity. But it showed limited laser performance, such as a high threshold current of ~1 mA and a limited direct tuning range of around 15 nm. Another 1060-nm MEMS-VCSEL was reported last year with excellent tuning performance ranging up to ~64 nm [120]. However, despite the compromised thermal performance constraint by the dielectric DBRs, it also has very high requirements for epitaxial growth and fabrication process. This might hinder the mass production in large scale with low cost.

The simply-structured high-contrast grating (HCG) with subwavelength periods suspended by two beams works as an ultra-broadband high-reflectivity mirror and an ultrathin lightweight MEMS actuator [15]. Tunable HCG-VCSELs at 850 nm and 1550 nm have been previously demonstrated by our group [9], [10]. Here, we report a monolithic tunable 1060-nm VCSEL using an HCG as the tunable mirror and wet oxidation to provide current confinement, leading to a wafer-scale, low cost fabrication process. Single-mode CW operation up to 110 ℃ is demonstrated, with a lasing threshold as low as 100 µA, and output power higher than 1.3 mW at room temperature. A wide continuous tuning range up to 40 nm was achieved.

6.2 Design

Design of the HCG-VCSEL structure here is depicted in Figure 6.1. The as-grown 1060-nm epitaxial wafer consists of 38 pairs of bottom DBRs as the bottom reflection mirror. Multiple strained InGaAs/GaAsP quantum wells provide the optical gain. The current and electrical confinement is realized by oxidizing the $Al_{0.98}GaAs$ layer, leaving only a small laser aperture. The suspended top HCG mirror offers high reflectivity benefitting from its high index-contrast with the surrounding air and its subwavelength dimensions. This structure is formed of n-p-n junctions, with the p-n junction forward biased to achieve lasing. By applying a voltage to the tuning contact to reverse bias the n-p junction, the HCG MEMS structure can be actuated electrostatically thus to tune the wavelength of the laser.
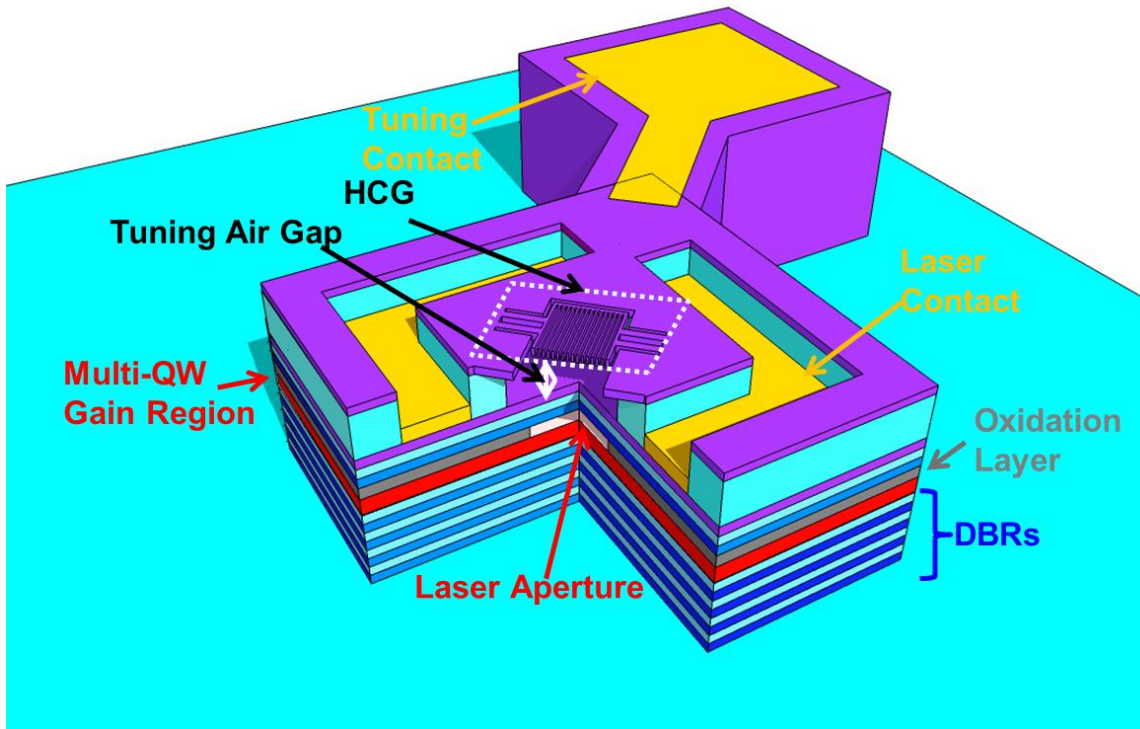
Figure 6.1 Cross-sectional schematics of a tunable HCG-VCSEL.

The general design of a VCSEL epitaxial wafer involves two important aspects: the optical design to maximize the overlap of the standing waves with the active region, and electrical design to provide efficient current flow into QWs and reduce the parasitic resistance. As shown in Figure 6.2, the green curve shows band diagram of the VCSEL material system, showing the p-i-n junction structure (the top n-p junction for laser tuning is not displayed). The red curve stands for the refractive index variation among the multiple layers, and the blue curve indicates the optical field intensity in this cavity. Optimization of the composition and thickness of each layer is performed during the optical cavity design. The goal is to achieve the largest

confinement factor or overlap integral between the standing waves and the QWs in the active region. This is the key to achieve low threshold and high output power for VCSELs. The confinement factor is calculated with transfer matrix method [103]. A value of ~1.3% is achieved here, which is limited by rather large penetration depth into the bottom DBRs. By replacing the bottom DBRs with material pairs with larger refractive index contrast, the confinement factor can be improved. To fulfill the round-trip condition of VCSEL cavity, the thickness of sacrificial layer needs to be designed carefully in response to the reflection phase carried by the selected HCG design.
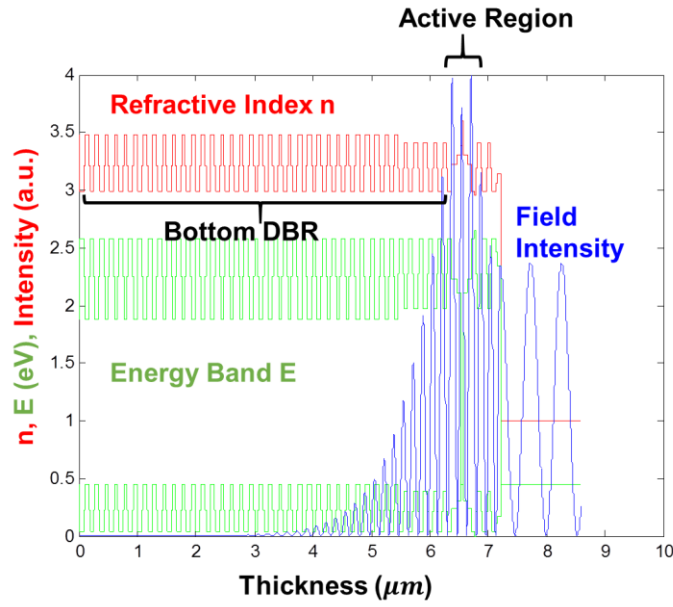
Figure 6.2 Cavity and energy band simulation of 1060nm HCG-VCSEL, including refractive index (red curve), electrical field intensity (blue curve) and band diagram (green curves).

Using the analytical tool from [121], the reflectivity contour map was simulated to facilitate the HCG design. In Figure 6.3 (a), the reflectivity distribution is plotted versus HCG thickness (t_g) and wavelength (λ) (both normalized by HCG period Λ) for TM mode. A thickness of ~300 nm is picked for λ=1060 nm with good fabrication tolerance. We then simulate the reflectivity versus HCG airgap (a) and period (Λ) with this wavelength and thickness. A range of dimensions that can be used to define HCG are then figured out, as shown in Figure 6.3 (b).

64
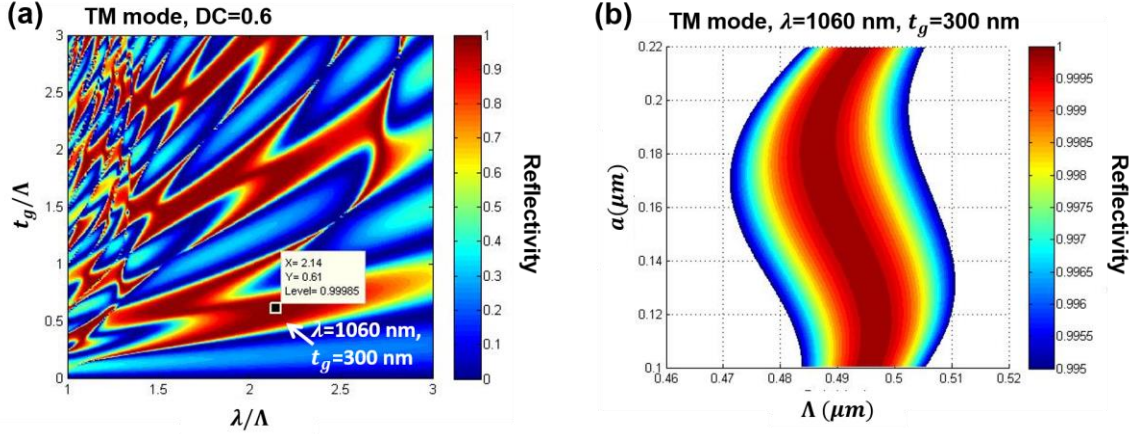
Figure 6.3 Simulated reflectivity contour plot for HCG design. **(a)** HCG thickness (T_g) versus wavelength (λ) reflectivity contour plot for TM mode HCG under DC = 0.6, highlighting a high reflectivity design with $\lambda\sim$1060 nm and $t_g\sim$300 nm. **(b)** Reflectivity contour plot with HCG airgap (a) versus period (Λ) simulated at λ=1060 nm, for a TM-mode HCG with thickness of 300 nm.

6.3 Fabrication

The designed wafer was grown by epitaxial vendor with multiple layers on a GaAs substrate, as shown in Figure 6.4 (a). From the bottom up, it consists of 38 pairs of DBRs, MQW active region, oxidation layer, 2 pairs of top DBRs, sacrificial layer for tuning gap, and then an $Al_{0.6}GaAs$ HCG layer. Here we briefly go through the fabrication process. The top tuning metal contacts are firstly deposited with electron beam deposition. Figures 6.4 (b) illustrates the cross-sectional layer structure and the corresponding top view of the device.

A 2D array of VCSEL devices are then patterned with UV optical lithography and etched by wet chemicals to form device mesas as in Figure 6.4 (c). Selective etching based on pH-buffered citric acid solution is used to achieve better uniformity throughout the wafer. Except for the uniformity at the bottom, the height of device mesa also influences the rate and quality of wet oxidation for laser aperture. As shown in Figure 6.4 (d), wet oxidation using a desktop furnace defines the aperture. Water vapor carried by nitrogen (N_2) flow oxidizes the $Al_{0.98}GaAs$ layer with a high selectivity of aluminum composition. The temperature, flow rate, and time are the main determinants for the oxidation rate. To realize single transverse-mode lasing, typically an oxidation aperture of <5 μm is needed for our HCG-VCSEL, which is more tolerant than the traditional double-DBR VCSELs. However, the yield of oxidation is still relatively low especially in a laboratory environment. In industry, some in-situ observation systems are used to control oxidation process. After wet oxidation, both light and electrical current will be confined in the conductive aperture, which partially determines the lasing threshold.

In Figure 6.4 (e), the n-p-n junction and multiple metal contacts are illustrated. Except for the top tuning contact biasing the n-type HCG layer, a laser contact is defined on the etched-down p-type laser contact layer. The etching is again realized through wet chemical selective etching. Therefore, the laser contact is used for current injection to forward bias the bottom p-n

junction to achieve lasing in the active region. And the tuning contact is used for voltage bias to reverse bias the top n-p junction for electrostatically tuning the HCG MEMS.

The most critical process step of fabricating the tunable HCG mirror occurs in the end of the whole flow, in order to preserve the shape and quality of the high-precision HCG dimensions. As illustrated in Figure 6.4 (f), the HCG dimensions are defined by ebeam lithography with precision of ± 10 nm. To improve yield, a range of HCG dimensions are written at once. Reactive ion beam (RIE) composed of $SiCl_4$ is used to dry etch the patterned HCG bars (Figure 6.4 (g)). The verticality and roughness of HCG sidewalls can be adjusted by gas flow and pressure in the chamber. After dry etching, HCG MEMS is then released in wet chemical. Ph-buffered citric acid solution is again used to etch away the GaAs sacrificial layer underneath while preserving $Al_{0.6}GaAs$ HCG bars. The tuning gap depth is very important for defining the cavity length, thus a complete etching of the sacrificial layer needs to be realized through sufficient etching time. We then use critical point drying (CPD) to completely release the MEMS structure. Figure 6.4 (h) demonstrates the finished HCG-VCSEL device.

(a)

(b)

(c)

(d)

(e)

(f)

(g)

(h)

HCG Layer: $Al_{0.6}GaAs$
Sacrificial Layer: GaAs
Oxidation Layer: $Al_{0.98}GaAs$
Active Region: 3 QWs

Bottom DBR pairs

Substrate: GaAs

Oxidized Aperture

Tuning Contact

N-type
Laser Contact (LD+)
P-type

N-type

Backside Contact (LD-)
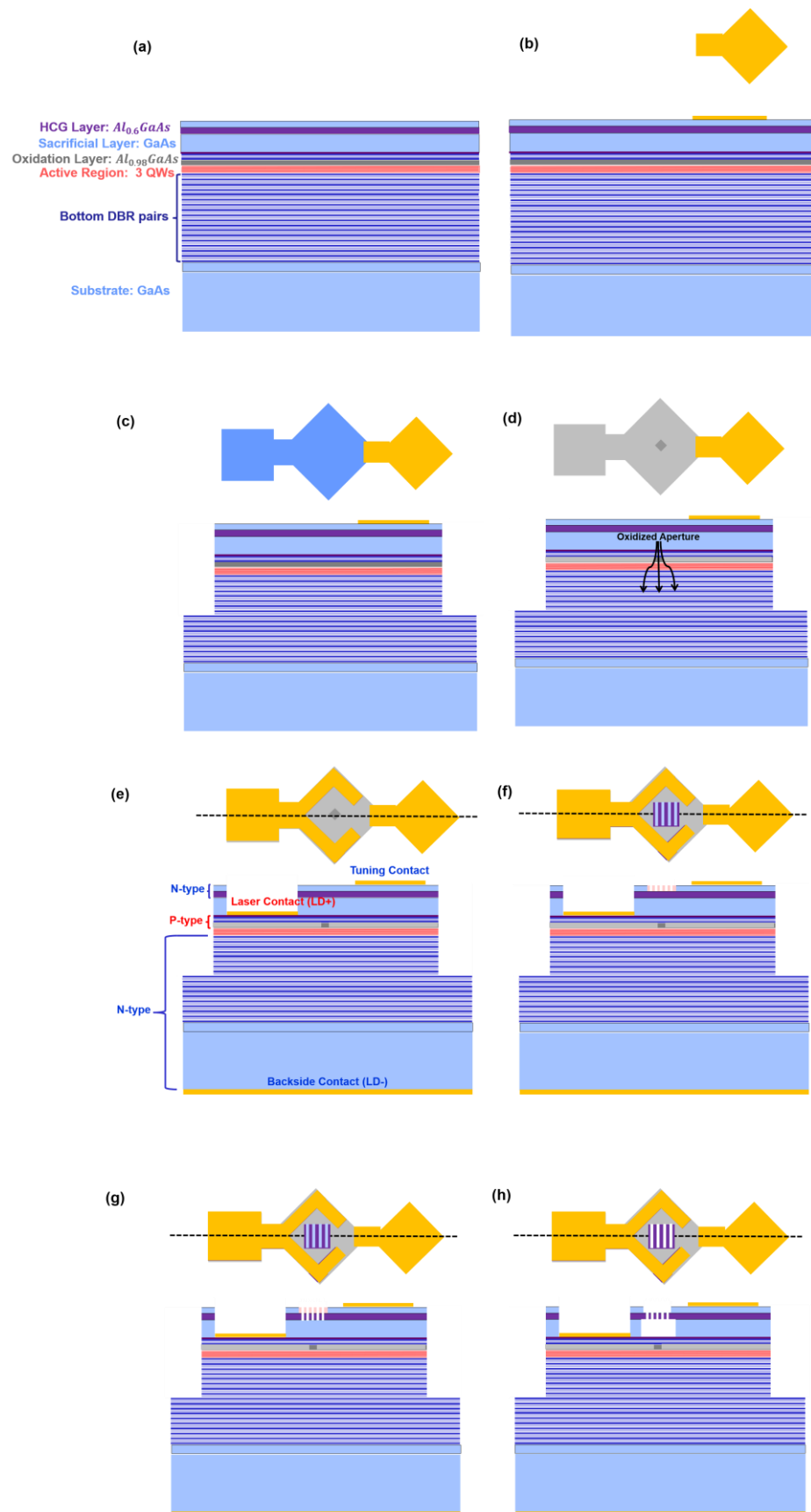
Figure 6.4 Schematics of the fabrication flow for oxidized tunable HCG-VCSEL. (a) Cross-sectional layer structure of the as-grown epitaxial wafer. Cross-sectional layer structure with the corresponding top-view of the device, after process of **(b)** tuning contact; **(c)** device mesa etching; **(d)** wet oxidation to form a small aperture for both optical and electrical confinements; **(e)** laser contact and bottom contact, with illustration of the n-p-n junction and all metal contacts; **(f)** ebeam lithography for HCG definition; **(g)** RIE dry etching of the defined HCGs; **(h)** release of HCG MEMS with selective wet chemical etching.

6.4 Performance

The scanning electron microscopy (SEM) image in Figure 6.5 (a) shows the top-view of a typical finished HCG-VCSEL device. The zoom-in image highlights the HCG MEMS mirror fully suspended and surrounded by the air. Being supported by the MEMS arms on both sides, the whole HCG mirror can be actuated with electrostatic tuning to realize wavelength shift. Figure 6.5 (b) displays an HCG array imaged by 3D confocal microscope, showing the ability for wafer-scale mass production.
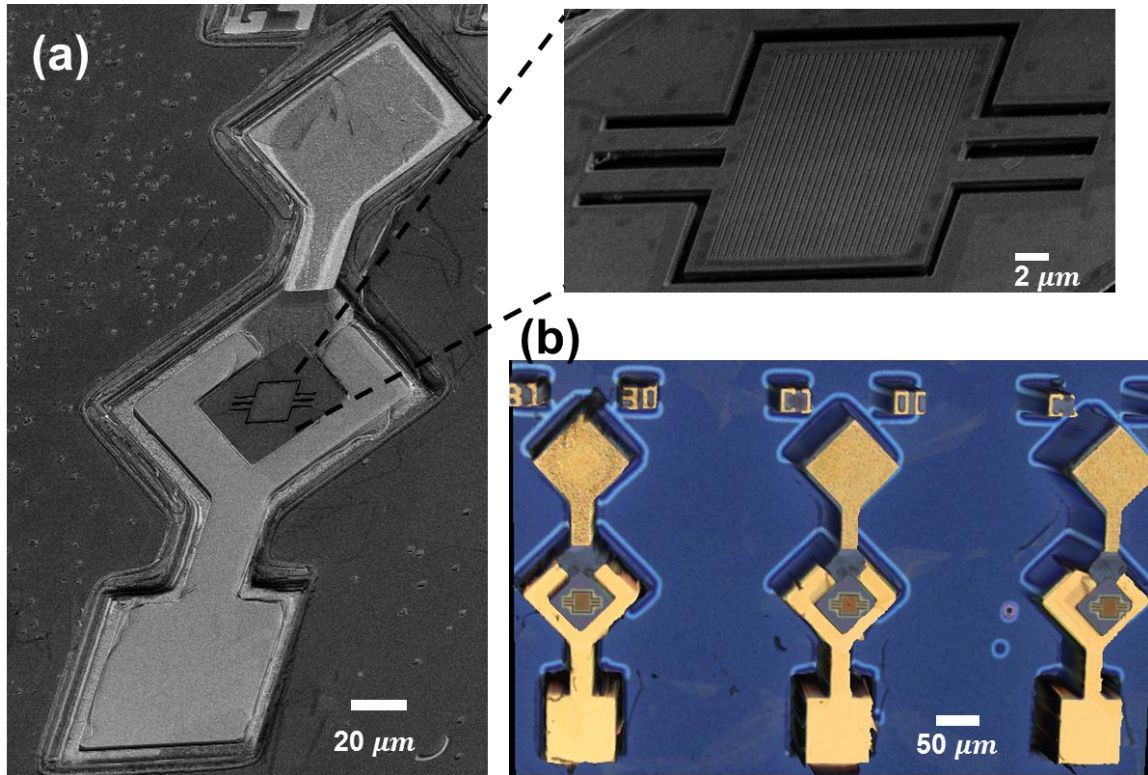
Figure 6.5 Images of a typical finished tunable HCG-VCSEL device. (a) Scanning electron microscope image of a typical HCG-VCSEL device, with a zoomed-in view of the fully suspended HCG surrounded by air. **(b)** 3D confocal optical image of the fabricated HCG-VCSEL array.

6.4.1 LIV and Spectra

With the laser aperture defined by wet oxidation to be smaller than 5 μm in diameter, the TM-mode HCG-VCSEL maintains single transverse-mode lasing under CW electrical operation. A Keithley current source is used to bias the VCSEL using electrical probing. Figure 6.6 shows the LIV (light-current-voltage) characteristics of a typical device at 20°C, showing a low threshold current of ~300 μA and output power of 1.3 mW at I=4 mA. The lowest threshold current we tested was ~100 µA. The inset spectrum demonstrates single longitudinal and transverse mode lasing at ~1056 nm with side-mode suppression ratio of >35 dB at room temperature. A Xenics InGaAs CCD camera captured the near-field emission of the device through a 100X objective at high gain sensitivity. While showing a small spot of spontaneous emission below lasing threshold (I_{th}), above lasing threshold, strong speckle patterns were observed which is a classic signature of lasing resonance. The laser has a voltage of ~8 V at 4 mA, indicating a series resistance of around 2 $k\Omega$. The series resistance can be improved by annealing the metal contact and optimizing the doping level in the current spreading layer. The wall plug efficiency is about 4%, which is mainly limited by the relatively high voltage and series resistance.
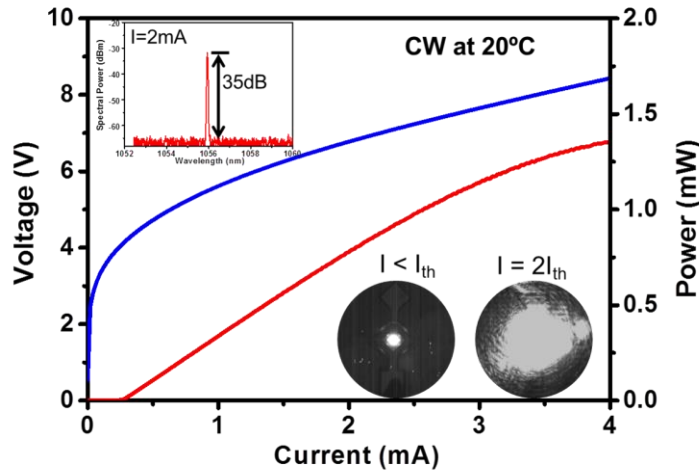
Figure 6.6 The LIV characteristic and spectrum (top inset) of a typical HCG-VCSEL under CW operation at 20 ℃, showing single mode lasing with side-mode suppression ratio of 35 dB at 2 mA, and output power of ~1.3 mW at 4 mA. The bottom inset images are captured by an IR camera from the top of the device for below lasing threshold (I < I_{th}) and after lasing (I = 2I_{th}).

Various temperatures are applied by the thermal electric cooler (TEC) to the copper chuck directly in contact with the VCSEL chip. And to our surprise, the single-mode lasing is sustained >110 ℃ heat sink temperature. Even at 110 °C, the output power still maintains at ~0.2 mW. Figure 6.7 illustrates the thermal behavior of the LIV characteristics. While the output power is reduced with the increased temperature, the threshold current does not undergo much increase. The VCSELs exhibit thermal rollover with increasing current bias due to gain spectrum red-shifting more rapidly than the resonant cavity spectrum, an effect typically seen in VCSELs [122].
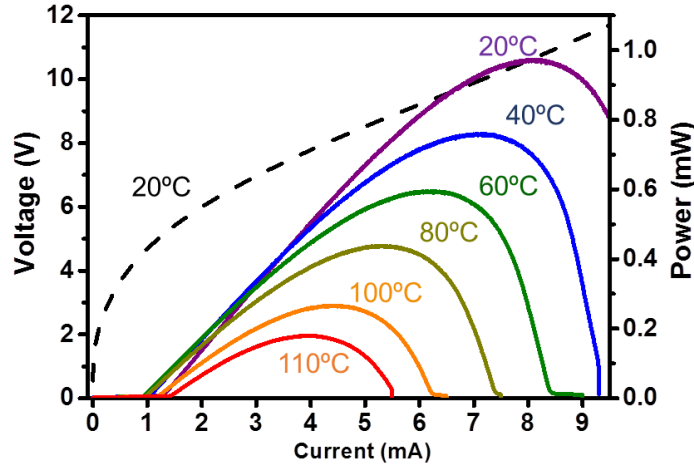
Figure 6.7 The LI characteristics under a series of heat sink temperature from 20 °C up to 110 °C. Output power is reduced while threshold current does not have obvious decrease. The IV characteristics at 20 °C is also shown and remains similar with temperature increase.

6.4.2 Thermal Characteristics

The thermal characteristic is critical for optimizing the device efficiency. The thermal resistance of the laser is defined by the following ratio,

$$R_{th} = \frac{\Delta T}{\Delta P} = \frac{\Delta\lambda/\Delta P}{\Delta\lambda/\Delta T} \qquad (6.1)$$

where ΔT, ΔP and $\Delta\lambda$ are the changes of temperature, thermal power and wavelength, respectively. The wavelength shift versus temperature under a fixed bias current $2I_{th}$ was firstly evaluated with the method above. As shown in Figure 6.8 (a), a fitted $\Delta\lambda/\Delta T$ ratio of 0.054 nm/°C can be extracted. This number is determined by index change versus temperature despite of type of laser. The wavelength shift versus dissipated thermal power was then characterized by increasing the injection current at a fixed temperature 20°C. Multiplying the bias current with the corresponding voltage and subtracting the optical output power, the thermal power can be calculated. The fitted ratio results in $\Delta\lambda/\Delta P$~0.061 nm/mW. Taking the two numbers to obtain the ratio, a thermal resistance of around 0.88 °C/mW is obtained. Oxide-confined laser aperture should be more prone to thermal heat compared with proton-implanted apertures because of its around 10 times smaller aperture here. To our surprise, the R_{th} number demonstrated above is almost only half of that for proton-implanted InP-based HCG-VCSEL [10], [117]. Compared with similar oxidized VCSELs, the thermal resistance is also smaller [123], [124]. This shows great promise for the material system design in our epitaxial wafer.
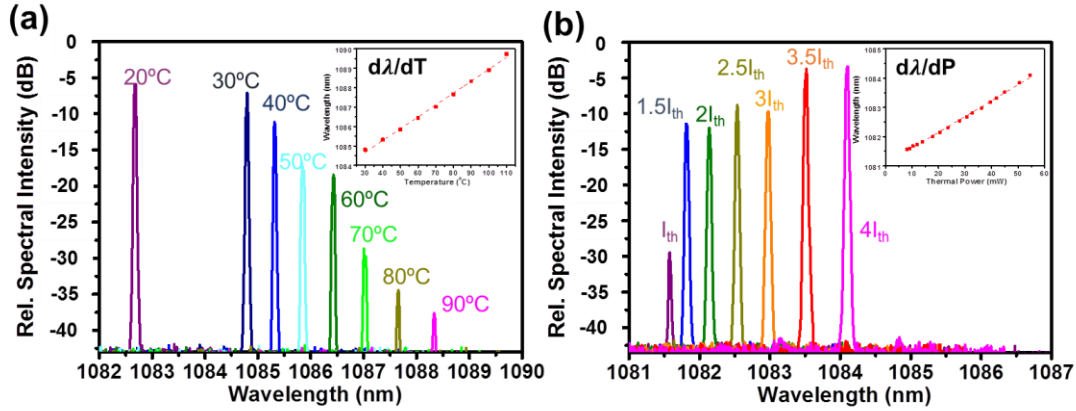
Figure 6.8 Characterization of thermal resistance. (a) Wavelength shift versus temperature (20-90 °C) under a bias current at $2I_{th}$, showing a fitted $d\lambda/dT$~0.054 nm/°C. **(b)** Wavelength shift versus injection current (I_{th}-$4I_{th}$) at 20 °C, multiplying with the corresponding voltage, a fitted wavelength shift versus dissipated thermal power $d\lambda/dP$~0.061 nm/mW is achieved. The calculated ratio of the above two gives a thermal resistance R_{th} of ~0.88 °C/mW.

6.4.3 Wavelength Tuning

Wavelength tuning of the HCG-VCSEL is realized through electrical actuation of the HCG MEMS structure. The HCG structure and the semiconductor layer beneath it form a parallel capacitive transducer. By reversely biasing the n-p junction between the tuning contact and laser contact, HCG MEMS moves downward thus reducing the optical cavity length. Continuous wavelength tuning of 20-nm towards the shorter wavelength is first obtained with 0-14.26 V of external applied voltage, shown in Figure 6.9 (a). The VCSEL stops lasing at 1064-nm under injection current of 2 mA due to gain or reflectivity falling below threshold. Above 15.57 V at 2 mA, the device starts lasing again with a higher order longitudinal mode around 1098-nm, and continuously tunes for another 14-nm over the applied voltage range of 15.57-17.8 V. The total tuning range through pure mechanical MEMS actuation is 34 nm. If we increase the injection current at the same time as tuning the voltage, thermal tuning could push the longer wavelength limit to 1104 nm. Thus, single-mode continuous tuning accounting for both mechanical and thermal approaches reaches 40 nm. The mechanical tuning range can be further increased if we pre-detune the center wavelength to the longer wavelength side of the whole tuning spectrum. The thermal tuning range here verifies that the gain and reflectivity are enough to support the whole 40-nm of mechanical tuning. Furthermore, the break in the middle of the tuning voltage range (14.26-15.57 V) is an artifact from designing the VCSEL epitaxy with the initial lasing wavelength at the center of the DBR and HCG bands. This can be corrected by changing the thickness of just one single layer, to realize continuous single longitudinal-mode tuning. In addition, the tuning voltage used here is relatively small compared with other MEMS structures in VCSEL [125], due to the light weight of our HCG structure. This allows for easy integration with low-voltage CMOS electronics for energy efficiency.

In order to investigate the limiting factor of the tuning range, RCWA method is used to simulate the reflectivity of the mirrors (including both the compound HCG mirror and bottom DBR mirror) versus tuning airgap and wavelength, as shown in Figure 6.9 (b). The resonance

wavelength of the corresponding cavity at each tuning step is also simulated and overlaid on top of the reflectivity contour. This simulation correlates with the measurement data in Figure 6.9 (a), and a theoretical tuning range of 50-nm is predicted for this HCG-VCSEL structure. We believe the red-shift of the starting center wavelength results from the extra strain in the QW region of the grown epitaxial wafer compared with design. This physical limit is determined by the free spectral range (FSR) between two longitudinal modes. Therefore, the wavelength tuning range can be further increased by improving the designs of cavity structure for wider FSR.
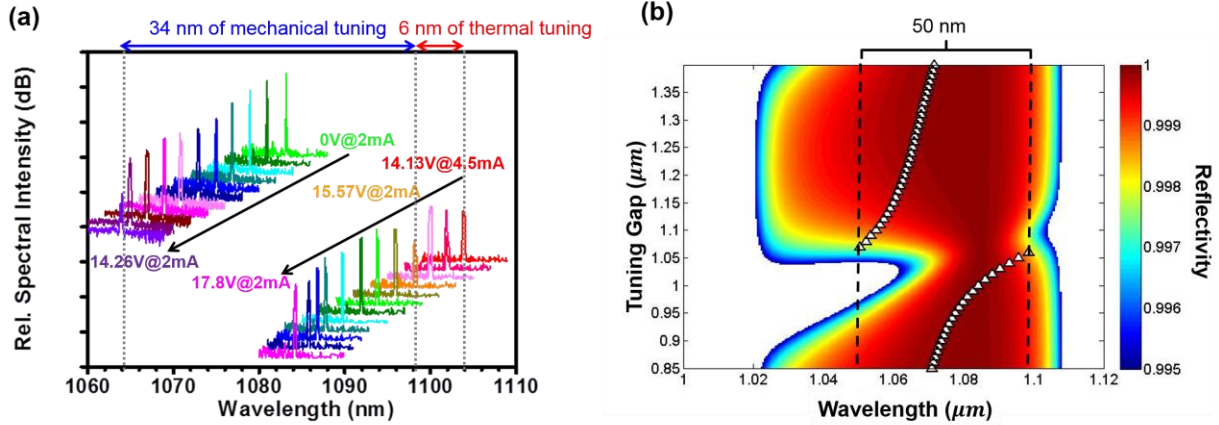
Figure 6.9 Wavelength tuning of the 1060-nm HCG VCSEL. (a) Single-mode continuous wavelength tuning of 40-nm, including 34-nm of mechanical tuning and 6-nm of thermal tuning. **(b)** Reflectivity contour of the reflection mirrors (including the top compound HCG mirror layers and the bottom DBR mirror) during tuning, with the resonance wavelength of the corresponding cavity indicated for each tuning airgap (triangular data points), showing a theoretical tuning range of 50-nm for this HCG-VCSEL structure.

When applying voltage to the tuning contact, the electrostatic force will reach an equilibrium balance with the elastic force from the MEMS spring. This will result in a new position of the HCG MEMS structure which is lower than the original position. This relation can be expressed by the following equation,

$$F_{electrostatic} - F_{elastic} = \frac{\epsilon A V^2}{2g^2} - k(g_0 - g) = 0 \quad (6.2)$$

where F is the tuning force and V is the tuning voltage, g_0 is the original tuning gap size (thickness of sacrificial layer) and g is the variable tuning gap, ϵ is the dielectric constant and A is the area of HCG capacitive plate. It can be calculated that the tuning gap size (g) follows approximately the power of 2/3 of the tuning voltage. And the theoretical maximum displacement of a capacitive transducer plate is 1/3 of the gap, which means after moving down by $1/3g$ (0.45 um in our case) the HCG MEMS will be clamped down. The wavelength versus tuning voltage for the first longitudinal mode measured in Figure 6.9 (a) is plotted in Figure 6.10. And the fitted relation is between V and λ is overlaid on top of the experimental data (red curve), which is generated utilizing equation (6.2) and calculation in Figure 6.9 (a). The well-matched trends prove that the HCG MEMS structure here indeed behaves like a micro-scale parallel capacitive transducer. The tuning efficiency (wavelength shift over tuning gap shift) is

approximately 0.06 nm/nm, which is mainly constraint by the large penetration depth into the DBRs. A larger tuning efficiency can be achieved by replacing the 2 pairs of top DBRs with an anti-reflection layer of equivalent optical thickness [119].
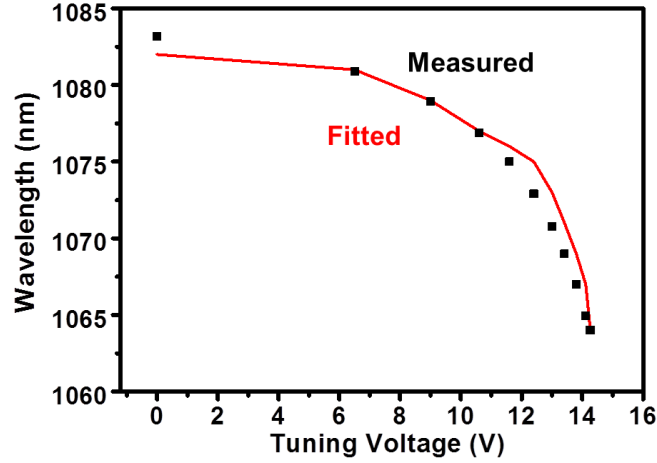
Figure 6.10 Lasing wavelength versus tuning voltage. The black dots are measurement data from Figure 6.9 (a), and the red curve is calculated with equation 6.2.

The wavelength tuning speed of the VCSEL is mainly determined by the resonance frequency of the MEMS structure. The frequency response of the mechanical tuning was measured and fitted with a harmonic oscillator model (Figure 6.11 (a)), yielding a 3-dB bandwidth of 1.15 MHz with a damped resonance frequency f_r~600 kHz. The Q-factor for the HCG MEMS is fitted to be around 1.5, mainly constraint by the air damping, the small spring constant, and the thick sacrificial layer. Using COMSOL, a finite element method (FEM) tool, the mechanical resonance is simulated to be ~541 kHz, very close to the measured value. While f_{-3dB}~1.15 MHz is already larger than the scanning rate requirement of most commercially available SS-OCT systems, it can be further improved. Because f_r is proportional to $\sqrt{k/m}$, where k is the spring constant and m is the mass of the MEMS structure, the ultralight weight HCG MEMS structure can potentially have 10 times faster tuning than its DBR counterpart. The spring constant k here is intentionally designed to be smaller for wider tuning range, and can be tailored to suit specific applications. We have indeed demonstrated tuning speed up to 100 MHz with a smaller HCG size and optimized spring constant [112].

73
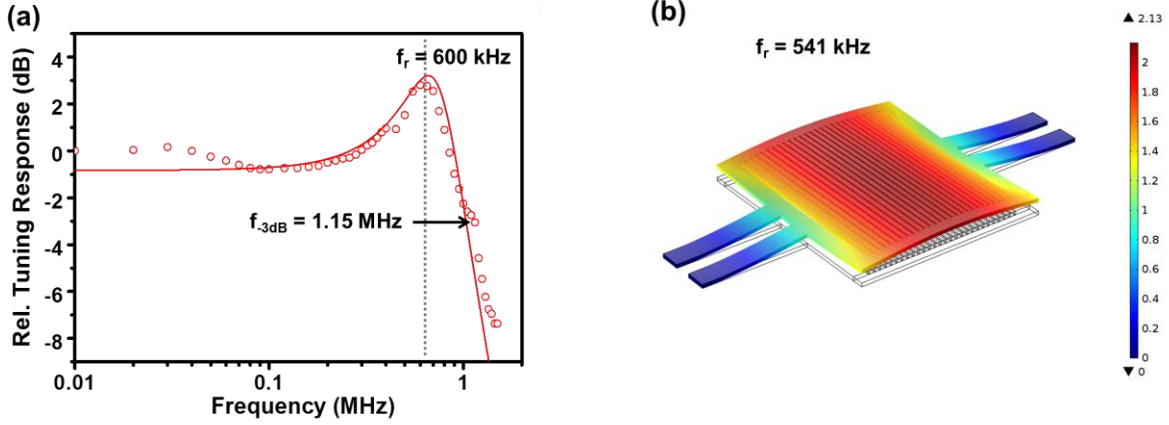
Figure 6.11 Tuning speed of the HCG MEMS. (a) Measured frequency response of the mechanical tuning, with a resonance frequency of 600 kHz and a 3-dB bandwidth of 1.15 MHz. The red circles are the measurement results and the red line is the fitted result with a harmonic oscillator model. **(b)** Tuning response of HCG MEMS simulated in COMSOL, showing a resonance frequency of 541 kHz.

6.4.4 Transverse Mode Control

As introduced above, the laser aperture definition for GaAs-based VCSELs generally utilizes the wet oxidation process which is highly selective to $Al_x GaAs$ with high Al-concentration. Although this technique is relatively mature in VCSEL fabrication industry with expensive in-situ supervision systems, it is yet extremely challenging to control under laboratory environment. Any fluctuation in the experimental conditions such as furnace temperature, vapor concentration, and gas flow, will greatly impact the yield and uniformity of VCSELs on a wafer scale. To obtain single transverse-mode VCSELs especially, an aperture of <5 μm is usually required, at which point oxidation rate increases with time exponentially [126]. Another degree of freedom to control transverse mode of VCSEL is therefore desired.

The size of HCG automatically poses a selective area of high-reflectivity on top of laser aperture. Furthermore, HCG is found to have reflectivity dependent on incidence angle (θ) [17]. Figure 6.12 illustrates the reflectivity contour (R>99.5%) of HCG airgap versus incidence angle, under a fixed HCG period (Λ~505 nm). Two designs are selected with distinct angle-dependent behavior. Design I with a~140 nm shows high reflectivity up to $\theta = 5°$, while the reflectivity of design II with a~105 nm is drastically reduced beyond $\theta = 1°$. Thus for design II, higher-order transverse modes emitting at a higher angle will be suppressed due to the reflectivity falling below threshold.
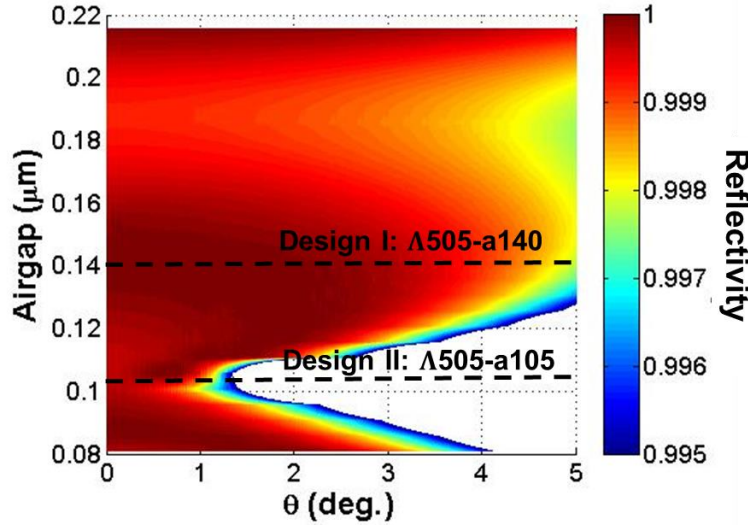
Figure 6.12 Reflectivity contour (R>99.5%) of HCG airgap versus incidence angle θ, of an HCG with period Λ~505 nm. While design I shows high reflectivity up to $\theta = 5°$, the reflectivity of design II drastically decreases above $\theta = 1°$.

The two designs above are fabricated into HCG-VCSEL devices with similar oxidation apertures. Figure 6.13 shows a comparison of the results, with (a) for design I (Λ~505 nm, a~140 nm) and (b) for design II (Λ~505 nm, a~105 nm). A Xerox IR camera was used to examine the aperture size right after wet oxidation, resulting in an aperture of around 20x20 μm^2 for both devices. We then measured the laser spectra of these devices with CW operation under a series of pump powers. As shown in Figure 6.13 (a-iii) and (b-iii), Device with HCG design I delivers multiple transverse modes for all pump levels, not surprisingly. However, device with HCG design II demonstrates a single transverse mode lasing, despite the large oxidation aperture. Thus it is validated that the angular-dependence of HCG can be used to efficiently control transverse modes of VCSEL and improve the yield of single-mode lasers. Similar results are demonstrated in [127]. This discovery is also very meaningful for pattern design of VCSEL emission, which will be discussed in details in Chapter 7.
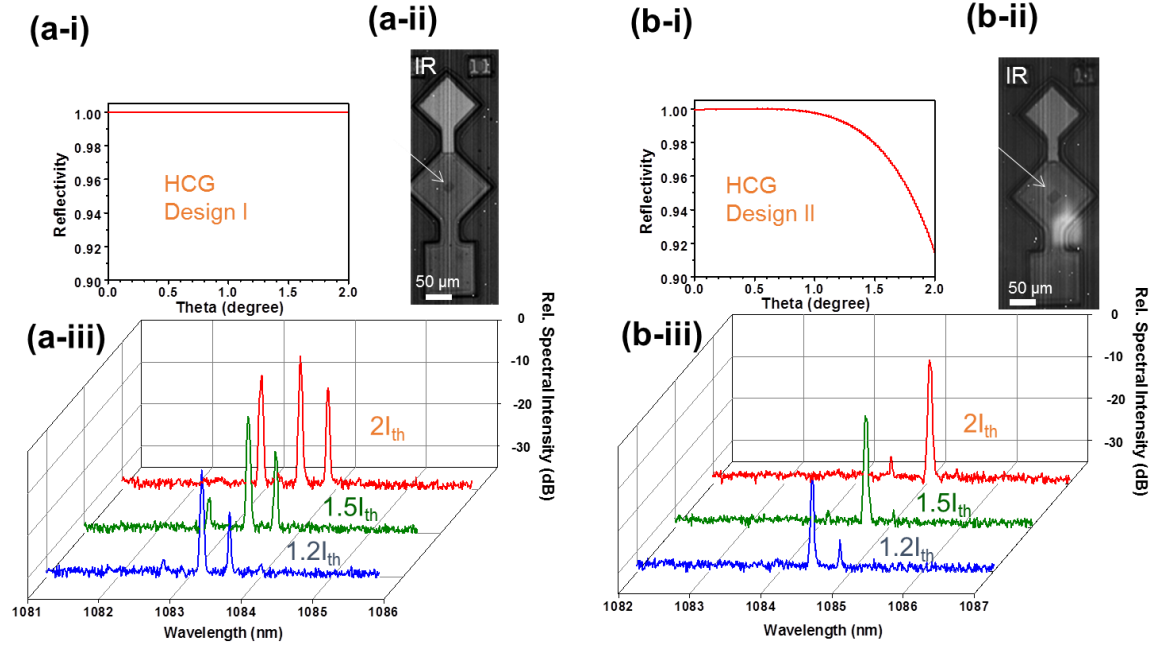
Figure 6.13 Angular-dependence of HCG reflectivity facilitates transverse mode control of VCSEL. Reflectivity versus angle (i), IR image of oxidation aperture (ii), and measured laser spectra under a series of injection currents (iii), for **(a)** HCG design I with Λ~505 nm and a~140 nm; and **(b)** HCG design II with Λ~505 nm and a~105 nm.

6.5 2D HCG-VCSEL

We have only investigated HCG designs with periodicity in 1D so far. In this section we explore the use of HCGs with 2D periodicity as tunable mirrors on the same 1060-nm VCSEL platform. The 2D HCGs not only can work as broadband high reflection mirror as well as 1D HCGs [128] [129], but also offer another degree of freedom to be designed into metasurfaces for light manipulation [130] [131]. Another potential that 2D-HCGs have is the polarization independence or multi-stability [128], which open up opportunities for multi-stable optical sources and all optical flip-flop operations with fast switching time and low switching energy [132]. Here we demonstrate the first (to the best of our knowledge) electrically-pumped tunable VCSEL using 2D-HCGs as the tuning mirror.

The 2D-HCG here is designed as mesh-type, where periodic air holes are etched through the high-index membrane. This is in contrast to the island-type 2D-HCGs [129] with high-index elements surrounded by low-index material, which is impossible to be fully suspended as a tunable MEMS mirror. However, without the high-index structures completely surrounded by low-index materials, the mesh-type 2D-HCGs are more challenging to design. The optical field tends to strongly couple across the unit cells through the connected high-index structures, making it difficult for the selection of manageable number of dominant modes and the engineering of interferences among them. Therefore, in order for the mesh-type 2D-HCG to function as desired for VCSELs, careful design with complete understanding of the high reflectivity mechanism is critical.

We use our in-home developed rigorous coupled-wave analysis (RCWA) package [131] for efficient and accurate simulations of 2D-HCGs. To narrow down our search of parameters and understand the optical behavior of the mesh-type grating, we first regard the grating as infinitely-long $\hat{z}$-invariant coupled waveguides. Here, we use grating periods $\Lambda_x = \Lambda_y = 750$ nm, and the air gaps are $A_x = 550$ nm and $A_y = 500$ nm. We are able to identify three most fundamental eigenmodes based on their polarization (E_x/H_y-dominant) and symmetry. These eigenmodes are solved numerically in Fourier domain using the Floquet mode expansion, and used to express the transverse electric field in the coupled waveguide. Figure 6.14 shows the reflectivity contour calculated by RCWA as a function of the incidence wavelength and the grating thickness under normal incidence condition. We observe a "checkerboard" pattern similar to that for 1D-HCG, except adding a set of narrow resonance lines. When overlaying on top the calculation results from the tri-mode round-trip phase conditions, they overlap perfectly. This proves that our tri-mode resonance theory can explain the optical behavior in 2D mesh-type HCGs, and can greatly facilitate our design of ultrahigh reflection HCG mirrors.
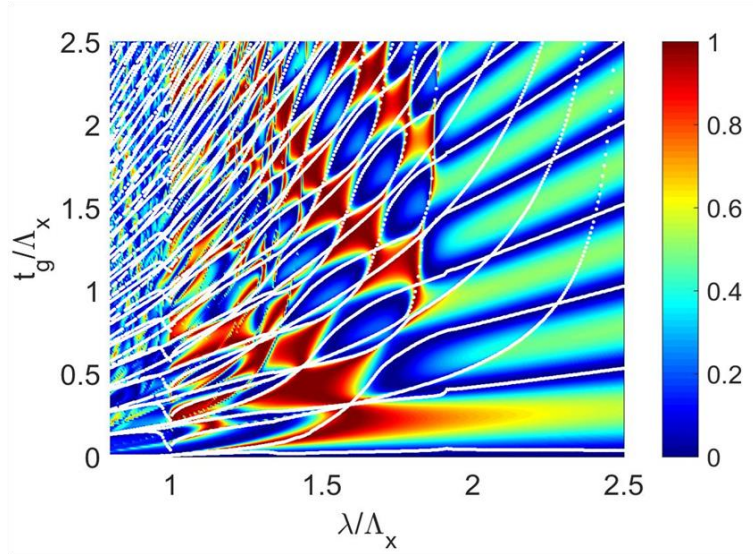
Figure 6.14 Reflectivity contour calculated from RCWA of thickness (t_g) versus wavelength (λ), both normalized by HCG period (Λ). The resonance lines are calculated from the tri-mode round-trip phase conditions are overlaid on top and show a perfect agreement.

The 2D-HCG is fabricated on the same VCSEL platform as the 1D-HCG VCSEL above. The ebeam lithography and RIE dry etching are adjusted to obtain the most calibrated HCG mesh dimensions. The SEM image of a fully suspended 2D-HCG MEMS is shown in Figure 6.15 (a). The LIV characteristics of the laser are plotted in Figure 6.15 (b), where a lasing threshold of 1.75 mA and an output power of 0.68 mW are seen. The images captured before and after lasing are inset, with speckle patterns observed above lasing threshold. The laser operates at single mode under CW electrical injection up to 75 °C on a TEC-controlled copper chuck.
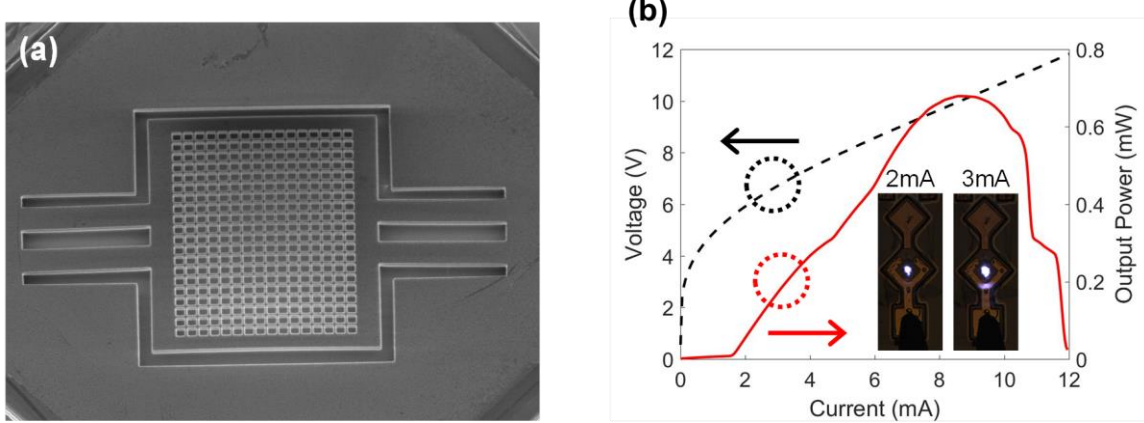
Figure 6.15 2D-HCG VCSEL fabricated on the 1060-nm epitaxial wafer. (a) SEM image of a suspended 2D mesh-type HCG surrounded by air. **(b)** LIV characteristics of the 2D-HCG VCSEL, showing a threshold current of 1.75 mA and output power of 0.68 mW. The inset images show the captured VCSEL emission from the top surface.

The total tuning range of 4.5 nm is demonstrated in Figure 6.16 (a), including 1.6-nm of electrostatic MEMS tuning by applying external voltage up to 17 V at 5mA, and 2.9-nm of thermal tuning by increasing injection current from 5 mA to 8 mA at zero tuning voltage. Though the tunability is not yet comparable to that of 1D-HCG VCSEL, this first demonstration of a tunable 2D-HCG VCSEL is still very meaningful for some applications. The tuning range limitation in this initial demonstration is unlikely due to the high reflectivity bandwidth of the 2D-HCG design, which is verified to be over 100 nm for R>99.5%. Figure 6.16 (b) shows the reflectivity contour during wavelength tuning calculated with RCWA method with the resonance wavelengths overlaid on top. The FSR-limited VCSEL tuning range with a polarization-dependent 2D-HCG design ($\Lambda_x = \Lambda_y = 750$ nm, $a_x = 550$ nm, and $a_y = 500$ nm) is simulated to be 42 nm, which is very close to that of the 1D-HCG design in Figure 6.9 (b). Therefore, we believe the cause of a compromised tuning range here is related to the MEMS mechanical properties. Combining the results from Figure 6.16 (a) and (b), (λ vs. V) and (λ vs. g) respectively, we can extract the equivalent MEMS spring constant from the electrostatic force equation [133] which results in 7.15 N/m. This indicates the 2D-HCG MEMS structure is stiffer than what we normally see in 1D-HCG MEMS.
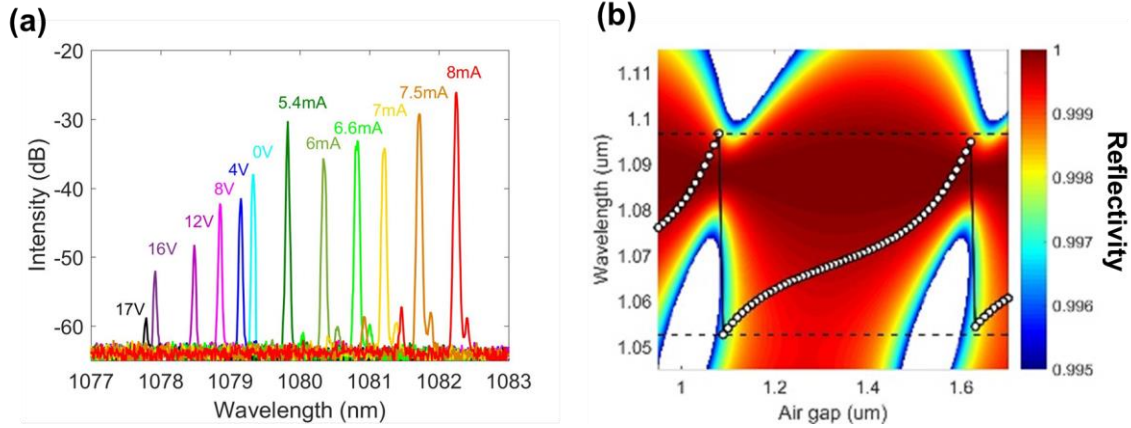
Figure 6.16 Wavelength tuning of 2D-HCG VCSEL. (a) Spectra showing a total tuning range of 4.5 nm, including 1.6-nm of electrostatic MEMS tuning (tuning voltage 0-17 V at current of 5 mA) and 2.9-nm of thermal tuning (injection current 5-8 mA at zero tuning voltage). **(b)** Reflectivity contour of compound HCG mirror during wavelength tuning with the resonance wavelengths at each tuning gap overlaid, showing a theoretical tuning limit of 42 nm.

6.6 Summary

To summarize this chapter, we have demonstrated a widely and fast tunable 1060-nm VCSEL enabled by HCG as an integrated tuning mirror. The 1D-HCG VCSELs show single mode emission at CW electrical operation. The lowest threshold current obtained is ~100 µA, and the output power can go beyond 1.3 mW. The laser provides excellent thermal characteristics which can still lase when the temperature rises above 110 °C. Utilizing the temperature-dependent and power-dependent spectra, the thermal resistance is calculated to be 0.88 °C/mW, outperforming other VCSEL structures with even larger laser apertures. The wavelength can be tuned through electrostatic actuation of the HCG MEMS structure, which behaves like a capacitive transducer plate. A total tuning range of 40 nm is obtained, including 34-nm of MEMS tuning and 6-nm of thermal tuning. A theoretical tuning limit of 50-nm results from the simulation and can be improved by designing the epitaxial layer structure to obtain wider FSR. Although optimized for wider tuning range rather than fast tuning speed, a 3-dB bandwidth of 1.15 MHz can still be obtained from the MEMS mechanical response measurement, which is sufficient for SS-OCT application. In addition, transverse-mode control is realized utilizing the angular-dependence of HCG reflectivity. This saves VCSELs from the traditionally challenging wet oxidation process, and improves the yield of single-mode lasers even on top of large laser apertures. Comparing with the other available 1060-nm tunable VCSELs, our work here demonstrates considerably wide tuning range and fast tuning speed, and most importantly shows the ease of fabrication with high yield at low cost. This shows promise for commercialization in applications such as short-link optical communication, SS-OCT, and LIDAR.

We also present the design rule for 2D-HCGs as broadband reflector for tunable VCSELs. With our tri-mode analysis we successfully explain the mechanism of ultrahigh reflection in 2D mesh-type HCGs, which agrees very well with the results from RCWA. We have fabricated the 2D-HCGs on the same 1060-nm epitaxial platform as the 1D-HCGs, and obtained some preliminary results. The devices also show single-mode lasing at CW operation, with output

power exceeding 0.68 mW. The MEMS tuning range reaches only 1.6 nm although the simulation shows a promising number of 42 nm. We believe this is caused by the much stiffer HCG MEMS structure, compared with the 1D-HCG. Yet the first demonstration of a tunable 2D-HCG VCSEL still shows promise for integrated metasurfaces aiming at direct light manipulation, multi-stable optical sources, and all optical flip-flop operations with fast switching time and low switching energy.

Chapter 7
HCG as Integrated Beam-Shaping Element for VCSEL

Vertical-cavity surface-emitting lasers (VCSELs) are key light sources in optical communications, with the advantages of low power consumption, low packaging cost, and ease of fabrication into arrays for wafer scale testing. The key advantage of VCSEL is built in nature – the vertical emission from the top surface. This not only optimizes the laser beam shape, but also greatly improves the coupling efficiency into fiber, grating couplers, and so on. It also opens up the opportunities for direct beam shaping with integrated optical elements, such as collimator, deflector, splitter, wave plates, planar lens, vortex beam generator, etc. The two most recent publications [134], [135] both realized vortex beam emission from VCSEL, by performing an extra step of fabrication on top of a finished VCSEL device. However, the difficulty of this method lies in the complicated fabrication process involving lithography and etching of 3D structure or non-straight lines. The coupling of the beam from the top of the finished VCSEL device with the optical element overlaid on top makes it even more challenging. In this chapter, we will introduce how high-contrast grating (HCG) can help solve these problems in a monolithic way.

7.1 InP-based Proton-Implanted HCG-VCSEL

Long-wavelength VCSELs (emitting in the 1.3-1.6 µm regime) are highly desirable for the rising applications of data and computer communications, optical access networks, and optical interconnects [10] , [116]. Additionally, mode-hop-free, fast and widely tunable VCSELs are a perfect candidate for optical coherent tomography (OCT) and light ranging applications (LIDAR) [14]. A single-mode, high-speed, tunable VCSEL emitting at 1550-nm has been previously reported, incorporating a high-contrast grating (HCG) metastructure as the top mirror [10] ,[116].

The VCSELs we fabricated in this paper are with bottom DBRs and a top HCG as reflective mirrors respectively. We used as-grown 1550-nm epitaxial wafer consisting of 40-55 pairs of bottom DBRs, multiple quantum wells in the active region, tunnel junction, sacrificial layer, HCG layer made of high-refractive-index material (InP), and top contact layer. The current aperture is designed to be <20 µm, ensuring the laser oscillation in single fundamental transverse mode. Details of the laser structure, fabrication process, and laser performance can be found in [10], [116]. The study here involves both TE and TM mode HCG-VCSELs [15]. Figure 7.1(a) shows the scanning electron microscopy (SEM) image of a typical TE HCG-VCSEL device, with a zoomed-in perspective of the fully suspended HCG mirror surrounded by air. The HCGs we fabricated have grating bar period of 1.05-1.11 µm and spacing of 0.4-0.84 µm for TE mode. This endues HCGs with the degrees of freedom to manipulate output properties while maintaining single-mode lasing. Figure 7.1(b) exemplifies a lasing spectrum at 15 ºC, with side mode suppression ratio of 45 dB. Single mode emission is demonstrated up to 85 ºC, with output power reaching 2.4 mW at 15 ºC under continuous-wave (CW) operation. In addition, the HCG-VCSEL was shown to have a total linewidth of 60 MHz and a coherent length of 5 m in air, and an intrinsic linewidth <20 MHz. Transmission of directly modulated 10 Gbps over 100-km dispersion-compensated single-mode fiber is demonstrated. Tunable HCG-VCSEL is also realized with the HCG integrated with a micro-electro-mechanical structure (MEMS). Continuous wavelength tuning as wide as 26.3 nm is achieved. The tunable VCSEL was used as

81

a source for external modulation for 40-Gbps differential-phase-shift-keyed signal and transmitted over 100-km dispersion-compensated link with negligible power penalty.

Different from GaAs-based VCSELs introduced in Chapter 6, the InP-based epitaxial materials are not endued with a layer like $Al_{0.98}GaAs$ which can be conveniently wet oxidized with high selectivity. Therefore, a planar and monolithic process of proton implant is used to provide current confinement, which was made possible because of the relatively thin thicknesses of the HCG and sacrificial layer on the top. Additionally, a tunnel junction is used to minimize the amount of p-type materials, thus reducing the free carrier absorption and electrical resistance. The wafer-scale proton implant process shares the same lithography mask, thus the aperture sizes are very uniform among the VCSEL devices. This reduces the degree of complexity in the study of beam-shaping characteristics, and is the main reason that we chose proton-implanted InP-based VCSEL over oxidized GaAs-based VCSEL as a platform here.
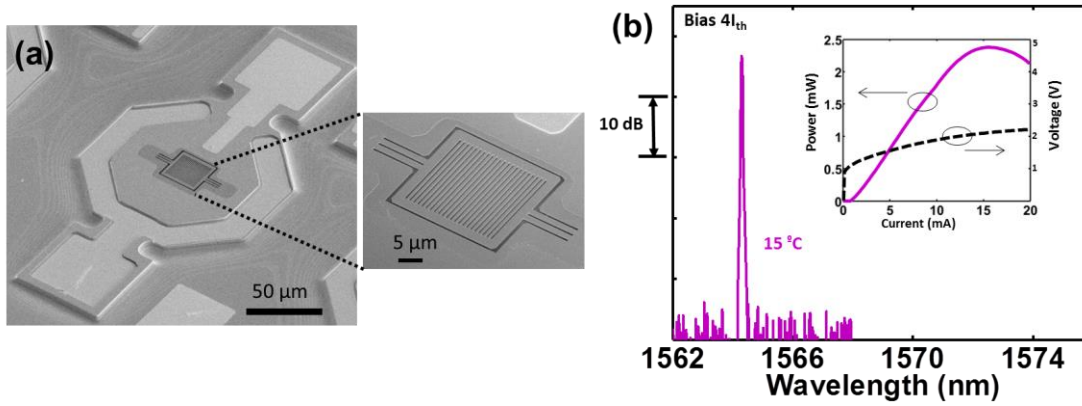
Figure 7.1 InP-based HCG-VCSEL emitting at around 1550 nm. (a) SEM image of a typical TE HCG-VCSEL device, with a zoomed-in view of the fully suspended HCG surrounded by air. **(b)** Spectrum and LIV characteristics of a typical TE HCG-VCSEL at 15 ℃, showing a single mode emission with side-mode suppression ratio of 45 dB, and output power of ~ 2.4 mW.

7.2 Manipulation of VCSEL Far-field Distribution with HCG

Besides the broadband high reflectivity, HCG offers various other unique characteristics such as wave-front phase engineering. Back in 2010, the paper by Lu et al. [12] led the trend of designing planar lens with optical phase elements [136]- [138]. The paper described how the phase distribution of a Fresnel lens can be mapped on the reflection or transmisison phase of HCG bars with different design parameters. After arranging the HCG bars of the picked dimensions in the spatial domain, a planar lens with high focusing power can be designed. The methodology was then extended to 2D sub-wavelength grating lenses and experimentally demonstrated with polarization-independent operation [139].

If we are to integrate the planar HCG lens with an active light source, in a VCSEL environment for instance, light emitted from the laser aperture is Gaussian shape instead of plane wave as in [12]. The light interaction with a finite-size HCG also distinguishes from that with an

infinite HCG [140], [141]. When the HCG dimensions are chirped spatially, each wave-front will encounter different transmission phases as indicated in Figure 7.2 (a). The information is then carried on and gets expressed in the far-field light intensity captured by camera. This is called spatial modulation of HCG transmission phase $\Phi_T(x, y)$, because HCG bars with dimensions chirped in the spatial domain are used for manipulating the phase of light. We then find that under Fresnel condition, the far-field (electric field) can be approximated as the Fourier transform of the near-field (electric field). Then when the Fourier transform is performed upon a Gaussian beam in spatial domain, in Fourier domain it is equivalent to decomposing the Gaussian beam into a series of plane waves at different incident angles. Thus far-field pattern is a representation of the angular information of the beam in the near field. Inspired by this explanation, if we keep the HCG dimensions uniform (not chirped) in the spatial domain, instead we filter the intensity of the beam in the angular domain after Fourier transform, we can also manipulate the light characteristics captured by camera. We name this method as angular modulation of HCG transmission intensity $I_T(k_x, k_y)$ as illustrated in Figure 7.2 (b), which keeps uniform HCG bars while exploring the angular dependence of its transmission intensity in the Fourier domain.
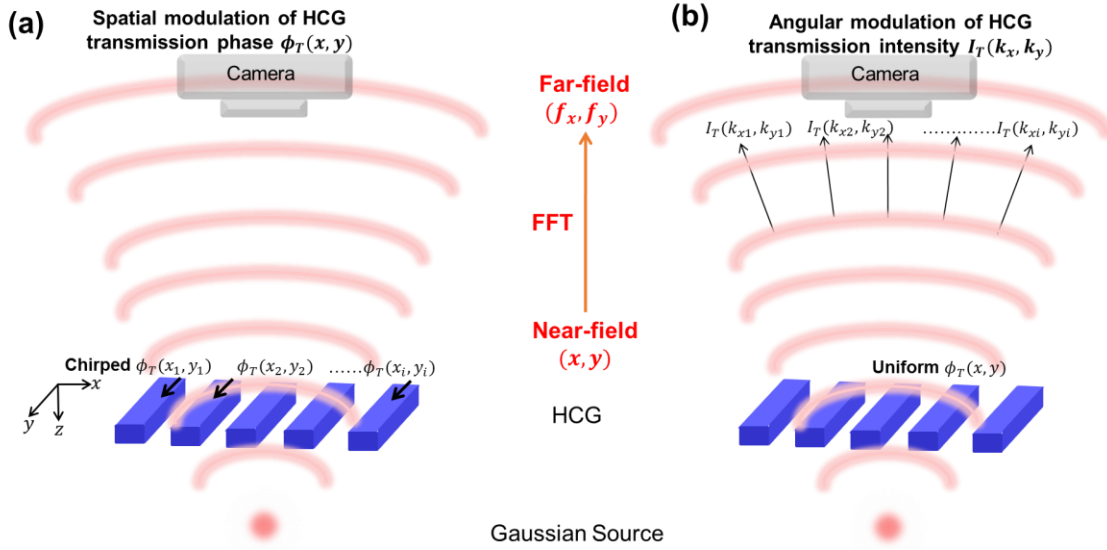
Figure 7.2 Comparison of two methods for far-field light manipulation. (a) Spatial modulation of HCG transmission phase $\Phi_T(x, y)$ by chirping the HCG dimensions in the near-field. **(b)** Angular modulation of HCG transmission intensity $I_T(k_x, k_y)$ by filtering the angular intensities in the far-field.

7.3 Angular Modulation of HCG Transmission Amplitude

Based on the hypothesis above, for a HCG design with chirped dimensions to perform light manipulation in the far-field, it must have angular-dependence characteristics of transmission intensity. It turns out some HCG designs do present very unique transmission characteristics, when the light is incident at an angle of θ other than surface-normal [105]. The HCG we study here are InP-based at 1550 nm, whose schematics are shown in Figure 7.3 (a). The dimensions of

HCG cover a wide range for both TE-polarization (t_g=195 nm, Λ = 1050~1110 nm, a = 420~840 nm) and TM-polarization modes (t_g=410 nm, Λ = 700-770 nm, a = 180-300 nm). The transmission of the HCG with Λ=1080 nm and varying airgap sizes (a) versus increasing incidence angle ($\theta = 0° - 20°$) is plotted in Figure 7.3 (b), showing the regions where T<0.05% thus R>99.5% to qualify for lasing condition. The transmission intensity versus θ for three different airgaps is then extracted for comparison. For design I with a=490 nm, the transmission decreases with incidence angle, while design II with a=650 nm has transmission increasing instead. Yet for design III, the transmission increases first then decreases with incidence angle, and vice versa for reflection. This fascinating characteristic has intrigued us to manipulate far-field emission pattern of VCSEL emission, which will be explained in the next section.
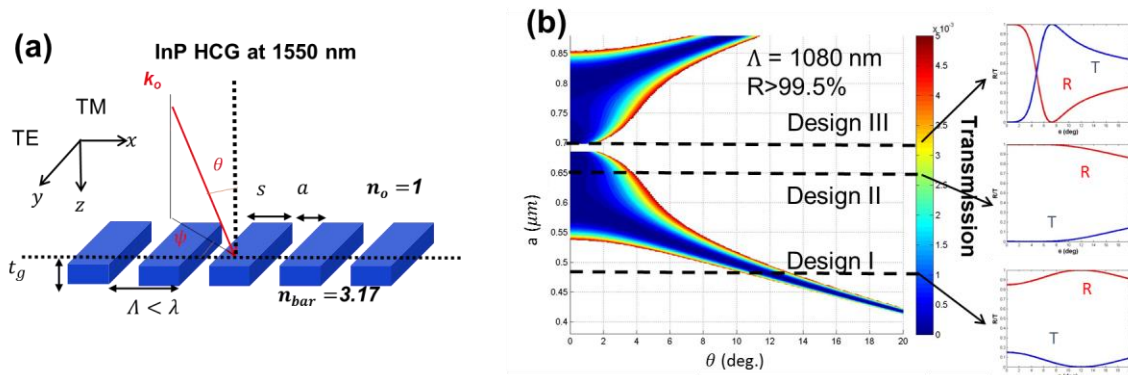
Figure 7.3 Angular dependence of HCG transmission. (a) Schematics of the HCG platform used in this study, InP-based HCG targeting at **λ**~1550 nm with oblique incidence angle **θ**. **(b)** Transmission of HCG with **Λ**=1080 nm for with varying airgaps under different airgap **θ**, highlighting three designs with distinct angle-dependent transmission / reflection characteristics.

Figure 7.4 illustrates how the angular dependence of HCG transmission amplitude is translated into the distribution of far-field intensities. The Gaussian beam generated by VCSEL laser aperture propagates from the near-field to the far-field. The HCG dimensions are uniform thus the transmission phase applied to the wave-fronts of the Gaussian beam is the same. In far-field, the Fourier transform of the Gaussian beam G (x,y) still remains as Gaussian shape denoted as G (k_x, k_y), which can be regarded as a decomposition into plane waves at different incidence angles (θ_i, ϕ_j) related to (k_{xi}, k_{yj}). If the transmission intensity of HCG is uniform across all incidence angles, then the Gaussian beam will not be influenced. However, if the transmission intensity of one particular HCG design has strong transmission variance across the range of incidence angles, such an intensity filtering factor $I_T(k_{xi}, k_{yj})$ will be superimposed upon the angular component G (k_{xi}, k_{yj}) thus to modulate the beam shape. The case in Figure 7.4 exemplifies an HCG design whose transmission intensity increases with incidence angle θ, resulting in a far-field pattern with intensity on the sides higher than the center - double lobes.
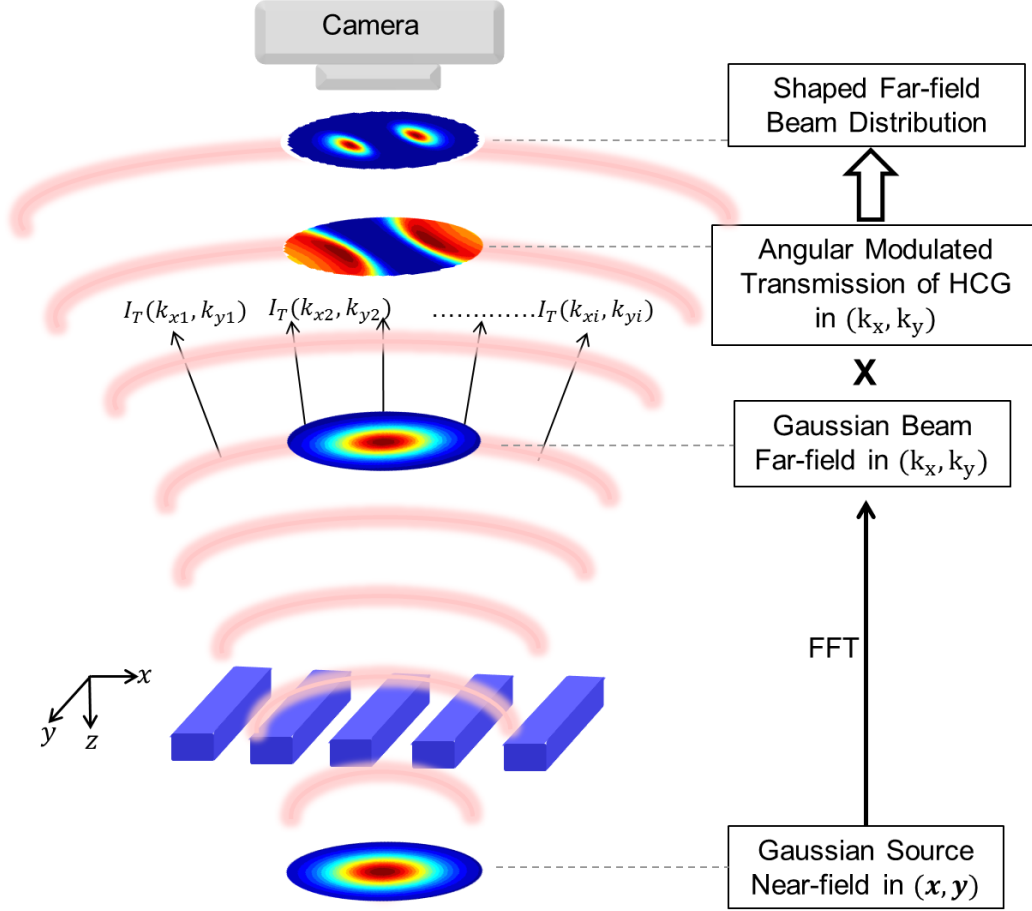
Figure 7.4 The schematic process of far-field emission pattern manipulation with HCG as a transmission angular modulation plate. The case exemplifies here shows an HCG with transmission intensity increasing with incidence angle, thus yielding a double-lobe far-field pattern instead of Gaussian shape.

The far-field manipulation of three HCG designs (i, ii, and iii) are illustrated in Figure 7.5. Plots in Figures 7.5 (a) show the original transmission distributions of three HCG designs versus incidence angles θ and ϕ, where θ is the angle between incidence beam and z-axis (propagation direction) and ϕ is the angle between incidence plane and x-axis (HCG periodicity direction) as indicated in Figure 7.3 (a). These are simulated with G-solver, a rigorous coupled-wave analysis (RCWA) tool. The transmission distribution is then converted from the angle domain (θ, ϕ) to Fourier domain (k_x, k_y) through the relations $k_x = k \cdot sin\theta \cdot cos\phi$ and $k_y = k \cdot sin\theta \cdot sin\phi$, where k is the wave vector. The results are displayed in Figure 7.5 (b). When these angular-dependent transmission distributions are superimposed on top of the Gaussian beam in Fourier domain (k_x, k_y), the resulting far-field distribution patterns are shown in Figure 7.5 (c) correspondingly. They lead to Gaussian, double-lobe, triple-lobe patterns in Figures 7.5 (c-i), (c-ii), and (c-iii), respectively.
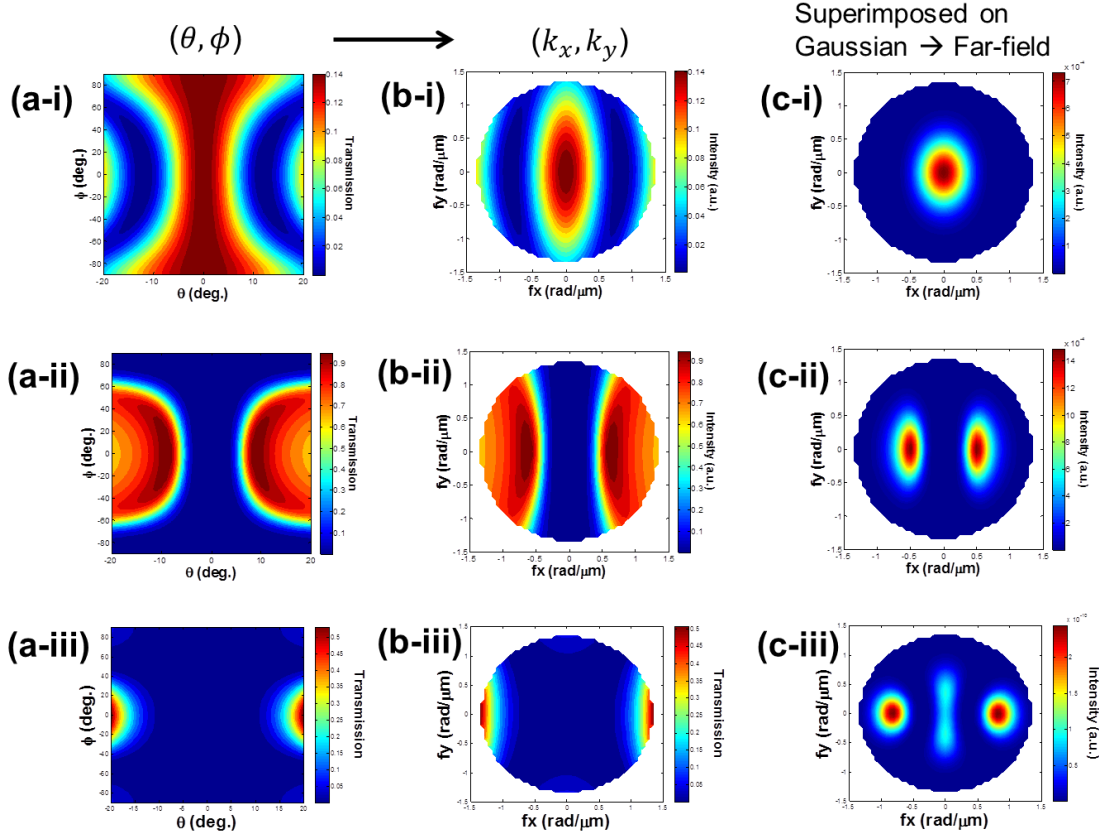
Figure 7.5 The method of calculating far-field emission distribution for three HCG designs. (a) Transmission intensity versus incidence angles (θ, ϕ) for HCG designs i, ii, iii. **(b)** Transmission intensity distribution converted into Fourier domain (k_x, k_y) for HCG designs i, ii, iii. **(c)** After superimposing (b) with Gaussian beam in Fourier domain, the resulting far-field distribution patterns for HCG designs i, ii, iii.

We applied this theory to analytically calculate the far-field patterns of different HCG designs. A wide range of HCG dimensions are fabricated for both TE and TM polarization modes, with a large degree of freedom. The measured far-field patterns all match well with the designs. Independently, we performed 3D finite-difference time-domain (FDTD) simulation to obtain the far-field patterns. The results are in excellent agreement with the analytically calculated and experimentally measured ones. Four examples are shown in Figure 7.6, with the rows (a), (b), (c) as the designed (with the analytical method above), measured (from fabricated devices), and simulated (with 3D FDTD tool) respectively. The examples show four different designs whose dimensions are labeled in the figures, where (i) and (ii) are TE-mode while (iii) and (iv) are TM-mode HCG. Depending on different HCG designs, the resulting far-field patterns shown are Gaussian, double-lobe, triple-lobe, and bow-tie shapes. It is worth noting that for both TE and TM mode epitaxial wafers, Gaussian beam outputs can be realized with large fabrication tolerance.
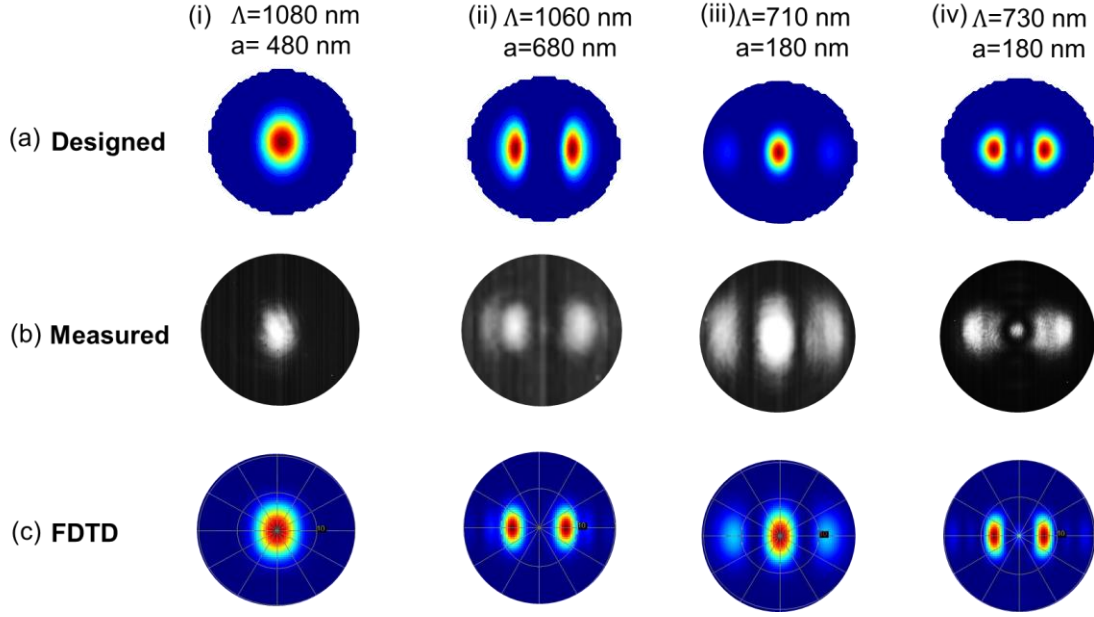
Figure 7.6 Far-field patterns for four HCG designs (i), (ii), (iii), and (iv). (a) Calculated far-field distributions with the analytical method in Figure 7.5. **(b)** Measured far-field distributions from fabricated HCG-VCSEL devices based on the designed parameters. **(c)** Simulated far-field distributions with 3D FDTD tool, showing great agreement with the designed and measured patterns.

In addition, the light manipulation is only effective in the x-axis here where the HCG periodicity occurs. We believe similar theory can be generalized to 2D HCG design that will provide another degree of freedom in beam shaping functionalities. However, for the 1D HCGs explored here, we also observed strong beam shaping in the y-direction for some HCG designs. We believe this is caused by the asymmetric laser apertures due to the imperfection of the proton implant process. Figure 7.7 shows the analytical calculated far-field patterns for a TE-HCG design (Λ=1080 nm, a = 840 nm) with varying aperture diameters in x and y directions. The pattern in the center ($A_x = A_y = 8$ μm) is the standard size we use for fabrication, when the aperture turns out to be perfectly round as designed. However, for apertures with $A_x \neq A_y$, the generated Gaussian beams will be elliptical. Although the HCG does not have strong angular dependence in the y-direction (parallel to HCG bars) due to lack of periodicity, reduced aperture size A_y can increase the divergence angle thus to enhance the angle-dependent effect in the y-direction. Therefore, interesting far-field patterns in the y-direction can be observed for the cases where $A_y < A_x$. This inspiring mechanism matches with some of the measured far-field patterns with features in the y-direction, and can be further utilized to increase the degree of freedom for beam shaping purposes.
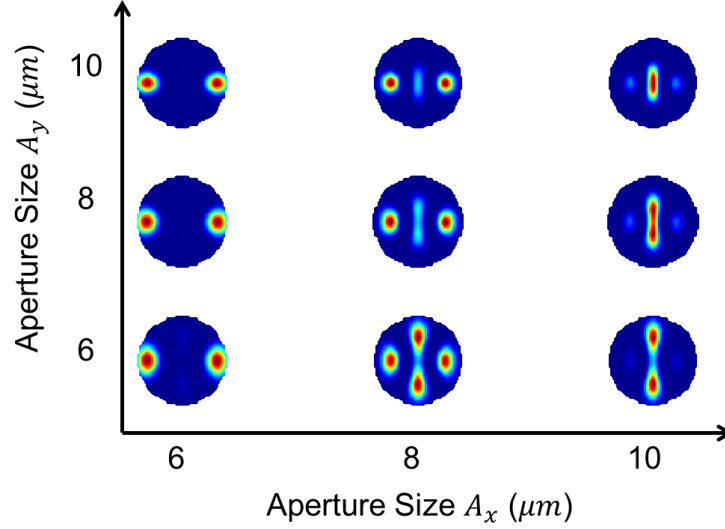
Figure 7.7 Analytically calculated far-field patterns for a TE-HCG design **Λ**=1080 nm and a=840 nm, with the aperture diameters in both x and y directions varying between 6, 8, and 10 **µm**. Enhanced angular dependence in y-direction for $\mathbf{A_y} < \mathbf{A_x}$ is expressed as interesting patterns.

7.4 Potential Applications for HCG-VCSEL Beam-Shaping

It is worth noting that all the HCG-VCSELs demonstrated here are with single-mode lasing, which is usually in Gaussian shape. With the transmission characteristics varying with emission angles, the HCG can act as a transmission modulation plate while being a high-reflection mirror to support lasing. As illustrated in Figure 7.8, we can then fabricate HCG-VCSEL arrays with various far-field patterns including but not limited to single-lobe, double-lobe, triple-lobe, "bow-tie", "sugar cone", "donut" shapes, etc. This opens new revenue for applications requiring flexible laser beam shapes from the same integrated optoelectronics chip.
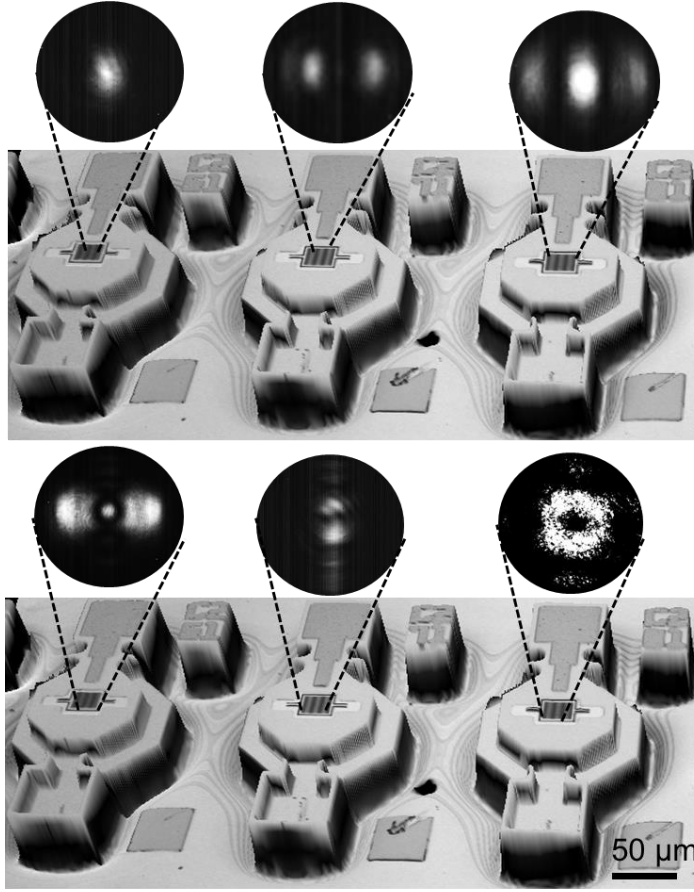
Figure 7.8 HCG-VCSEL arrays emitting at single-mode yet with various far-field emission patterns including single-lobe, double-lobe, triple-lobe, bow-tie, sugar cone, donut shapes. The device image is taken with 3D confocal optical microscope, and the far-field patterns are captured with Xerox IR camera.

Furthermore, while the front-surface emission of HCG-VCSEL is manipulated by a large variety of HCG designs, the back-surface beam always remains as Gaussian shaping by going through the bottom DBR mirror. This is experimentally verified by thinning down the wafer substrate and collecting laser emission from the backside. A two-face single-mode laser is then born as introduced in Figure 7.8, generating bidirectional dual laser beams to double the functionalities.
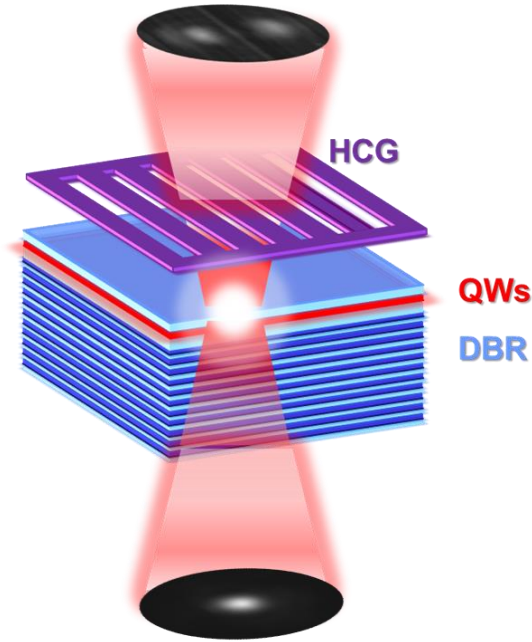
Figure 7.9 A double-face single-mode laser, with front-surface beam shape manipulated by HCG designs while back-side beam remains as Gaussian shape.

In the future, we would like to combine the phase engineering mentioned in Figure 7.2 and reported in [12] with the angular modulation of HCG introduced here, to realize a variety of beam shaping configurations fully integrated with active VCSEL source. The HCG functions both as an integrated tuning mirror to support lasing, and as an integrated optical element for beam shaping functions. Figure 7.10 lists some of the potential functions, where the HCG-VCSEL will be able to collimate, focus, deflect, split, and even reshape the light into any desired patterns. We believe such versatile lasers integrated on a compact chip will be promising in the fields of laser transverse mode control (as introduced in section 6.4.4), efficient light coupling, particle trapping, cell manipulation, and much more beyond.
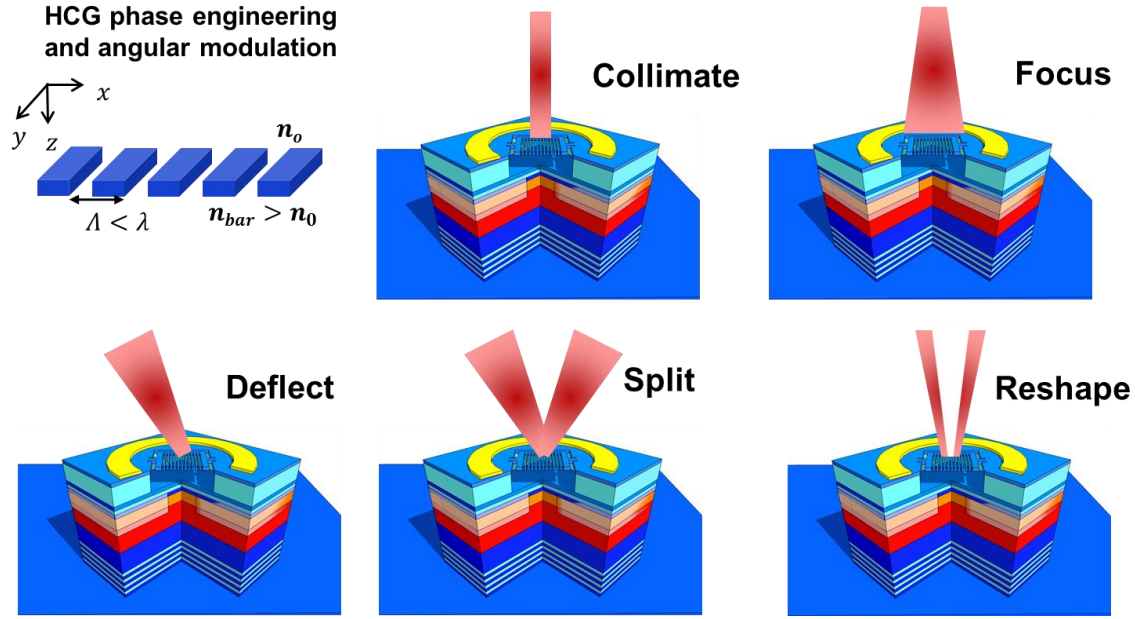
Figure 7.10 InP-based HCG-VCSEL emitting at around 1550 nm. (a) SEM image of a typical TE HCG-VCSEL device, with a zoomed-in view of the fully suspended HCG surrounded by air. **(b)** Spectrum and LIV characteristics of a typical TE HCG-VCSEL at 15 ℃, showing a single mode emission with side-mode suppression ratio of 45 dB, and output power of ~ 2.4 mW.

7.5 Spatial Modulation of HCG Transmission Phase

In order to combine the spatial modulation of transmission phase with the angular modulation of transmission intensity introduced above, a preliminary study of HCG transmission phase (ϕ_T) is conducted here. Different from the design of a passive element in ref. [12], the design of an active HCG here integrated with VCSEL is constraint due to its dual roles – high reflection mirror and transmission modulation plate. Fabrication feasibility also needs to be taken into account on a VCSEL platform. Therefore, if we are to spatially chirp the HCG dimensions, the range of reflection phase that the selected HCG bars cover is not able to vary much in order to satisfy the round-trip condition for lasing. But to achieve most flexibility of beam shaping, the range of transmission phase needs to be big enough. This is a challenging task, because the reflection phase (ϕ_R) and transmission phase (ϕ_T) are related. Taking a TE-mode HCG with thickness T_g=195 nm for instance, the reflectivity and transmission contour plots are shown in Figure 7.11 (a) and (b), respectively. The reflection phase contour versus HCG period and airgap is also calculated in Figure 7.11 (c) with our home-built HCG Solver [121], providing only <0.2π variation in the HCG dimension range with high reflectivity. However, it is found that the HCG transmission phase (Figure 7.11 (d)) shows an interesting π phase jump in the middle of the contour plot, matching the 100% reflectivity line in Figure 7.11 (a). This unique property greatly broadens the transmission phase that this range of HCG dimensions can cover. This is good news for beam-shaping utilizing the chirped HCG transmission phase.
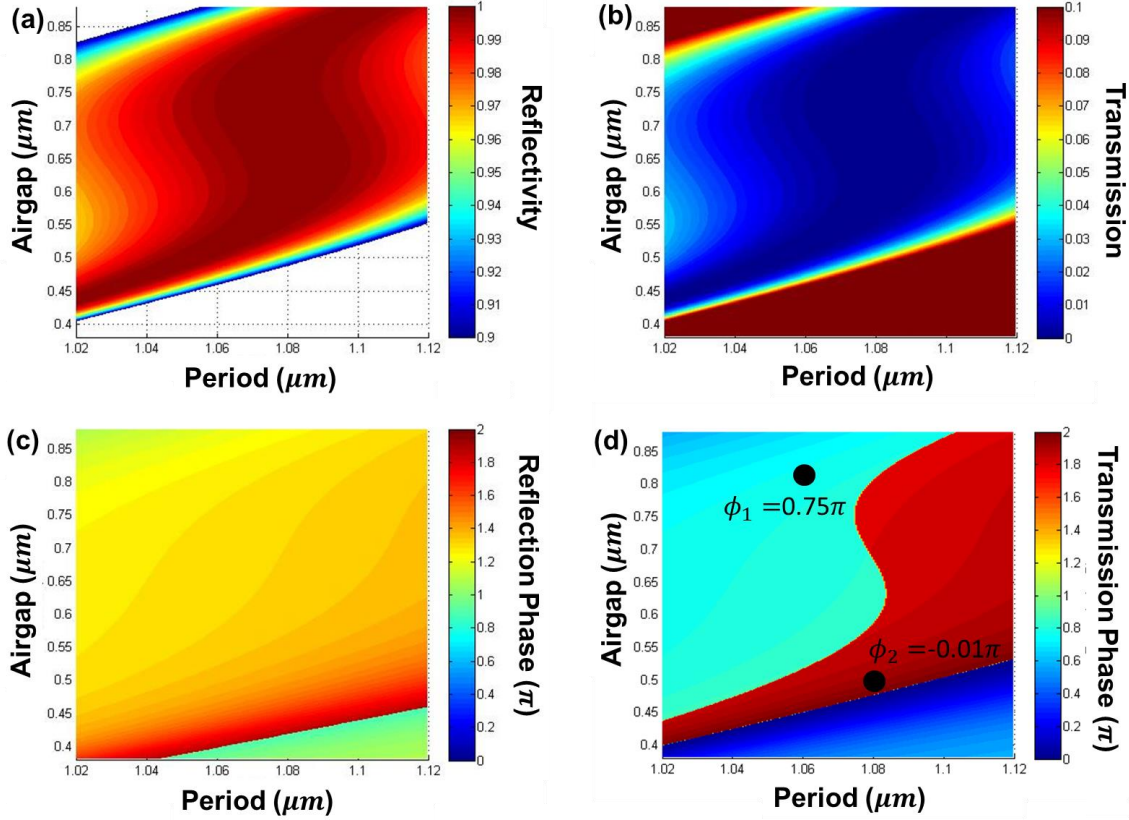
Figure 7.11 Reflection and transmission characteristics of a TE-mode 1550-nm HCG with t_g=195 nm, simulated with HCG-solver analytical solution. (**a**) Reflectivity contour versus period and airgap, showing R>90%. (**b**) Transmission contour versus period and airgap, showing T<10%. (**c**) Reflection phase versus period and airgap, providing only <0.2**π** phase variation for this HCG dimension range with high reflectivity. (**d**) Transmission phase versus period and airgap, showing a **π** phase abruption between the light blue and red regions matching with the R=100% line in (a). The $\boldsymbol{\phi_1 = 0.75\pi}$ for dimension (**Λ**=1060 nm, a=820 nm), and $\boldsymbol{\phi_2 = -0.01\pi}$ for dimension (**Λ**=1080 nm, a=480 nm) are highlighted which are located at both sides of the abruption line. The line between the red region and blue region is **2π** –fold, indicating the same phase for red and blue regions.

In the same format as Figure 7.4 for angular modulation of HCG transmission amplitude, Figure 7.12 illustrates how the spatial chirping of HCG transmission phase is translated into the distribution of far-field intensities. The HCG dimension is not uniform here, instead it is chirped by alternating between the two dimensions indicated in Figure 7.11 (d) with transmission phase $\phi_1 = 0.75\pi$ and $\phi_2 = -0.01\pi$. The transmission phase difference here reaches ~0.75π, much larger than the reflection phase range (<0.2π). The Gaussian beam generated by VCSEL laser aperture propagates through the spatially chirped HCG. After superimposing the phase factor at each spatial position, the resulting E-field of the Gaussian beam is plotted in the near-field. The Gaussian beam then propagates from the near-field to the far-field through Fourier transform. In the far-field, the spatial components of the Gaussian beam carrying ϕ_1 and ϕ_2 interfere with each other and result in the re-shaped far-field distribution, - a double-lobe pattern. Mathematically, it is like the sum of each spatial component (with different phase factors) going through a "squared" process by Fourier transform so that the phase part gets expressed in the far-

field. This is different from Figure 7.4 where each angular component already went through the "sum" process by Fourier transform from near-field to far-field. If at this point each angular component gets superimposed with different phase factors (if they exist), and they will only be "squared" individually to achieve far-field pattern. Thus the phase factors are canceled out and not expressed in the angular modulation of far-field even if they exist. Therefore, angular phase information is neglected in the process of Figure 7.4 and only the angular transmission amplitude matters.
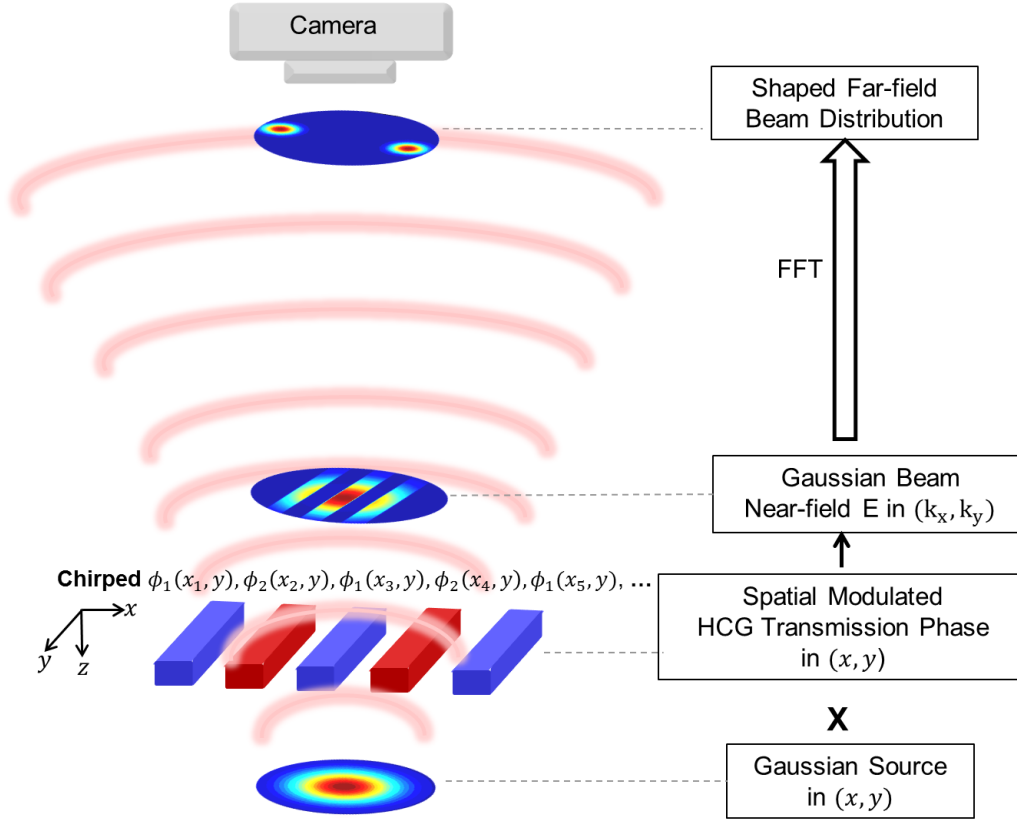
Figure 7.12 The schematic process of far-field emission pattern manipulation with HCG as a transmission spatial modulation plate. The case exemplifies here shows an HCG with transmission phase chirped by alternating between ϕ_1 and ϕ_2, thus yielding a double-lobe far-field pattern instead of Gaussian shape.

Furthermore, we tried changing the periodicity of the spatial chirping and analytically calculated the corresponding far-field distribution. As displayed in Figure 7.13, rows (a), (b), (c) are the spatial HCG phase distribution (alternating between ϕ_1 and ϕ_2 in Figure 7.11 (d)), E-field of Gaussian beam after phase superposition, and the resulting far-field distribution, respectively. On the other hand, column (i) represents the phase chirping with 2 periods each alternating between HCG designs-1 and design-2, while 4 periods each for column (ii), and then half of HCG bars with ϕ_1 and the other half with ϕ_2 in column (iii). The maximum divergence angle of ~20 ° can be achieved between the two lobes which is decreased with increasing the

chirping period. And by arranging half side of the HCG bars as design-1 with ϕ_1 and the other half as design-2, the intensity between the two lobes can be modulated.
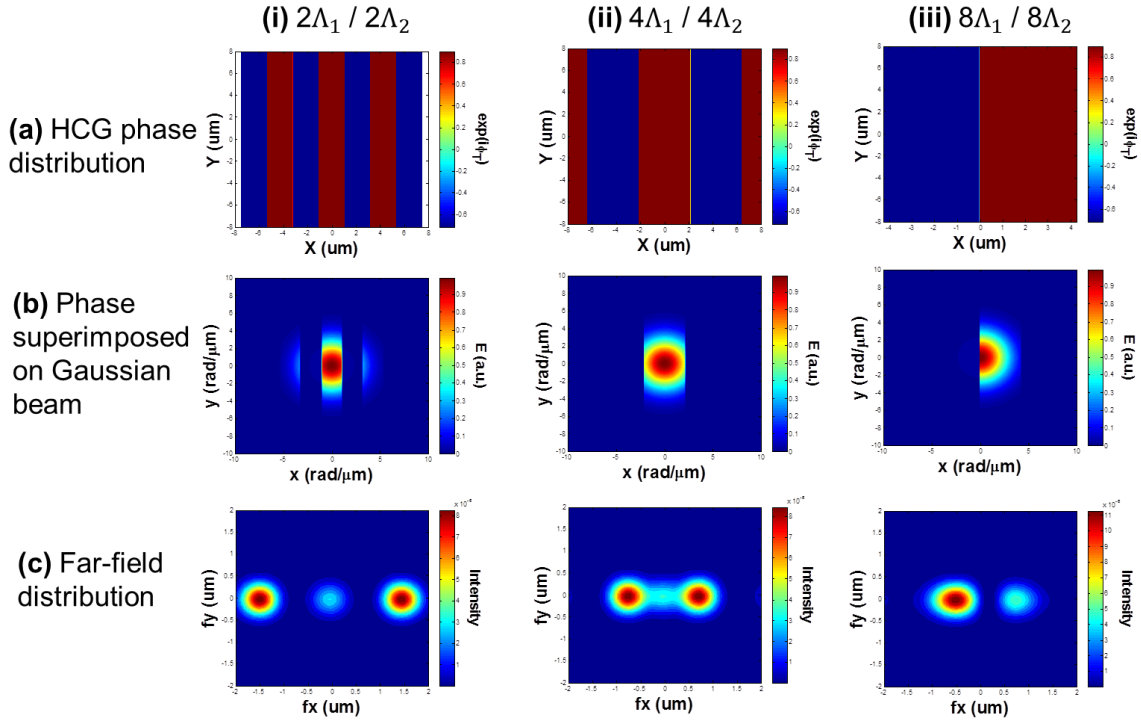
Figure 7.13 The analytical calculation of far-field distribution from spatially chirped HCG with an alternation between design-1 and design-2 in Figure 7.11 (d) for the chirping periods of **(i)** 2**Λ** each, **(ii)** 4**Λ** each, and **(iii)** 8**Λ** each for half side of HCG. The figures calculated are **(a)** HCG phase distribution in the form of **exp(iϕ_T)**, **(b)** E-field of the Gaussian beam after the superimposing of phase information, **(c)** the resulting far-field distribution.

Although this it a preliminary study, it shows the potential of dual beam generation with a divergence angle as large as ~20°. This large divergence angle is generated by beam-shaping with spatial modulation of HCG transmission phase. This is promising for applications such as simultaneous coupling into two fibers or special-shaped optical elements. Further research is needed to combine this with the angular modulation of HCG transmission amplitude in section 7.3, and create full beam-shaping with the monolithic HCG element.

7.6 Summary

We reported a novel beam-shaping scheme of far-field pattern from a single-mode VCSEL using the unique transmission characteristics of a HCG mirror. It is shown that a HCG can be designed to simultaneously provide high reflectivity to support the lasing of a single transverse mode, as well as a tailorable transmission profile to shape the output beam pattern. This originates from the angular dependence of the HCG transmission. The design of the far-field patterns is discussed, and both the simulation and experimental results are presented, which are in excellent agreement. The HCG is thus demonstrated as a dual function optical element, which can act as

an integrated tunable mirror as well as an integrated beam-shaping optical element. A single-mode dual-beam laser is demonstrated, with the front-surface emission beam being shaped by HCG designs while the back-surface emission remaining as Gaussian shape. We also performed preliminary study for spatial modulation of HCG transmission phase, which can be combined together with angular modulation of HCG transmission amplitude for more flexible beam-shaping. This work opens up possibilities to design arbitrary far field patterns directly from a VCSEL without the addition of any secondary optical element. It is thus promising for a variety of applications requiring beam shaping, such as particle trapping, cell manipulation, high efficiency optical coupling to optical fibers and grating couplers.

Chapter 8
Summary and Outlook

In summary, two research aspects promoting the development of integrated optoelectronics on the device level are discussed in this dissertation – material integration and function integration.

The material integration approach discussed here focuses on high-quality InP nanostructures grown directly on silicon substrate. The unique core-shell growth mode allows the scale-up of nanostructure diameters to go far beyond the lattice-mismatched critical dimensions. The micro-sized pillars thus enable superior optical properties compared with traditional nanowires. Furthermore, the low-temperature MOCVD technique without any external catalyst enables post-CMOS compatible processes.

In this dissertation, three types of crystal phases are explored in the nanoneedles, including ZB/WZ-mixed phase, mostly ZB-phase, and single-crystal WZ-phase. The optical properties of each category were studied and linked to the physics of the different underlying band structures. All three classes of nanoneedles are able to achieve optically-pumped lasing at different wavelengths. InP nanolasers growtn on silicon could form the basis of long-wavelength heterostructure III-V lasers emitting at silicon-transparent wavelength. The single-crystal WZ-phase nanoneedles show the largest bandgap (~1.41 eV at 298 K) and the most efficient radiative carrier recombination mechanism validated by its carrier recombination lifetime and internal quantum efficiency (IQE). It is thus selected as the excellent material platform for nanoneedle/nanopillar-based optoelectronic devices such as nanolasers, photovoltaics, photodetectors, etc. The surface quality of the single-crystal wurtzite-phase micropillar is further investigated. Unique features are identified in the carrier recombination lifetimes of these nanopillars at room temperature enabled by the ultra-bright emission. The methodology of combining room-temperature recombination lifetimes and IQE values to obtain the surface recombination velocity (SRV) of the pillar is demonstrated. With a SRV value of 1.1×10^3 cm/sec and the radiative recombination B coefficient of 2.0×10^{-10} cm^3/sec, it is verified that the material quality of the InP micropillars grown on silicon approaches that of the InP bulk. This unprecedented metastable direct growth of InP micropillars monolithically on silicon thus combines the strengths of nanostructures and bulk materials, and provides an avenue in the integration of optoelectronics with silicon-based technologies.

The function integration approach discussed here primarily centers around a key element – high-contrast subwavelength grating (HCG). The ultrathin layer of monolithic grating element is endued with intriguing rich properties, among which the ultra-broadband high reflection enables its implementation in vertical-cavity surface-emitting lasers (VCSEL). Compared with the traditional distributed Bragg reflector (DBR) mirror, the integrated HCG tuning mirror offers numerous advantages. First of all, the single monolithic layer greatly mitigates the epitaxial and fabrication complexities. The compact form factor and greatly-reduced weight also facilitates fast MEMS actuation. Furthermore, the emission is polarization selective for 1D HCG structure, which is desired by some applications.

In this dissertation, a widely and fast tunable 1060-nm VCSEL using 1D-HCG tunable top mirror is demonstrated, aiming at swept-source optical coherence tomography (SS-OCT) and

light detection & ranging (LiDAR) applications. An ultralow threshold of <100 µA and high output power of >1.3 mW are attained for single-mode lasing at CW operation. The laser also offers outstanding thermal characteristics, with lasing above 110 °C and low thermal resistance of 0.88 °C/mW. A continuous tuning range of ~40 nm is achieved by actuating the HCG MEMS with an electrostatic tuning voltage. The tuning voltage can further be increased by improving the free spectral range (FSR) of the epitaxial wafer design. Thought it's optimized for wide tuning range over fast tuning speed, a 3-dB bandwidth of 1.15 MHz is still demonstrated which is enough to meet the requirement for SS-OCT. Design and lasing are also demonstrated for 2D-HCG VCSELs. This preliminary result shows promise for polarization-independent applications such as multi-stable optical sources and all optical flip-flop operations. Inspired by the method of designing the HCG reflectivity to realize transverse-mode control of VCSEL for single-mode yield improvement, the angular-dependence of HCG is explored. It turns out the HCG transmission intensity can be modulated in the angular domain thus to perform certain degree of beam-shaping. The design of the far-field patterns is discussed, followed by the fabrication and characterization of HCG-VCSELs whose far-field distributions match very well with the designs and simulations. An array of VCSELs all emitting at single-mode at CW operation can deliver a variety of far-field emission patterns, such as Gaussian, double-lobe, triple-lobe, bow-tie, donut, etc. While the front-side emission is modulated and tailored by different HCG designs, the back-side emission through DBR mirror still remains as Gaussian. This two-face dual-beam VCSEL is demonstrated by the first time. Furthermore, except for angular modulation of HCG transmission amplitude, the HCG is also able to be designed for spatial modulation of its transmission phase. Preliminary results are simulated which are promising for beam-shaping with another degree of freedom. These two methods combined together open up possibilities to design arbitrary far-field patterns directly from a VCSEL without the addition of any secondary optical element. The HCG shows its great potential working both as an integrated tuning mirror and an integrated beam-shaping element for optoelectronics.

97

Bibliography

[1]   R. Chen, T. D. Tran, K. W. Ng, W. S. Ko, L. C. Chuang, F. G. Sedgwick, C. Chang-Hasnain, "Nanolasers grown on silicon," *Nature Photonics,* vol. 5, no. 3, pp. 170-175, 2011.

[2]   M. Moewe, L. C. Chuang, S. Crankshaw, C. Chase, C. Chang-Hasnain, "Atomically sharp catalyst-free wurtzite GaAs/AlGaAs nanoneedles grown on silicon," *Applied Physics Letters,* vol. 93, no. 2, pp. 23116-23116, 2008.

[3]   K. W. Ng, T. D. Tran, W. S. Ko, R. Chen, F. Lu, C. J. Chang-Hasnain, "Single crystalline InGaAs nanopillar grown on polysilicon with dimensions beyond the substrate grain size limit," *Nano letters,* vol. 13, no. 12, pp. 5931-5937, 2013.

[4]   F. Ren, K. W. Ng, K. Li, H. Sun, C. J. Chang-Hasnain, "High-quality InP nanoneedles grown on silicon," *Applied Physics Letters,* vol. 102, no. 1, p. 012115, 2013.

[5]   F. Lu, T. D. Tran, W. S. Ko, K. W. Ng, R. Chen, C. Chang-Hasnain, "Nanolasers grown on silicon-based MOSFETs," *Optics express,* vol. 20, no. 11, pp. 12171-12176, 2012.

[6]   K. W. Ng, W. S. Ko, T. D. Tran, R. Chen, M. V. Nazarenko, F. Lu, V. G. Dubrovskii, M. Kamp; A. Forchel; C. J. Chang-Hasnain, "Unconventional growth mechanism for monolithic integration of iii–v on silicon," *ACS nano,* vol. 7, no. 1, pp. 100-107, 2012.

[7]   K. Li, H. Sun, F. Ren, K. W. Ng, T. D. Tran, R. Chen, C. J. Chang-Hasnain, "Tailoring the optical characteristics of microsized InP nanoneedles directly grown on silicon," *Nano letters,* vol. 14, no. 1, pp. 183-190, 2013.

[8]   K. Li, K. W. Ng, T. D. Tran, H. Sun, F. Lu, C. J. Chang-Hasnain, "Wurtzite-phased InP micropillars grown on silicon with low surface recombination velocity," *Nano letters,* vol. 15, no. 11, pp. 7189-7198, 2015.

[9]   M. C. Y. Huang, Y. Zhou, and C. J. Chang-Hasnain, "A nanoelectromechanical tunable laser," *Nature Photonics,* vol. 2, pp. 180-184, 2008.

[10]   Y. Rao, W. Yang, C. Chase, M. C. Y. Huang, D. P. Worland, S. Khaleghi, M. R. Chitgarha, M. Ziyadi, A. E. Willner, and C. J. Chang-Hasnain, "Long-Wavelength VCSEL Using High Contrast Grating," *Selected Topics in Quantum Electronics, IEEE Journal of,* vol. 19, p. 1701311, 2013.

[11]   Y. Zhou, M. Moewe, J. Kern, M. C. Y. Huang, and C. J. Chang-Hasnain, "Surface-normal emission of a high-Q resonator using a subwavelength high-contrast grating," *Optics Express,* vol. 16, pp. 17282-17381, 2008.

[12]   F. Lu, F.G. Sedgwick, V. Karagodsky, C. Chase and C.J. Chang-Hasnain, "Planar high-numerical-aperture low-loss focusing reflectors and lenses using subwavelength high

contrast gratings," *Optics Express,* vol. 18, pp. 12606-12614, 2010.

[13] W. Yang, J. Ferrara, K. Grutter, A. Yeh, C. Chase, Y. Yue, A. E. Willner, M. Wu, and C. J. Chang-Hasnain, "Low loss hollow-core waveguide on a silicon substrate," *Nanophotonics,* vol. 1, pp. 23-29, 2012.

[14] W. Yang, S. A. Gerke, K. W. Ng, Y. Rao, C. Chase, C. J. Chang-Hasnain, "Laser optomechanics," *Scientific reports,* vol. 5, 2015.

[15] C. J. Chang-Hasnain and W. Yang, "High-contrast gratings for integrated optoelectronics," *Advances in Optics and Photonics,* vol. 4, pp. 379-440, 2012.

[16] K. Li, C. Chase, Y. Rao, C. J. Chang-Hasnain, "Widely tunable 1060-nm high-contrast grating VCSEL," in *IEEE Compound Semiconductor Week (CSW)*, Toyama, Japan, 2016.

[17] K. Li, Y. Rao, C. Chase, W. Yang, C. J. Chang-Hasnain, "Beam-Shaping Single-Mode VCSEL With A High-Contrast Grating Mirror," in *CLEO: Science and Innovations, SF1L. 7*, San Jose, CA, 2016.

[18] R. Chen, "Doctoral Degree Dissertation: Nano-Optoelectronic Integration on Silicon," University of California at Berkeley, 2012.

[19] M. E. Groenert, C. W. Leitz, A. J. Pitera, V. Yang, H. Lee, R. J. Ram, E. A. Fitzgerald, "Monolithic integration of room-temperature cw GaAs/AlGaAs lasers on Si substrates via relaxed graded GeSi buffer layers," *Journal of applied physics,* vol. 93, no. 1, pp. 362-367, 2003.

[20] D. K. Biegelsen, F. A. Ponce, A. J. Smith, J. C. Tramontana, "Initial stages of epitaxial growth of GaAs on (100) silicon," *Applied physics,* vol. 61, p. 1856, 1987.

[21] K. Tomioka, T. Tanaka, S. Hara, K. Hiruma, T. Fukui , "III-V nanowires on Si substrate: selective-area growth and device applications," *IEEE Journal of Selected Toppics in Quantum Electronics,* vol. 17, no. 4, pp. 1112-1129, 2011.

[22] K. Tomioka and T. Fukui , "Recent progress in integration of III-V nanowire transistors on Si substrate by selective-area growth," *J. Phys. D: Appl. Phys.,* vol. 47, p. 394001, 2014.

[23] T. Martensson, S. Patrik, T. Svensson, B. A. Wacasar, M. W. Larsson, W. Seifert, K. Deppert, A. Gustafsson, L. R. Wallenberg, L. Samuelson, "Epitaxial III-V nanowires on silicon," *Nano letters,* vol. 4, no. 10, pp. 1987-1990, 2004.

[24] Y. Watanabe, H. Hibino, S. Bhunia, K. Tateno, T. Sekiguchi, "Site-controlled InP nanowires grown on patterned Si substrates," *Phys. E,* vol. 24, no. 4, pp. 133-137, 2004.

[25] V. Khorenko, I. Regolin, S. Neuman, W. Prost, F.-J. Tegude, H. Wiggers, "Photoluminescence of GaAs nanowhiskers grown on Si substrate," *Applied physics letter,*

vol. 85, no. 26, pp. 6407-6409, 2004.

[26] A. L. Roest, M. A. Verheijen, O. Wunnicke, S. Serafin, H. Wondergem, E. P. A. M. Bakkers, "Position-controlled epitaxial III-V nanowires on silicon," *Nanotechnolog,* vol. 17, no. 14, pp. 271-275, 2006.

[27] M. Mattila, T. Hakkatainen, H. Lipsanen , "Catalyst-free growth of In(As)P nanowires on silicon," *Applied physics letter,* vol. 89, pp. 063119-063121, 2006.

[28] H. D. Park, S.M. Prokes, M. W. Twigg, R. C. Cammarata, A.-C. Gaillot, "Si-assisted growth of InAs nanowires," *Applied physics letter,* vol. 89, no. 22, pp. 223125-223127, 2006.

[29] T. Martensson, J. B. Wagner, E. Hilner, A. Mikkelsen, C. Thelanders, J. Stangl, B. J. Ohlsson, A. Gustafsson, E. Lundgren, L. Samuelson, W. Seifert, "Epitaxial growth of indium arsenide nanowires on silicon using nucleation templates formed by self-assembled organic coatings," *Advanced materials,* vol. 19, no. 6, pp. 1801-1806, 2007.

[30] F. Jabeen, V. Grillo, S. Rubini, F. Martelli, "Self-catalyzed growth of GaAs nanowires on cleaved Si by molecular beam epitaxy," *Nanotechnology,* vol. 19, no. 27, pp. 27511-27517, 2008.

[31] K. Tomioka, Y. Kobayashi, J. Motohisa, S. Hara, T. Fukui, "Selective-area growth of vertically aligned GaAs and GaAs/AlGaAs core-shell nanowires on Si(111) substrate," *Nanotechnology,* vol. 20, no. 14, pp. 145302-145309, 2009.

[32] M. Cantoro, G. Brammertz, O. Richard, H. Bender, F. Clemente, M. Lays, S. Degroode, M. Caymax, M. Hwyns, S.D. Gendt, "Controlled III/V nanowire growth by selective-area vapor phase epitaxy," *Journal of electrochemistry,* vol. 156, no. 11, pp. 860-868, 2009.

[33] T. Tanaka, K. Tomioka, S. Hara, J. Motohisa, E. Sano, T. Fukui , "Vertical surrounding gata transistors using single InAs nanowires grown on Si substrates," *Applied physics express,* vol. 3, no. 2, pp. 025003-025005, 2010.

[34] J. C. Shin, K. H. Kim, K. J. Yu, H. Hu, L. Yin, C. Z. Ning, J. A. Rogers, J. M. Zuo, X. Li, "InxGa1-xAs nanowires on silicon: one-dimensional heterogeneous epitaxy, bandgap engineering, and photovoltaics," *Nano letters,* vol. 11, pp. 4831-4838, 2011.

[35] P. Krogstrup, H. I. Jorgensen, M. Heiss, O. Demichel, J. V. Holm, M. Aagesen, J. Nygard, A. F. I. Morral, "Single-nanowire solar cells beyond the Shockley-Queisser limit," *Nature photonics,* vol. 7, pp. 306-310, 2013.

[36] B. Mayer, D. Rudolph, J. Schnell, S. Morkotter, J. Winnerl, J. Treu, K. Muller, G. Bracher, G. Abstreiter, G. Koblmuller, J. J. Finley, "Lasing from individual GaAs-AlGaAs core-shell nanowires up to room temprature," *Nature communication,* vol. 4, p. 2931, 2013.

[37] H. Takeuchi, A. Wung, X. Sun, R. T. Howe, T. King , "Thermal budget limits of quarter-micrometer foundry CMOS for post-processing MEMS devices," *IEEE Trans. Electron Devices,* vol. 52, no. 9, pp. 2081-2086, 2005.

[38] L. C. Chuang, M. Moewe, C. Chase, N. P. Kobayashi, C. Chang-Hasnain, "Critical diameter for III-V nanowires grown on lattice-mismatched substrates," *Applied physics letter,* vol. 90, p. 043115, 2007.

[39] A. Black, A. Rhawkins, N. M. Margalit, D. I. Babic, J. Holmes, AlIl, Y.-L. Chang, P. Abraham, J. E. Bowers, E. L. Hu, "Wafer fusion: materials issues and device results," *IEEE Journal of selected topics in quantum electronics,* vol. 3, no. 3, pp. 943-951, 1997.

[40] U. Gosele and Q.-Y. Tong, "Semiconductor wafer bonding," *Annual review of materials science,* vol. 28, no. 1, pp. 215-241, 1998.

[41] R. E. Camacho-Aguilera, Y. Cai, N. Patel, J. T. Bessette, M. Romagnoli, L. C. Kimerling, J. Michel, "An electrically pumped germanium laser," *Optics express,* vol. 20, no. 10, pp. 11316-11320, 2012.

[42] L. C. Chuang, "Doctoral Degree Dissertation: III-V nanowires and nanoneedles on lattice mismatched substrates for optoelectronic device applications," University of California at Berkeley, 2011.

[43] M. Moewe, "Doctoral Degree Dissertation: Growth and characterization of III-V nanowires and nanoneedles," University of California at Berkeley, 2009.

[44] L. C. Chuang, M. Moewe, K. W. Ng, T. D. Tran, S. Crankshaw, R. Chen, W. S. Ko, C. Chang-Hasnain, "GaAs nanoneedles grown on sapphire," *Applied Physics Letters,* vol. 98, no. 12, p. 123101, 2011.

[45] L. C. Chuang, F. G. Sedgwick, R. Chen, W. S. Ko, M. Moewe, K. W. Ng, T. D. Tran, C. Chang-Hasnain, "GaAs-Based nanoneedle light emitting diode and avalanche photodiode monolithically integrated on a silicon substrate," *Nano letters,* vol. 11, pp. 385-390, 2011.

[46] K. Li, F. Ren, T. D. Tran, K. W. Ng, C. Chang-Hasnain, "Characteristics of InP nanoneedles grown on silicon by low-temperature MOCVD," in *Indium Phosphide and Related Materials (IPRM) – IEEE International Conference ,* Santa Barbara, CA, 2012.

[47] H. Sun, F. Ren, T. D. Tran, K. W. Ng, K. Li, C. Chang-Hasnain, "High quality InGaP micropillars directly grown on silicon," in *Photonics Society Summer Topical Meeting Series- IEEE International Conference ,* 50-51, 2013.

[48] R. Chen, D. Parekh, K. W. Ng, C. Chang-Hasnain, C. , "High-speed avalanche photodiodes using III-V nanopillars monolithically grown on silicon," in *Group IV Photonics (GFP)-IEEE 9th International Conference ,* 48-50, 2012.

[49] W. S. Ko, I. Bhattacharya, T. D. Tran, K. W. Ng, C. Chang-Hasnain, "InP nanowire avalanche photodiode and bipolar junction phototransistor integrated on silicon substrate," in *Int. Conf. on Indium Phosphide and Related Materials (IPRM) − IEEE International Conference* , Mo-B1-2, 2014.

[50] W. S. Ko, T. D. Tran, I. Bhattacharya, K. W. Ng, H. Sun, C. Chang-Hasnain, "Illumination angle insensitive single indium phosphide tapered nanopillar solar cell," *Nano letters,* vol. 15, no. 8, pp. 4961-4967, 2015.

[51] R. Chen, K. W. Ng, W. S. Ko, D. Parekh, F. Lu, T. D. Tran, K. Li, C. Chang-Hasnain, "Nanophotonic integrated circuits from nanoresonators grown on silicon," *Nature communications,* vol. 5, 2014.

[52] Foll Helmut, "III-V semiconductors. Semiconductor Technology and Nano Electronics Course Website," [Online]. Available: http://www.tf.uni-kiel.de/matwis/amat/semitech_en/kap_2/backbone/r2_3_1.html .

[53] L. M. Smith, H. E. Jackson, J. M. Yarrison-Rice, C. Jagadish, "Insights into single semiconductor nanowire heterostructures using time-resolved photoluminescence," *Semicond. Sci. Technol. ,* vol. 25, p. 024010, 2010.

[54] A. Scofield, S. H. Kim, J. N. Shapiro, A. Lin, B. L. Liang, A. Scherer, D. L. Huffaker, "Room Temperature Continuous Wave Lasing in Nanopillar Photonic Crystal Cavities," in *Conference on Lasers and Electro-Optics (CLEO)* , CTh4M, 2012.

[55] D. Saxena, S. Mokkapati, P. Parkinson, N. Jiang, Q. Gao, H. H. Tan, C. Jagadish, "Optically pumped room-temperature GaAs nanowire lasers," *Nature photonics,* vol. 7, pp. 963-968, 2013.

[56] Q. Gao, D. Saxena, F. Wang, L. Fu, S. Mokkapati, Y. Guo, L. Li, J. Wong-Leung, P. Caroff, H. H. Tan, C. Jagadish, "38Selective-area epitaxy of pure wurtzite InP nanowires: high quantum efficiency and room-temperature lasing," *Nano letters,* vol. 14, pp. 5206-5211, 2014.

[57] K. W. Ng, "Doctoral Degree Dissertation: III-V nanostructures on dissimilar substrates for optoelectronic applications," University of California at Berkeley, 2014.

[58] R. Chen, S. Crankshaw, T. D. Tran, L. C. Chuang, M. Moewe, C. Chang-Hasnain, "Second-harmonic generation from a single wurtzite GaAs nanoneedle," *Applied physics letter,* vol. 96, no. 5, p. 051110, 2010.

[59] T. X. Sayle, S. C. Parker, D. C. Sayle, "Ionic conductivity in nano-scale CeO2/YSZ heterolayers," *J. Mater. Chem.,* vol. 16, pp. 1067-1081, 2006.

[60] S. H. Huang, G. Balakrishnan, A. Khoshakhlagh, A. Jallipalli, L. R. Dawson, D. L. Huffaker, "Strain relief by periodic misfit arrays for low defect density GaSb on GaAs,"

Applied physics letter, vol. 88, p. 131911, 2006.

[61]   Ng, K. W.; Ko, W. S.; Lu, F.; Chang-Hasnain, C. J. , "Metastable growth of pure wurtzite InGaAs microstructures," *Nano letters,* vol. 14, pp. 4757-4762, 2014.

[62]   K. Ikejiri, Y. Kitauchi, K. Tomioka, J. Motohisa, T. Fukui, "Zinc blende and wurtzite crystal phase mixing and transition in indium phosphide nanowires," *Nano letters,* vol. 11, pp. 4314-4318, 2011.

[63]   T. T. T. Vu, T. Zehender, M. A. Verheijen, S. R. Plissard, G. W. G. Immink, J. E. M. Haverkort, E. P. A. M. Bakkers, "High optical quality single crystal phase wurtzite and zincblende InP nanowires," *Nanotechnology,* vol. 2014, pp. 115705-115710, 2013.

[64]   E. G. Gadret, G. O. Dias, L. C. O. Dacal, M. M. de Lima, Jr., C. V. R. S. Ruffo, F. Iikawa, M. J. S. P. Brasil, T. Chiaramonte, M. A. Cotta, L. H. G. Tizei, D. Ugarte, and A. Cantarero, "Valence-band splitting energies in wurtzite InP nanowires: Photoluminescence spectroscopy and ab initio calculations," *Physical Review B,* vol. 82, p. 125327, 2010.

[65]   J. M. Jancu, K. Gauthron, L. Largeau, G. Patriarche, J. C. Harmand, P. Voisin, "Type II heterostructures formed by zinc-blende inclusions in InP and GaAs wurtzite nanowires," *Applied physics letter,* vol. 97, p. 041910, 2010.

[66]   K. Miura, Y. Iguchi, M. Tsubokura, Y. Kawamura, "The growth of high quality GaAsSb and type-II InGaAs/GaAsSb superlattice structure," *Journal of applied physics,* vol. 113, p. 143506, 2013.

[67]   L. Zhang, J. W. Luo, A. Zunger, N. Akopian, V. Zwiller, J. C. Harmand, "Wide InP nanowires with wurtzite/zincblende superlattice segments are type-II whereas narrower nanowires become Type-I: an atomistic pseudopotential calculation," *Nano letters,* vol. 10, pp. 4055-4060, 2010.

[68]   J. Bao, D. C. Bell, F. Capasso, J. B. Wagner, T. Martensson, J. Tragardh, L. Samuelson, "Optical properties of rotationally twinned InP nanowire heterostructures," *Nano letters,* vol. 8, pp. 836-841, 2008.

[69]   S. Paiman, Q. Gao, H. J. Joyce, Y. Kim, H. H. Tan, C. Jagadish, X. Zhang, Y. Guo, J. Zou, "Growth temperature and V/III ratio effects on the morphology and crystal structure of InP nanowires," *J. Phys. D: Appl. Phys.,* vol. 97, p. 041910, 2010.

[70]   K. P. O'Donnel and X. Chen, "Temperature dependence of semiconductor band gaps," *Applied physics letter,* vol. 58, pp. 2924-2926, 1991.

[71]   Y. Kobayashi, M. Fukui, J. Motohisa, T. Fukui, "Micro-photoluminescence spectroscopy study of high-quality InP nanowires grown by selective-area metalorganic vapor phase epitaxy," *Physica. E,* vol. 40, pp. 2204-2206, 2008.

[72] A. Mishra, L. V. Titova, T. B. Hoang, H. E. Jackson, L. M. Smith, J. M. Yarrison-Rice, Y. Kim, H. J. Joyce, Q. Gao, H. H. Tan, C. Jagadish, "Polarization and temperature dependence of photoluminescence from zincblende and wurtzite InP nanowires," *Applied physics letter,* vol. 91, p. 263104, 2007.

[73] PicoQuant, "Time-Resolved Photoluminescence," PicoQuant, [Online]. Available: https://www.picoquant.com/applications/category/materials-science/time-resolved-photoluminescence. [Accessed 2016].

[74] N. Akopian, G. Patriarche, L. Liu, J. C. Harmand, V. Zwiller, "Crystal phase quantum dots," *Nano letters,* vol. 10, pp. 1198-1201, 2010.

[75] K. Pemasiri, M. Montazeri, R. Gass, L. M. Smith, H. E. Jackson, J. Yarrison-Rice, S. Paiman, Q. Gao, H. H. Tan, C. Jagadish, X. Zhang, J. Zou, "Carrier dynamics and quantum confinement in type II ZB-WZ InP nanowire homostructures," *Nano letters,* vol. 9, pp. 648-654, 2009.

[76] S. Reitzenstein, S. Munch, C. Hofmann, A. Forchel, S. Crankshaw, L. C. Chuang, M. Moewe, C. Chang-Hasnain, "Time resolved microphotoluminescence studies of single InP nanowires grown by low pressure metal organic chemical vapor deposition," *Applied physics letter,* vol. 91, p. 091103, 2007.

[77] N. Chauvin, M. H. H. Alouane, R. Anufriev, H. Khmissi, K. Naji, G. Patriarche, C. Bru-Chevallier, M. Gendry, "Growth temperature dependence of exciton lifetime in wurtzite InP nanowires grown on silicon substrate," *Applied physics letter,* vol. 100, p. 011906, 2012.

[78] S. Chrankshaw, S. Reitzenstein, L. C. Chuang, M. Moewe, S. Munch, C. Bockler, A. Forchel, C. Chang-Hasnain, "Recombination dynamics in wurtzite InP nanowires," *Physics Review B,* vol. 77, p. 235409, 2008.

[79] S. Watanabe, N. Yamada, M. Nagashima, Y. Ueki, C. Sasaki, Y. Yamada, T. Taguchi, K. Tadatomo, H. Okagawa, H. Kudo, "Internal quantum efficiency of highly-efficient InxGa1-xN-based near-ultraviolet light-emitting diodes," *Applied physics letter,* vol. 83, p. 4906, 2003.

[80] M. T. Borgstrom, J. Wallentin, M. Heurlin, S. Falt, P. Wickert, J. Leene, M. H. Magnusoon, K. Deppert, L. Samuelson, "Nanowires with promise for photovoltaics," *IEEE Journal of selected topics in quantum electronics,* vol. 17, pp. 1050-1061, 2011.

[81] R. T. Ross, "Some thermodynamics of photochemical systems," *Journal of chemistry physics,* vol. 46, pp. 4590-4593, 1967.

[82] O. Miller and E. Yablonovitch , "Intense internal and external fluorescence as solar cells approach the Shockley-Queisser efficiency limit," *IEEE J. Photovoltaics ,* vol. 2, pp. 303-311, 2012.

[83] T. D. Tran, R. Chen, K. W. Ng, W. S. Ko, F. Lu, C. J. Chang-Hasnain, "Three-dimensional whispering gallery modes in InGaAs nanoneedle lasers on silicon," *Applied physics letters,* vol. 11, p. 111105, 2014.

[84] J. C. Johnson, K. P. Knutsen, H. Yan, M. Law, Y. Zhang, P. Yang, R. J. Saykally, "Ultrafast carrier dynamics in single ZnO nanowire and nanoribbon lasers," *Nano letters,* vol. 4, pp. 197-204, 2004.

[85] S. Munch, S. Reitzenstein, M. Borgstrom, C. Thelander, L. Samuelson, L. Worschech, A. Forchel, "Time-resolved photoluminescence investigations on HfO2-capped InP nanowires," *Nanotechnology,* vol. 21, p. 105711, 2010.

[86] H. J. Joyce, J. Wong-Leung, C.-K. Yong, C. J. Docherty, S. Paiman, Q. Gao, H. H. Tan, C. Jagadish, J. Lloyd-Hughes, L. M. Herz, M. B. Johnson, "Ultralow surface recombination velocity in InP nanowires probed by terahertz spectroscopy," *Nano letters,* vol. 12, pp. 5325-5330, 2012.

[87] Y. S. Yoo, T. M. Roh, J. H. Na, S. J. Son, Y. H. Cho, "Simple analysis method for determining internal quantum efficiency and relative recombination ratios in light emitting diodes," *Applied physics,* vol. 102, p. 211107, 2013.

[88] F. Wang, Q. Gao, K. Peng, Z. Li, Z. Li, Y. Guo, L. Fu, L. M. Smith, H. H. Tan, C. Jagadish, "Spatially resolved doping concentration and nonradiative lifetime profiles in single Si-doped InP nanowires using photoluminescence mapping," *Nanoletters,* vol. 15, pp. 3017-3023, 2015.

[89] A. Liu and Y. Rosenwaks , "Excess carriers lifetime in InP single crystals: radiative versus nonradiative recombinations," *Journal of applied physics,* vol. 86, p. 430, 1999.

[90] T. D. Tran, H. Sun, K. W. Ng, K. Li, F. Lu, E. Yablonovitch, C. J. Chang-Hasnain, "High brightness InP micropillars grown on silicon with Fermi level splitting larger than 1 eV," *Nano letters,* vol. 14, pp. 3235-3240, 2014.

[91] M. E. Levinshtein, S. L. Rumyantsev, M. Shur, Handbook Series on Semiconductor Parameters. 1. Si, Ge, C (diamond), GaAs, GaP, GaSb, InAs, InP, InSb, New York: World Scientific Publishing Company, Incorporated, 1996.

[92] R. K. Ahrenkiel, D. J. Dunlavy, T. Hanak, "Minority-carrier lifetime in ITO/InP heterojunctions," *Journal of applied physics,* vol. 64, no. 4, pp. 1916-1921, 1986.

[93] L. A. Coldren and S. W. Corzine, Diode lasers and photonic integrated circuits, New York: Wiley, 1995.

[94] S. Jahangir, A. Banerjee, P. Bhattacharya, "Carrier lifetimes in green emitting InGaN/GaN disks-in-nanowire and characteristics of green light emitting diodes," *Phys. Status Solidi C,* vol. 10, no. 5, pp. 812-815, 2013.

[95] H. C. Jr. Casey and E. Buehler, "Evidence for low surface recombination velocity on n-type InP," *Applied physics letter,* vol. 30, pp. 247-249, 1977.

[96] C. A. Hoffman, K. Jarasiunas, H. J. Gerritsen, A. V. Nurmikko, "Measurement of surface recombination velocity in semiconductors by diffraction from picosecond transient free carrier gratings," *Applied physics letter,* vol. 33, no. 6, pp. 536-539, 1978.

[97] P. Bandaru and E. Yablonovitch , "Semiconductor surface-molecule interactions wet etching of InP by α-hydroxy acids," *Journal of The Electrochemical Society ,* vol. 149, no. 11, pp. G599-G602, 2002.

[98] W. Yang, T. Sun, Y. Rao, M. Megens, T. Chan, B.-W. Yoo, D. A. Horsley, M. C. Wu, and C. J. Chang-Hasnain, "High-speed optical phased array using two-dimensional high-contrast grating all-pass filters," in *Proceedings of SPIE 8633, High Contrast Metastructures II,*, San Francisco, 2013.

[99] L. Zhu, V. Karagodsky, and C. Chang-Hasnain, "Novel high efficiency vertical to in-plane optical coupler," in *Proceedings of SPIE 8270, High Contrast Metastructures, 82700L*, San Francisco, USA, 2012.

[100] T. Sun, S. Kan, G. Marriott, C. J. Chang-Hansnain, "High-contrast grating resonators for label-free detection of disease biomarkers," *Scientific reports,* vol. 6, p. 27482, 2016.

[101] W. Yang and C. J. Chang-Hasnain, "Ultra-compact optical switch using high contrast grating hollow-core waveguide," in *Conference on Lasers and Electro-Optics, OSA Technical Digest*, San Jose, USA, 2013.

[102] "Wikipedia," Wikipedia, [Online]. Available: https://en.wikipedia.org/wiki/Laser_diode.

[103] S. L. Chuang, in *Physics of photonic devices*, Wiley, 2009, p. 411.

[104] R. Koda, "Doctoral Degree Dissertation: All-expitaxial, long-wavelength VCSEls using bipolar cascaded active region for high differential quantum efficiency," University of California at Santa Barbara, 2005.

[105] Y. Rao, "Doctoral Degree Dissertation: InP-based long wavelength VCSEL using high contrast grating," University of California at Berkeley, 2012.

[106] S. Jatta, B. Kogel , M. Maute, K. Zogal, F. Riemenschneider, G. Bohm, M.-C. Amann, P. Meisner, "Bulk-Micromachined VCSEL At 1.55 μm With 76-nm Single-Mode Continuous Tuning Range," *IEEE Photonics technology letters,* vol. 21, no. 24, pp. 1822-1824, 2009.

[107] T. Yano, H. Saitou, N. Kanbara, R. Noda, S.-i. Tezuka, N. Fujimura, M. Ooyama, T. Watanabe, T. Hirata, N. Nishiyama, "Wavelength Modulation Over 500 kHz of Micromechanically Tunable InP-Based VCSELs With Si-MEMS Technology," *IEEE Journal of Selected Topics in Quantum Electronics,* vol. 15, no. 3, pp. 528-534, 2009.

[108] M. S. Wu, E. C. Vail, G. S.Li, W. Yuen, and C. J. Chang-Hasnain, "Tunable micromachined vertical cavity surface emitting laser," *Electronic Letters,* vol. 31, no. 19, pp. 1671-1672, 1995.

[109] M. C. Larson, A. R. Massengale, J. S. Harris, "Continuously tunable micromachined vertical cavity surface emitting laser with 18 nm wavelength range," *Electronics Letters,* vol. 32, no. 4, pp. 330-332, 1996.

[110] C. Gierl, T. Gruendl, P. Debernardi, K. Zogal, C. Grasse, H. A. Davani, G. Bohm, S. Jatta, F. Kuppers, P. Meibner and M. C. Amann, "Surface micromachined tunable 1.55 μm-VCSEL with 102 nm continuous single-mode tuning," *Optics Express,* vol. 19, no. 18, pp. 17336-17343, 2011.

[111] C. F. R. Mateus, M. C. Y. Huang, Y. Deng, A. R. Neureuther, and C. J. Chang-Hasnain, "Ultra-broadband mirror using low index cladded subwavelength grating," *IEEE Photonics Technology Letters,* vol. 16, pp. 518-520, 2004.

[112] C. F. R. Mateus, M. C. Y. Huang, L. Chen, and C. J. Chang-Hasnain and Y. Suzuki, "Broadband mirror (1.12-1.62 um) using single-layer sub-wavelength grating," *IEEE Photonics Technology Letters,* vol. 16, pp. 1676-1678, 2004.

[113] M. C. Y. Huang, Y. Zhou, and C. J. Chang-Hasnain, "A surface-emitting laser incorporating a high index-contrast subwavelength grating," *Nature Photonics,* vol. 1, pp. 119-122, 2007.

[114] C. Chase, Y. Zhou, C.J. Chang-Hasnain, "Size effect of high contrast gratings in VCSELs," *Optics Express,* vol. 17, p. 24002 – 24007, 2009.

[115] W. Hofmann, C. Chase, M. Müller, Y. Rao, C. Grasse, G. Böhm, M.-C. Amann, and Connie Chang-Hasnain, "Long-Wavelength High-Contrast Grating Vertical-Cavity Surface-Emitting Laser," *IEEE Photonics Journal,* vol. 2, pp. 415-422, 2010.

[116] C. Chase, Y. Rao, W. Hofmann, and C. J. Chang-Hasnain, "1550 nm high contrast grating VCSEL," *Optics Express,* vol. 18, pp. 15461-15466, 2010.

[117] J. Ferrara, W. Yang, L. Zhu, P. Qiao, C. J. Chang-Hasnain, "Heterogeneously integrated long-wavelength VCSEL using silicon high contrast grating on an SOI substrate," *Optics express,* vol. 23, no. 3, pp. 2512-2523, 2015.

[118] L. Zhu, J. Ferrara, C. J. Chang-Hasnain, "Flexible HCG-VCSEL," Compound Semiconductor Week 2015, Santa Barbara, CA, 2015.

[119] T. Ansbaek, I.-S. Chung, E. S. Semenova, and K. Yvind, "1060-nm tunable monolithic high index contrast subwavelength grating VCSEL," *IEEE Photonics Technology Letters,* vol. 24, pp. 455-457, 2013.

[120] D. D. John, C. B. Burgner, B. Potsaid, M. E. Robertson, B. K. Lee, W. J. Choi, A. E. Cable, J. G. Fujimoto, V. Jayaraman, "Wideband electrically pumped 1050-nm MEMS-tunable VCSEL for ophthalmic imaging," *Journal of Lightwave Technology*, vol. 33, p. 3461, 2015.

[121] W. Yang, C. J. Chang-Hasnain, "CCH Optoelectronics Group - High Contrast Grating Solver Package," University of California at Berkeley, 28 3 2014. [Online]. Available: https://light.eecs.berkeley.edu/cch/hcgsolver.html. [Accessed 2016].

[122] M. W. Maeda, C. J. Chang-Hasnain, A. Von. Lehmen, H. Izadpanah, C. Linda, M. Z. Iqbal, L. T. Florez, J. P. Harbison, "Mluti-gigabit/s operation of 16-wavelength vertical cavity surface emitting laser array," *Photonics Tehcnology Letters*, vol. 3, no. 10, pp. 863-865, 1991.

[123] B. Weigl, M. Grabherr, C. Jung, R. Jager, G. Reiner, R. Michalzik, D. Sowada, K.J. Ebeling, "High-performance oxide-confined GaAs VCSELs," *IEEE Journal of Selected Topics in Quantum Electronics*, vol. 3, no. 2, pp. 409-415, 1997.

[124] K. Lascola, "Master Degree Dissertation: Modeling of Vertical Cavity Surface Emitting Lasers," University of Californiat at Berkeley, 1997.

[125] C. Lam, H. Liu, B. Koley, X. Zhao, V. Kamalov and V. Gill, "Fiber optic communication technologies: What's needed for datacenter network operations," *IEEE Communications Magazine*, vol. 48, no. 7, pp. 32-39, 2010.

[126] P. C. Ku and C. J. Chang-Hasnain, "Thermal oxidation of AlGaAs: modeling and process control," *IEEE journal of quantum electronics*, vol. 39, no. 4, pp. 577-585, 2003.

[127] Fumio Koyama, "Engineering of angular dependence of high-contrast grating mirror for transverse mode control of VCSELs," in *Proc. of SPIE Vol. 8995 89950H-1*, 2014.

[128] Y. Tsunemi, N. Yokota, S. Majima, K. Ikeda, T. Katayama, and H. Kawaguchi, "1.55-µm VCSEL with polarization-independent HCG mirror on SOI.," *Optics Express*, vol. 21, no. 23, pp. 28686-28692, 2013.

[129] R. G. Mote, S. F. Yu, W. Zhou, and X. F. Li, "Subwavelength focusing behavior of high numerical-aperture phase Fresnel zone plates under various polarization states," *Applied physics letters*, vol. 95, p. 191113, 2009.

[130] N. Yu and F. Capasso, "Flat optics with designed metasurfaces," *Nature Materials*, vol. 13, p. 139, 2014.

[131] P. Qiao, L. Zhu, W. C. Chew, C. J. Chang-Hasnain, "Theory and design of two-dimensional high-contrast-grating phased arrays," *Optics Express*, vol. 23, no. 19, pp. 24508-24524, 2015.

[132] T.Katayama, Y. Sato, T. Mori, and H. Kawaguchi, "Polarization bistable characteristics of 1.55 um vertical-cavity surface-emitting lasers," *Japanese J. Appl. Phys.,* vol. 46, no. 49, pp. 1231-1233, 2007.

[133] P. Qiao, G. L. Su, Y. Rao, M. C. Wu, C. J. Chang-Hasnain, and S. L. Chuang, "Comprehensive model of 1550 nm MEMS-tunable high-contrast-grating VCSELs," *Optics express,* vol. 22, no. 7, pp. 8541-8555, 2014.

[134] K. Tanabe, X. GU, A. Matsutani, and F. Koyama, "Compact Vortex Beam Emitter Laterally Integrated with VCSEL Array," in *OSA Technical Digest (online) (Optical Society of America, 2015)*, paper SW1F.2, 2015.

[135] H. Li, D. B. Phillips, X. Wang, Y. D. Ho, L. Chen, X. Zhou, J. Zhu, S. Yu, and X. Cai, "Orbital angular momentum vertical-cavity surface-emitting lasers," *Optica,* vol. 2, no. 6, pp. 547-552, 2015.

[136] D. Fattal, J. Li, Z. Peng, M. Fiorentino, and R. G. Beausolei, "Flat dielectric grating reflectors with focusing abilities," *Nature Photonics,* vol. 4, pp. 466-469, 2010.

[137] D. Fattal, J. Li, Z. Peng, M. Fiorentino, and R. G. Beausoleil, "A silicon lens for integrated free-space optics," in *Integrated Photonics Research, Silicon and Nanophotonics, OSA Technical Digest*, 2011.

[138] A. Arbabi, Y. Horie, A. J. Ball, M. Bagheri, and A. Faraon, "Altmetric: 42Views: 4,234Citations: 18More detail," *Nature communications,* vol. 6, p. 7069, 2015.

[139] S. Vo, D. Fattal, W. V. Sorin, Z. Peng, T. Tran, M. Fiorentino, R. G. Beausoleil, "Sub-Wavelength Grating Lenses With a Twist," *IEEE Photonics Technology Letters,* vol. 26, no. 13, pp. 1375-1378, 2014.

[140] A. Liu, W. Hofmann, D. Bimberg, "2D analysis of finite size high-contrast gratings for applications in VCSELs," *Optics Express,* vol. 22, no. 10, pp. 11804-11811, 2014.

[141] A. Liu, W. Zheng, D. Bimberg, "Unidirectional transmission in finite-size high-contrast gratings," in *Asia Communication and Photonics Conference - AF2A.52*, 2016.